Local chromatin context dictates the genetic determinants of the heterochromatin spreading reaction.

R.A. Greenstein[1,2,†], Henry Ng[1,2,†], Ramon R. Barrales[3,#], Catherine Tan[5,6], Sigurd Braun[3,4], and Bassem Al-Sady[1,*]

1Department of Microbiology &Immunology, George Williams Hooper Foundation, University of California San Francisco, San Francisco, CA 94143, USA, 2TETRAD graduate program, University of California San Francisco, San Francisco, CA 94143, USA, 3Biomedical Center, Department of Physiological Chemistry, Ludwig-Maximilians-Universität of Munich, 82152 Planegg-Martinsried, Germany, 4Institute for Genetics, Justus-Liebig University Giessen, 35392 Giessen, Germany, #current address: Centro Andaluz de Biología del Desarrollo, Universidad Pablo de Olavide de Sevilla-Consejo Superior de Investigaciones Científicas-Junta de Andalucía, Sevilla, Spain. 5Department of Cell and Tissue Biology, University of California San Francisco, San Francisco, CA 94143, USA, 6Biomedical Sciences graduate program, University of California San Francisco, San Francisco, CA 94143, USA

† these authors contributed equally to this work, listed in alphabetical order

*correspondence: bassem.al-sady@ucsf.edu

ABSTRACT

Heterochromatin spreading, the expansion of gene-silencing structures from DNA-encoded nucleation sites, occurs in distinct settings. Spreading re-establishes gene-poor constitutive heterochromatin every cell cycle, but also invades gene-rich euchromatin de novo to steer cell fate decisions. How chromatin context, i.e. euchromatic, heterochromatic, or different nucleator types, influences the determinants of this process remains poorly understood. By screening a nuclear function gene deletion library in fission yeast using a previously established heterochromatin spreading sensor system, we identified regulators that positively or negatively alter the propensity of a nucleation site to spread heterochromatin. We find that different chromatin contexts are dependent on unique sets of genes for the regulation of heterochromatin spreading. Further, we find that spreading in constitutive heterochromatin requires Clr6 histone deacetylase complexes containing the Fkh2 transcription factor, while the Clr3 deacetylase is globally required for silencing. Fkh2 acts by recruiting Clr6 to nucleation-distal chromatin sites. Our results segregate the pathways that control lateral heterochromatin spreading from those that instruct DNA-directed assembly in nucleation.

Keywords: heterochromatin, fission yeast, spreading, chromatin context, Clr6, Clr3, Fkh2.

Cellular differentiation requires the genome to be partitioned into regions of activity and inactivity such that genes coding for lineage-inappropriate information are repressed. This requires the formation and propagation, in space and time, of gene-repressive heterochromatin structures. Heterochromatin is most commonly seeded by DNA-directed nucleation (Hall et al. 2002; Reyes-Turcu et al. 2011) and then propagates across the chromosome in a DNA-sequence indifferent process termed spreading to repress gene expression in the underlying regions. Silencing is instructed by assembly factors, such as HP1, that recognize heterochromatic chemical modifications (Jacobs et al. 2001; Lachner et al. 2001). The spreading of silencing structures occurs in at least two very different chromatin contexts: (1) Constitutive heterochromatin, which is generally gene-poor and therefore depleted of activities associated with active genes known to antagonize heterochromatin (Scott et al. 2006; Greenstein et al. 2019); or (2) heterochromatin involved in regulating cellular differentiation, which is either seeded at new nucleation sites or invades gene-rich euchromatin de-novo from existing nucleation sites (Wen et al. 2009; Zhu et al. 2013; Zylicz et al. 2015; Zylicz et al. 2018; Nicetto and Zaret 2019). In either scenario, specific factors may intrinsically promote or antagonize this process. For constitutive heterochromatin, maintenance through replication is aided by the inheritance of nucleosomes bearing heterochromatic marks (Alabert et al. 2015). This inheritance promotes modification of nearby nucleosomes due to the “read-write” positive feedback intrinsic to heterochromatin histone modifiers (Zhang et al. 2008; Al-Sady et al. 2013; Ragunathan et al. 2015). When the spreading process invades active chromatin de novo, as occurs in differentiation, it will encounter chromatin modifications that can specifically antagonize heterochromatin (Greenstein et al. 2019). Thus, during this initial invasion process, heterochromatin spreading does not benefit from the inheritance through replication of pre-existing marked nucleosomes. Beyond the differences between active and inactive chromatin, it remains unclear whether distinct nucleation element classes require different regulators to enact efficient spreading outward from those sites.

Fission yeast is an excellent model for addressing the regulation of heterochromatin spreading: (1) It contains a small number of well -defined heterochromatin nucleators, (2) harbors heterochromatin domains that are constitutive as

well as others involved in cellular differentiation, and (3) is competent to assemble ectopic heterochromatin domains induced by inserting nucleation sequences into euchromatin. Over the past four decades, forward and reverse genetic screens in fission yeast have established an exhaustive list of factors required for the nucleation of heterochromatin domains. Some of these nucleation mechanisms include repeat sequences that instruct RNAi-machinery to process noncoding (nc) RNAs involved in targeting the histone methyltransferase Clr4 (Moazed 2009); signals within nascent transcripts that trigger heterochromatin island formation (Zofall et al. 2012); pathways involving telomere-protection by the shelterin complex (Wang et al. 2016; Zofall et al. 2016); and transcription factor-bound sequences that recruit heterochromatin regulators directly (Jia et al. 2004). However, less is understood about factors specifically required for the spreading process. With our previously established fluorescent reporter-based heterochromatin spreading sensor, we can segregate the central output of heterochromatin (gene silencing) from the spatial control of the reaction (spreading) (Greenstein et al. 2018; Greenstein et al. 2019). This allows us to address the following questions: (1) Are there known or novel regulators of heterochromatin that primarily regulate spreading, versus nucleation? (2) Does spreading over chromatin with distinct characteristics, such as gene density or nucleosome arrangements, require different sets of regulators? (3) Does the set of regulators required for efficient spreading depend on the type of nucleator that seeds it - for example nucleators using transcription and ncRNA pathways versus direct tethering of heterochromatic factors?

To address these questions, we conducted a series of reverse genetic screens in S. pombe, using a custom collection of nuclear function gene deletions, which we investigated in four different heterochromatin contexts. These include several derivatives of the fission yeast mating type (MAT) locus. This gene-poor constitutive heterochromatin region is contained by IR-L and IR-R boundaries (Grewal and Klar 1997; Thon et al. 2002; Noma et al. 2006) and nucleated by at least two elements: (1) cenH, which is homologous to pericentromeric dh and dg elements and relies on ncRNA pathways, including RNAi (Grewal and Klar 1997; Thon and Friis 1997; Noma et al. 2004); (2) the REIII element, a sequence which recruits heterochromatin factors via the stress-response transcription factors Atf1 and Pcr1 (Jia et al. 2004; Kim et al. 2004). We also queried an ectopic heterochromatin domain that is embedded in gene rich euchromatin. This domain is nucleated by an ectopically inserted dh element fragment proximal to the ura4 locus (Canzio et al. 2013; Marina et al. 2013; Greenstein et al. 2018).

The following themes emerge from our genetic screen for heterochromatin spreading in these contexts: (1) The genetic requirements for promotion and containment of heterochromatin spreading differ significantly between distinct chromatin contexts, and to some degree also between different types of nucleators. Among the spreading promoting factors identified, only two contribute to all loci we examined, and neither was previously implicated in heterochromatin assembly. (2) A division of labor between two histone deacetylase (HDAC) complexes in global heterochromatin silencing and spreading. Sub-complexes of the Clr6 complex containing the Fkh2 transcription factor promote spreading, but not nucleation, at multiple heterochromatin loci, while the Clr3 HDAC is required for global heterochromatic silencing at most sites. (3) Broad antagonism of spreading at both euchromatic and heterochromatic loci by a diverse set of nucleosome remodelers, in particular Ino80 and Swr1C.

Results

Our previously developed heterochromatin spreading sensor relies on three transcriptionally-encoded fluorescent protein-coding genes that collectively report single-cell measurements of heterochromatin formation via flow cytometry, while normalizing for transcriptional and translational noise (Al-Sady et al. 2016; Greenstein et al. 2018). It provides separate, quantitative recordings of nucleation-proximal ("green") and distal ("orange") events at a heterochromatin site over large populations of isogenic cells (typically N >20,000, except when strains grow poorly) (**Figure 1A**). In contrast to the singular readout employed by auxotrophy-dependent reporter gene silencing assays, the heterochromatin spreading sensor assay distinguishes changes in heterochromatin nucleation and spreading, and additionally permits tracking of emerging multimodal cell populations and unique population distributions.

Design of heterochromatin spreading sensors at four chromatin contexts.

To explore whether the heterochromatin context utilizes general or specific sets of regulators for the spreading reaction, we queried three different derivatives of the constitutively heterochromatic mating type (MAT) locus and one euchromatic context, each containing an embedded heterochromatin spreading sensor (**Figure 1A, Figure 1 Supplement 1**) (Greenstein et al. 2018). The mating-type locus contexts included wild type MAT, with the cenH and REIII nucleating DNA elements intact, and two MAT variants that contained mutations in either the cenH or REIII elements (**Figure 1A, Figure 1 Supplement 1A,B**). Mutations in these DNA elements limit initiation of heterochromatin spreading to one nucleator (Greenstein 2018). To probe heterochromatin formation in the euchromatic

context, we focused on the ura4 locus, where heterochromatin spreading is ectopically driven by the upstream insertion of a pericentromeric dh DNA element (**Figure 1 Supplement 1C**, (Marina et al. 2013; Greenstein et al. 2018)). We refer to this chromatin context as ECT (ectopic). When analyzed by flow cytometry, WT MAT and MAT ΔcenH (OFF isolate, see methods) populations appear fully nucleated with near-complete local spreading, as evidenced by population density in the bottom left in the 2D density hexbin plot (**Figure 1F,H TOP** (Greenstein et al. 2018)). MAT ΔREIII and ECT cell populations, while mostly nucleated, display a stochastic distribution of spreading states, as evidenced by a vertical distribution on the left of the 2D density histogram (**Figure 1J,L TOP** (Greenstein et al. 2018)). While the distance between nucleation and sensor sites varies slightly for the different chromatin context analyzed (from 2.4 to 3.6 kb; see **Figure 1 Supplement 1**), we showed previously that altering the distance between "green" and "orange" does not qualitatively affect the output (Greenstein et al. 2018). Thus, we presume that these differences in behavior reflect different intrinsic properties of the chromatin environment rather than differences in the reporter arrangement. In addition to wild-type background, we display Δclr3 as reference for a strong loss-of-silencing mutant (**Figure 1F,H,J,L**).

Identification of chromatin context-specific spreading regulators.

We crossed a deletion library of ~400 nuclear function genes (see methods and Table 1, Figure 1B) to these four reporter strains and measured nucleation and spreading by flow cytometry. To segregate spreading from nucleation, we first isolated cell populations that reside within a "green"-off gate, which represents cells with heterochromatin fully assembled at the nucleation site and no expression of the reporter (see methods, Figure 1C and (Greenstein et al. 2018)). Within this gate, we divide the "orange" signal into 4 grids, from fully repressed (i.e., complete spreading over "orange"; Grid 1) to fully de-repressed (i.e., no silencing at "orange; Grid 4), with the remaining space symmetrically divided to yield Grids 2&3 (see methods). To quantify increased or decreased spreading in a given mutant, we calculated a $Grid_n^{mut/par}$ metric (described in methods), which tracks the changes of cell distributions in "orange" expression within the "green"-off gate (**Figure 1C**). Since WT MAT and MAT ΔcenH display very tight silencing of both "green" and "orange" with very few events in grid 4 (**Figure 1F,H**), we used a $Grid_n^{mut/par}$ metric that considers both grids 3+4 for the robust identification of spreading defects. MAT ΔREIII and ECT have a more stochastic spreading behavior with "green"-off cells populating a range of "orange" states from OFF to ON (Greenstein et al. 2018), including to some extent both grid 3 and 4 (**Figure 1J.L**). Hence, for these two contexts we used a $Grid_n^{mut/par}$ metric that only considers grid 4 to focus on complete loss of spreading (i.e. "orange" signal in the range of Δclr4 control). To isolate gain or loss of spreading mutants (hits) for further analysis, we employed two metrics (1) a significance threshold when multiple parental isolates were available (all except ECT) and (2) a percentile based cut-off. As significance threshold, we only considered mutants in which $Grid_n^{mut/par}$ values were above 2 standard deviations beyond the mean of the parent isolates (Figure 1 G,I,K,M). As an additional cut-off, we only considered the top 15% of all $Grid_n^{mut/par}$ -ranked mutants, even if more genes pass the 2SD significance threshold. Having identified these gene hits, we next proceeded to analyze their relationships within and across chromatin contexts.

We first examined the degree to which spreading modulators are shared between chromatin contexts via upset plots (**Figure 1D,E**). Conceptually similar to a Venn diagram, this analysis allows rapid visualization of the degree of overlap between sets, with the number of shared hits plotted as a bar graph and the sets each bar represents annotated below the plot. For loss of spreading phenotypes (i.e. genes that promote spreading, Figure 1D), these upset plots showed that exceedingly few genes (i.e. 2 of 164 unique hits) are shared across all chromatin contexts, emphasizing the specific impact of each context on heterochromatin spreading. Notably, these two genes (*apm3, rrp17*) have not previously been implicated in heterochromatin assembly. Apm3 has been proposed to be part of an AP-3 adaptor complex, whereas Rrp17 is a predicted rRNA exonuclease. Six genes were shared across all the MAT locus chromatin contexts (*apl5, cph1, hrp1, spt2, snt2, pcf1*). In contrast, the majority of hits (i.e. 101 genes) contributed only to one chromatin context. The degree to which genes contributed positively towards spreading ($Grid_n^{mut/par}$) and the degree of overlap across chromatin contexts (by color code) is shown in **Figure 1G,I,K,M**. We additionally show the 2D density hexbin plot for the top loss-of-spreading hit for each context (**Figure 1F,H,J,L**). Among the top hits, we made the following observations: (1) Pathways involved in the removal of the heterochromatin antagonist Epe1 play a prominent role in promoting spreading. Epe1 is turned over by an E3 ligase complex (Braun et al. 2011), which includes the adaptor proteins Ddb1 and Cdt2 and is regulated by the COP9 signalosome also involved in Epe1 turnover (Bayne et al. 2014).We found that *csn1* (COP9), *cdt2*, and *ddb1* are the three strongest hits in ECT and that cdt2 is also among the top hits in MAT ΔcenH. (2) Beyond the Epe1 turnover pathway, additional top hits unique to ECT are the histone variant H2A.Z (*pht1*), which antagonizes heterochromatin

spreading in budding yeast (Meneghini et al. 2003), and an Asf/HIRA chaperone subunit (*hip1*) (Figure 1M). (3) For WT MAT and MAT ΔREIII, we found as top hit fkh2, which encodes a transcription factor, and as second top hit, *rrp6*, a key member of the nuclear exosome (see below; **Figure 1G,K**). (4) The strongest and largely unique hit in MAT ΔcenH is gad8, which encodes a protein kinase that targets several factors, including Tor2 and Fkh2 (**Figure 1I**).

As mentioned above, loss of the AP-3 adaptor complex subunits Apm3 and Apl5 induced loss of spreading in either all chromatin contexts (Apm3) or only the MAT contexts, respectively (Apl5, also observed in (Holla et al. 2020)). We further assessed the activities of Apm3 and Apl5 by newly generating *Δapm3* and *Δapl5* single and double mutants in the MAT ΔREIII background, where *Δapm3* and *Δapl5* had a moderate and mild effect in the screen, respectively. We reproduced the mild to moderate spreading defect for both single mutants; we further observed a slightly stronger defect in the *Δapm3 Δapl5* double mutant ($Grid_4^{mut/par}$ 1.56) compared to the *Δapm3* and Δapl5 single mutants ($Grid_4^{mut/par}$ 1.4 and 1.16, respectively); **Figure 1 Supplement 2A-D**). Whereas Apl5 is largely cytoplasmic, Apm3 shows both nuclear and cytoplasmic localization, (**Figure 1 Supplement 2E,F**) and also affects H3K9me2 accumulation at heterochromatin islands (**Figure 1 Supplement 2G**). Together, these findings may support the notion of a direct rather than indirect role for Apm3 in heterochromatin assembly. However, further work is needed to elucidate the specific function of Apm3 in heterochromatin spreading and whether this is linked to the AP-3 complex itself.

Besides loss of spreading, we also identified mutants that showed gain of spreading in WT MAT, MAT ΔREIII and ECT (Figure 1E, Figure 1 Supplement 3) by examining a $Grid_n^{mut/par}$ metric that considers grid 1. We could not examine MAT ΔcenH for this phenotype because this chromatin context is highly repressed in the OFF state as reported previously (Grewal and Klar 1996; Greenstein et al. 2018). Also for this phenotype, only a limited number of mutants are shared as hits across these three chromatin contexts (5 out of 98, *vps71, arp6, leo1, git1, pmk1*, Figure 1E; examples for top hits are shown in Figure 1 Supplement 3). Notably, Leo1 was previously shown to be implicated in spreading control across boundaries (Verrier et al. 2015), whereas Vps71 and Arp6 are members of the H2A-Z-specific Swr1 remodeling complex(Krogan et al. 2003). ECT displayed the largest fraction of spreading-antagonizing genes that are unique to a single context, with 46 out of 69. In contrast, while ECT displays a very similar spatio-temporal spreading behavior to MAT ΔREIII (Greenstein et al. 2018), we found little overlap between the two and only 14 genes unique to MAT ΔREIII (**Figure 1J,L**). The larger number of antagonists in ECT suggests that spreading is under additional layers of control in the euchromatic context.

Due to the chromatin context-specific effects and the fact that this type of spreading analysis with the heterochromatin spreading sensor system has not been conducted before, we sought to independently validate above observations. We selected 5 mutants that have chromatin context-specific effects, covering both loss and gain of spreading: *saf5*, which shows gain of spreading in WT MAT and mildly in MAT ΔREIII; *eaf6*, which shows gain of spreading in MAT ΔREIII only; *pht1* and *hip1*, which show loss of spreading only in ECT; and *gad8*, which shows loss of spreading primarily in MAT ΔcenH. We recreated these mutations de novo in the chromatin contexts described above and conducted RT-qPCR analysis for SF-GFP ("green", nucleation) and mKO2 ("orange", spreading) transcripts. This validation approach recapitulated broadly what our screen analysis showed **(Figure 1, Supplement 4**), confirming the context-specific functions in heterochromatin spreading of these gene products.

Taking our analysis beyond individual genes, we sought to query which protein complexes are involved in spreading regulation, as this can point out the major pathways involved in this process. Using the Gene Ontology (GO) protein complex annotations from Pombase (Lock et al. 2018), we annotated each gene hit identified using the criteria described in Figure 1 (G-M). We then tabulated the frequency ("counts") of each GO complex per chromatin context for both loss of spreading (loss) and gain of spreading (gain) phenotypes, performed unsupervised clustering on the data, and displayed the results as a heatmap (**Figure 2 Supplement 1**). Overall, we identified three major common trends: (1) a role for chromatin remodelers in antagonizing spreading; (2) a role for the SAGA complex in promoting spreading at ECT; (3) a role for Clr6 histone deacetylase complexes (HDACs) in promoting spreading, with the notable exception of Set3C, which antagonizes spreading and is annotated into the expanded Rpd3L complex.

Chromatin remodelers broadly antagonize spreading.

Mutants defective in chromatin remodeling complexes strongly contribute to the "gain" phenotype category, including the Swr1C, Ino80, SWI/SNF, and RSC-type complexes (**Figure 2 Supplement 1**). To explore this further, we assessed which protein components contributed to these GO complex counts. For all genes annotated to a given chromatin remodeling complex and

present in our screens, we displayed whether they were identified as a hit (blue) or not (grey) in a hit table (**Figure 2A**). Indeed, we found that the large majority of the gene hits annotated fall within the "gain" but not "loss" phenotype across backgrounds, confirming a potential role of these nucleosome remodeling complexes in antagonizing spreading.

SAGA promotes spreading, primarily in the euchromatic context.

A surprising observation was the enrichment of a large number of subunits of the SAGA complex among the loss-of-spreading hits, which was represented with six subunits in the ECT context, the most enriched single complex for any background (**Figure 2B**). This implies that SAGA, a histone acetylase involved in gene transcription, positively regulates heterochromatin spreading in euchromatin. To assess if SAGA contributes directly to spreading of the heterochromatin structure, rather than indirectly to gene silencing, we assessed the accumulation of H3K9me2 at "green" and "orange" in the ECT background, as well as the pericentromeric *dg* element. Consistent with the screen data, we find that the histone acetylation catalytic subunit Gcn5 is required for efficient spreading of H3K9me2 to "orange", but not its establishment at "green" or at *dg* **(Figure 2, Supplement 2**).

Clr6 HDAC complexes promote spreading, primarily in constitutive heterochromatin.

Three classes of HDACs exist, which have partially redundant and non-overlapping functions in the formation of heterochromatin domains and gene silencing. Clr6 belongs to class I and is part of several sub-complexes, contributing to both heterochromatic and euchromatic gene regulation (Grewal et al. 1998; Nicolas et al. 2007). Clr3 belongs to class II and is a member of the SHREC complex (Sugiyama et al. 2007) and Sir2 belongs to the class III HDAC of the sirtuin family (Shankaranarayana et al. 2003). Unlike class II and III HDACs (Clr3, **Figure 1**; Sir2, **Figure 1 Supplement 5**), we show here that sub-complexes of the Clr6 family, including the Rpd3S, Rpd3L, and Clr6 I", appear to contribute exclusively to spreading but not nucleation (for hit table of top hits and 2D hexbin plots see Figure 2C; for additional 2D hexbin plots of all Clr6 components see **Figure 2 Supplement 3**). As noted above, the forkhead transcription factor Fkh2 was identified among the strongest spreading hit in WT MAT and MAT ΔREIII HSS strains. Despite not being formally annotated to the Clr6 I" complex by GO terms, Fkh2 was previously described as a member of this sub-complex (Zilio et al. 2014). We included Fkh2 as a member of Clr6 I" in further analysis for this reason. While Rpd3L/ Clr6 I', Clr6 I", and Clr6S (Complex II) positively contributed to spreading ("loss" phenotype), several members of the Rpd3L-Expanded complex antagonized spreading and were found as hits inducing a "gain" phenotype (Figure 2C). This includes a subset belonging to the Set3 Complex (Set3, Hif2, Hos2, Snt1). Next, we confirmed the phenotypes of *Δfkh2* and *Δprw1* by generating de novo generated gene deletions in the MAT ΔREIII heterochromatin spreading sensor (Figure 2C). The *Δfkh2 Δprw1* double mutant displayed a similar phenotype to the single mutants, corroborating the notion that Fkh2 acts in the same pathway as Prw1 (Figure 2C).

Overall, this data suggests that Clr6 I', Clr6 I" and Clr6S HDAC complexes specifically promote heterochromatin spreading in addition to their described roles in transcriptional gene silencing.

Clr6 complexes, in contrast to Clr3, promote H3K9me2 spreading and do not contribute significantly to nucleation.

Our above analysis suggested that Clr6 complex subunits contribute to the spreading of gene silencing. In what comes below, we address the mechanisms underlying this phenotype, and contrast the role of Clr6 to that of another prominent heterochromatic HDAC, Clr3. First, we examined whether the phenotype observed for Δprw1 and *Δfkh2* also holds true for clr6 itself, which codes for the catalytic subunit. To do this, we explored the *clr6-1* allele, which displays a hypomorphic phenotype at permissive temperatures (note that clr6 is an essential gene) (Grewal et al. 1998). Under this condition, *clr6-1* shows moderate spreading defects in MAT ΔREIII without affecting nucleation, which is consistent with its role in nucleation-distal silencing (**Figure 3 B vs. A**). In contrast, mutants in the HDAC Clr3 behaved differently, showing a complete loss of silencing when employing a catalytic dead version of Clr3 (*clr3-D232N*) (**Figure 3 C vs A, Figure 1**). This result implies that the two major HDACs, Clr6 and Clr3, have different roles in heterochromatin silencing.

Next we examined directly whether heterochromatin assembly is impacted. To this end, we focused on the H3K9me2 mark, which signals heterochromatin formation and can accumulate without major changes in gene expression (Jih et al. 2017). This allows us to examine chromatin structure independent of gene silencing. We performed H3K9me2 ChIP-Seq analysis in wild-type and the mutants *Δfkh2*, *Δprw1*, *clr6-1*, and *clr3-D232N* and analyzed the data in two independent ways: First, we produced input-normalized signal tracks, plotting mean and 95% confidence interval per genotype calculated from multiple replicates (**Figure 3 E-H**; see methods). Second, we conducted a differential

enrichment analysis that examines 300bp windows along the genome containing above-background signal for significantly different accumulation of H3K9me2 between each mutant and the wild-type (**Figure 3 E-H**; see methods).

Principal Component Analysis (PCA) on the overall phenotype revealed that mutant isolates segregated from the wild-type along PC1, with Clr6 mutants diverging additionally from wild-type along PC2 (**Figure 3 Supplement 1A**). Focusing on the signal tracks as well as the differential enrichment analysis, we make the following overall observations across the genome: The three Clr6-related mutants, *Δfkh2*, *Δprw1*, and *clr6-1*, show defects in heterochromatin spreading at all heterochromatic locations in the genome (**Figure 3E-H**). This is evidenced both by separation of the 95% confidence intervals of the mutant versus wild-type signal tracks and the differential enrichment analysis, with the effect most prominent at the pericentromeres (**Figure 3F, Figure 3 Supplement 1 C, D**) and the sub-telomeric regions (**Figure 3 G,H, Figure 3 Supplement 1E,F**). At the MAT locus, the effect is more restricted to the region centromere-distal from cenH **(Figure 3E, Figure 3 Supplement 2G**), consistent with the location of "orange" (**Figure 1 Supplement 1**). This further does not appear to impact the region near REII, which is centromere-proximal from cenH. Importantly, Clr6 mutants show little defect in H3K9me2 accumulation at nucleation centers, especially those driven by RNAi, i.e. cenH at MAT, the dg and dh repeats at the pericentromere, and homologous repeats at the subtelomeric *tlh1/2* gene (**Figure 3E-H**). This suggests that Clr6 complexes largely do not contribute to heterochromatin assembly during nucleation, but instead are essential for spreading. In contrast, Clr3 appears to act upstream, as the catalytic mutant *clr3-D232N* shows strong H3K9me2 accumulation defects at all major nucleation centers as well as the distal regions (**Figure 3E-H**). This is consistent with the view that spreading is conditioned on preceding successful heterochromatin assembly at nucleation sites. The sole exception are heterochromatin islands, where surprisingly, *clr3-D232N* shows increased H3K9me2 accumulation, possibly due to redistribution form RNAi nucleation centers elsewhere (**Figure 3 Supplement 1 G-I**). At these regions, Clr6 mutants, in contrast, show loss of H3K9me2.

We further analyzed the different impact of Clr6 and Clr3 on H3K9me2 at nucleation sites and distal regions via volcano plots of regions tested for differential enrichment in comparisons of *Δfkh2*, *Δprw1*, *clr6-1,* and *clr3-D232N* each to wild-type (**Figure 3 I-L, Figure 3 Supplement 2A-D**). While all mutants have significantly reduced enrichment relative to wild-type at distal sites subject to spreading, these plots reveal key features that separate the phenotype of the Clr6C mutants from clr3-D232N: We find, (1) that nucleation center sequences are significantly reduced in the *clr3-D232N* versus wild-type comparison, but not in Clr6 complex mutant comparisons to wild-type. This further indicates that *clr3-D232N*, but not Clr6 mutants, show significant H3K9me2 accumulation defects at nucleation centers. In addition, this analysis reveals (2) that, in comparison to wild-type, *clr3-D232N* shows significantly increased H3K9me2 enrichment at euchromatic sites, namely islands, which is absent for the Clr6-related mutants (**Figure 3L, right**). Overall, these analyses reinforce the view that Clr6 primarily impacts spreading of H3K9me2, but not its accumulation at nucleation centers.

Fkh2 is part of several Clr6 complexes in vivo.

It is not established how Fkh2 integrates into Clr6 complexes, or how it may contribute to Clr6 activity. It has previously been shown that Fkh2 co-immunoprecipitates with Clr6 (Zilio et al. 2014). We validated this result here for Clr6 and Sds3, which specifies Clr6 I complexes (Figure 4 Supplement 1A). However, this result does not imply necessarily that Fkh2 is a resident member of Clr6 complexes, and if so, of which one(s). To address this question, we performed sucrose gradient fractionations of cellular lysates, similar to prior analyses (Nicolas et al. 2007), using a Fkh2-TAP fusion and epitope-tagged Clr6-13MYC. Clr6 is distributed into a number of complexes, as shown previously, but does not appear to exist in free form (**Figure 4A and Figure 4 Supplement 1C**). Fkh2-TAP is also distributed into several Clr6 peaks: It associates strongly with a large Clr6 complex focused in fraction 10. It also associates with Clr6 in fractions 5-7 but most strongly in fraction 7. Fkh2, unlike Clr6, also migrated in an apparent free form (fraction 2), consistent with its role as a transcription factor (Buck et al. 2004; Bulmer et al. 2004). When we performed this experiment with Fkh2-13MYC and Sds3-TAP, we find Fkh2 associated with the main Sds3 fractions (peaks in fractions 9-10, **Figure 4 Supplement 1B**). Hence, we believe that this peak represents the Clr6 I' (Nicolas et al. 2007) and the related Clr6 I" complexes (Zilio et al. 2014), which would be consistent with the involvement of Clr6 I" subunits in the regulation of spreading (**Figure 2C**). Based on prior analysis (Nicolas et al. 2007), the mid-sized complex containing Clr6-13MYC and Fkh2-TAP (**Figure 4A**, fraction 7), likely, represents complex II, which is consistent with the involvement of Cph2 and Alp13 as spreading regulators across all chromatin contexts (**Figure 1, Figure 2C**). Next, we sought to address if this co-migration indicates stable Clr6 complex association. We predicted that the migration pattern of Fkh2 would change in mutants of core Clr6 complex

members. When we performed sucrose gradient analysis with Fkh2-13MYC (as opposed to Fkh2-TAP above) in the *Δprw1* mutant, we found that the peaks associated with bound, but not free, Fkh2-MYC are shifted towards lower molecular weight by one fraction; this was seen for both, large and small Clr6 complexes (**Figure 4B**). We note that in this experiment, more Fkh2-MYC was detected in lower molecular weight migrating complexes. Therefore, we conclude that Fkh2 is a *bone fide* member of Clr6 complexes.

Fkh2 helps direct Clr6 to distal heterochromatin sites specifically, and not euchromatic or nucleation sites.

We next sought to understand how Fkh2 helps Clr6 spread H3K9me2. One trivial possibility is that Fkh2 directs the transcription of major heterochromatin components, independent of its association with Clr6 complexes. To test this notion, we performed RT-qPCR for 9 major heterochromatin regulators, including representatives of the ClrC, RITS, Clr6, and SHREC complexes, as well as swi6. We do not observe any significant reduction of these transcripts in *Δfkh2* compared to wild-type (**Figure 4 Supplement 2**), suggesting that Fkh2 acts via another mechanism. We next tested whether Fkh2 affects the chromatin localization of Clr6. Using ChIP, we tracked the chromatin association of Clr6-13MYC at various heterochromatic loci in WT or *Δfkh2* in the MAT ΔREIII heterochromatin spreading sensor background. At the MAT locus, Clr6-13MYC was efficiently detected above untagged background signal at cenH “green” or at mtd1, a gene in euchromatin outside the IR-R MAT boundary. At these loci, Clr6 recruitment was not affected by the absence of Fkh2 (**Figure 4C**). However, at “green”-distal sites, namely the “orange” reporter and a more boundary proximal site, deletion of *fhk2* reduces the localization of Clr6. Similarly, *Δfkh2* affects Clr6 localization at the heterochromatin islands *mei4, mcp7*, and *ssm4* (**Figure 4D**). At telomeres, where *Δfkh2* also has a significant impact on H3K9me2 spreading, we also find a significant reduction in Clr6 chromatin association at distal sites (**Figure 4E**, 30kb) but not at the euchromatic control locus, act1 (**Figure 4F**). Therefore, it appears that one role of Fkh2 in promoting heterochromatin spreading is to strengthen the recruitment of Clr6 to nucleation-distal heterochromatic sites.

Discussion

The formation of a heterochromatin domain requires three interconnected steps, nucleation, assembly of heterochromatin structures, and the lateral spreading from DNA-sequence driven nucleation sites. The genetic circuitry that regulates spreading at different chromatin loci is not well understood. Here, our ability to separate requirements for nucleation and distal spreading within heterochromatin domains allowed us to pinpoint which factors are necessary to drive or restrain spreading at different genomic loci. A key finding from this work is the requirement of variants of the Clr6 HDAC complex specifically in the spreading reaction, in addition to the antagonism by a broad class of chromatin remodelers. Additionally, we find that different chromatin contexts have specific requirements for spreading, for example, the role of SAGA in promoting spreading within euchromatin.

Of the HDACs involved in heterochromatin function, Clr3 is likely the best described. Its associated SHREC complex is required for silencing, likely via its ability to repress nucleosome turnover (Aygun et al. 2013), maintain nucleosome occupancy (Sugiyama et al. 2007; Garcia et al. 2010), and remove H3K14 acetylation known to antagonize heterochromatin assembly (Wirén et al. 2005). Our results show that Clr3 catalytic and deletion mutants completely lose heterochromatic silencing and are defective in H3K9me2 accumulation (**Figure 1, 3**) including at nucleation centers (**Figure 3, Figure 3 Supplement 3**). Similarly, the Sir2 HDAC is broadly implicated in heterochromatin nucleation and assembly (Shankaranarayana et al. 2003; Alper et al. 2013), and we also observe near-complete silencing loss in *Δsir2* (**Figure 1 Supplement 5**). In contrast to Clr3 and Sir2, Clr6 is required specifically for heterochromatin spreading, but not assembly at nucleation centers (**Figures 1-3**). This is consistent with the finding that the clr6-1 allele has only small impacts on transcription of the cenH nucleator-encoded ncRNAs (Yamane et al. 2011). Our screen showed that several, but not all members, of the recently described Clr6 complex I" (Zilio et al. 2014) promote spreading, Key subunits of Clr6 II and Clr6 I' were also featured as hits. That not all annotated Clr6 subunits share gain or loss of spreading phenotypes may suggest these subunits do not contribute to heterochromatin spreading, but instead mediate other functions of the complex. On the other hand, Fkh2 is a very prominent subunit promoting spreading, especially at MAT. As we find that Fkh2 is a resident member of several Clr6 complexes, the I',I", and II types (**Figure 4A, B**), we believe these results indicate two possible, nonexclusive interpretations: (1) the composition of different Clr6 subcomplexes in vivo is either more dynamic than previously thought, and/or (2) a number of different, preassembled Clr6 complexes can associate with Fkh2, which imparts a role in spreading regulation. Interestingly, the Set3-submodule that typifies the Rpd3L-Expanded complex (Shevchenko et al. 2008) has a distinct spreading-antagonizing behavior (**Figure 2C**). This contrasts with a mild positive role of the Set3 complex at pericentromeres (Yu et al. 2016). Taken together, we believe our data suggest that Clr3

works upstream, to establish heterochromatin at noncoding-RNA driven nucleation centers, and Fkh2-containing Clr6 complexes function downstream to spread heterochromatin structures outward (**Figure 4G**).

What mediates the spreading-specific role of Clr6 complexes? One possible explanation is that they act in conjunction with the histone chaperone Asf/HIRA which cooperates with Clr6 in gene silencing at ncRNA nucleators (Yamane et al. 2011). However, we do not favor that this pathway mediates distal spreading, since Asf/HIRA subunits Hip1, Hip3 and Slm9 have mild or no phenotype for spreading in MAT contexts. Asf/HIRA mutant phenotypes were more pronounced in ECT, a context that is less reliant on Clr6 for spreading (**Figure 1**, see below). We believe Fkh2 plays a key role in imparting this spreading-specific role for Clr6. Fkh2 is a transcription factor that regulates meiotic genes in *S. pombe* (Buck et al. 2004; Bulmer et al. 2004; Alves-Rodrigues et al. 2016). However, the observation that loss of Fkh2 impacts H3K9me2 spreading at all sites (**Figure 3, Figure 3 Supplement 3**) makes it less likely in our view that Fkh2 acts via binding to canonical sequence motifs. Fkh2 has also been shown to act as a chromatin organizing protein through clustering origins of replication (Knott et al. 2012). It is conceivable that Fkh2 creates chromatin environments that are conducive to nucleation -distal Clr6 recruitment, either by tethering to a nuclear compartment such as the nuclear periphery (Holla et al. 2020) or via chromatin conformational or biophysical changes (Sanulli and G 2020; Zenk et al. 2021). In either case, Fkh2 promotes the recruitment of Clr6 complexes to the spreading zone (**Figure 4C-E).** The spreading-specific role of Clr6 complexes may be additionally supported by other known recruitment mechanisms, for instance HP1/Swi6 (Hall et al. 2002; Canzio et al. 2011) (Fischer et al. 2009). While the precise mechanism of Fkh2-mediated Clr6 recruitment will be the subject of further study, our results unambiguously demonstrate that Fkh2 typifies a specific functional mode of the conserved HDAC Clr6/RPD3 among its numerous essential activities in gene regulation (Yang and Seto 2008).

Our results show a role of chromatin remodelers across several classes in antagonizing spreading. This role is widespread, as Ino80, Swr1C, SWI/SNF and RSC appear to contribute to antagonizing heterochromatin spreading. This broad antagonism contrasts with more specific functions uncovered previously for Ino80/Swir1C (Meneghini et al. 2003). As above for Clr6, not all subunits show a spreading phenotype. Remodelers have been implicated in negatively regulating heterochromatin function by creating specific nucleosome free regions (NFRs, (Lorch and Kornberg 2017)) that antagonize heterochromatin. Since NFRs may be roadblocks to spreading (Garcia et al. 2010; Lantermann et al. 2010), it is possible that remodelers employ this mechanism to restrain heterochromatin spreading globally. In addition, remodelers such as SWI/SNF and RSC destabilize nucleosomes generally (Narlikar et al. 2001; Rowe and Narlikar 2010), leading to increased turnover (Rawal et al. 2018), which would antagonize heterochromatin spreading. This increased turnover may be tolerated at ncRNA nucleation sites, where turnover is at near euchromatic levels (Greenstein et al. 2018), likely due to ncRNA transcription (Volpe et al. 2002; Noma et al. 2004). This would suggest that regulation of nucleosome stability has a particular significance at distal, but not nucleation sites.

Beyond the broad finding of Clr6 and remodelers as specific promoters and antagonizes of spreading respectively, this study uncovered several locus- and nucleation center type-specific pathways. Here we would like to highlight two main observations:

1. Distinct factors are required for similar nucleators in different chromatin environments. ECT and MAT ΔREIII are both driven by related ncRNA nucleators (dh and cenH, respectively) and have remarkably similar behaviors with respect to nucleation and spreading across the cell population (Greenstein et al. 2018). Efficient spreading specifically at ECT requires Hip1, and moderately Slm9, which code for a key subunits of the HIRA H3/H4 chaperone. HIRA has been implicated in stabilizing heterochromatic nucleosomes (Yamane et al. 2011). Hence, given that transcribed chromatin is known to destabilize nucleosomes, it seems likely that this specific requirement reflects the challenge faced by heterochromatic domains when expanding within gene-rich chromatin. ECT is also particularly reliant on the SAGA complex for spreading **(Figure 2A, Figure 2 Supplement 2**). This initially may seem counterintuitive , as SAGA has been shown to be recruited by Epe1 to antagonize heterochromatin assembly at constitutive sites (Bao et al. 2019). In fact, in our screen SAGA plays a less prominent role in the MAT context. This requirement for SAGA at ECT may be connected to the observation that SAGA can modulate the chromatin recruitment of remodelers, such as SWI/SNF, via direct acetylation (Kim et al. 2010). Therefore, one possible explanation that remains to be tested for the SAGA phenotype we observe is acetylation of SWI/SNF and possibly other remodelers that antagonize spreading, releasing them from chromatin.

2. Spreading from qualitatively different nucleators within the same environment, namely REIII and cenH, also differ in their sensitivity to different mutants. The significant overlap in factors between WT MAT and MAT ΔREIII indicates that

heterochromatin formation at MAT is dominated by the ncRNA nucleator cenH, in agreement with our previous findings (Greenstein et al. 2018). The REIII element, which nucleates heterochromatin independent of ncRNA (Jia et al. 2004), has different requirements. For example, ncRNA-independent spreading at REIII (MAT ΔcenH) is uniquely promoted by the MTOR pathway Gad8 kinase, partially consistent with a previous report implicating Gad8 for MAT silencing (Cohen et al. 2018). While Gad8 is reported to target Fkh2 for phosphorylation, *Δfkh2* has very weak effects on MAT ΔcenH. Other potential phosphorylation targets of Gad8, if it acts through its kinase function, in promoting spreading from REIII remain to be established. We note that REIII can confer a high propensity for local intergenerational inheritance of silencing (Grewal and Klar 1996; Greenstein et al. 2018). Therefore, a formal possibility for spreading defects in the MAT ΔcenH context, or others with high intergenerational stability, is that the gene identified is required for the maintenance of heterochromatin outside the nucleator, rather than its initial formation by spreading.

In this work, we defined how regulation of heterochromatin silencing and nucleation differ in fundamental ways from distal spreading. While similar nucleation elements likely rely on a common set of machinery, the success of heterochromatin spreading appears much more sensitive to the chromatin context, particularly in gene-rich versus gene-poor chromatin. Our findings will likely have important implications for directing gene silencing during cellular differentiation. In this situation, regions that have previously been in a transcriptionally active state are invaded by heterochromatin and will have to compete for core spreading factors in a dosage limited system (Eissenberg et al. 1992; Nakayama et al. 2000). We note that several of the factors we identify as critical to regulating spreading in euchromatinic environments are conserved in metazoans, opening the possibility that they contribute differentiation via heterochromatin control in these organisms.

Methods

Mutant Generation for Genetic Screen.

We generated a 408 gene deletion mini-library that represent a subset of the S. pombe Bioneer deletion library, focused on nuclear function genes. The library (table 1) was assembled via three criteria: 1. ~200 genes coding for proteins that evidence "nuclear dot" morphology based on a high-throughput YFP- tagged"ORFeome" screen (Matsuyama et al., 2006, also used in Braun et al., 2011). 2. ~50 deletions of central *S. pombe* DNA binding transcription factors. 3. ~150 gene deletions selected based on a search of annotations for chromatin regulation- related functions (majority of this set), or prior preliminary data for roles in regulation of heterochromatin function. Deletions that grow poorly in rich media were eliminated. Several Bioneer collection mutants were independently validated and produced de novo. For the ectopic locus HSS reporter strain, the screen was performed essentially as described (Greenstein et al. 2019). Briefly, the parent HSS reporter strain was crossed to the library. Crosses were performed as described (Verrier et al. 2015; Barrales et al. 2016; Greenstein et al. 2018; Greenstein et al. 2019) using a RoToR HDA colony pinning robot (Singer). For the MAT HSS reporter strains, the screen was performed essentially as described (Greenstein et al. 2019) with the exception that crosses were generated using a 96 well manual pinner. Note that the MAT ΔcenH, we used an OFF isolate as described (Greenstein et al. 2018). This is because ΔcenH behaves in a bimodal fashion, producing stable ON (no heterochromatin) and OFF (heterochromatin) alleles at MAT. In addition, three Δ*clr4* mutant isolates and six individual parent isolates from each genomic context were included as controls. Crosses for the ectopic HSS strains were performed using SPAS media for 4d at room temperature, while for the MAT HSS strain crosses were performed on ME media for 3d at 27°C. For all strains, crosses were incubated for 5d at 42°C to retain spores, while removing unmated haploid and diploid cells. The ectopic HSS spores were germinated on YES medium supplemented with G418, hygromycin B, and nourseothricin. For MAT HSS strains, spores were germinated on YES medium supplemented with G418 and hygromycin B. The resulting colonies were pinned into YES liquid medium for overnight growth and then prepared for flow cytometry as described below.

Flow Cytometry Data Collection and Normalization for Genetic Screen.

In preparation for flow cytometry, overnight cultures were diluted to OD = 0.1 (approximately a 1:40 dilution) in rich media (YES) and incubated at 32 C with shaking of rpm for 4–6 hours. For the ectopic locus HSS strains, flow cytometry was performed essentially as described (Greenstein et al. 2018; Greenstein et al. 2019). For the MAT locus HSS strains, flow cytometry was performed using a Fortessa X20 Dual instrument (Becton Dickinson) attached with high throughput sampler (HTS) module. With a threshold of 30,000 events, samples sizes ranged from ~1000 to 30,000 cells depending on strain growth. Fluorescence detection, compensation, and data analysis were as described. The R scripts for analysis is included as a text file. Flow data deriving from the genetic screen for individual strains are represented as 2d density hexbin plots in Figure 1, 1S3, 1S5, 2S1, and 2S3. Dashed red and blue guidelines respectively

indicate median minus 2SD of “green”/“orange”-On cells (*Δclr4* control cells with normalized fluorescence above 0.5) and median plus 2SD of “green”/ “orange”-Off cells (“red”-Only control).

We note that an error occurred relative to v1 of this manuscript: .fcs files in the 3.1 version are exported with a color compensation matrix appended to each sample but not applied, in contrast to .fcs 2.0 files where compensation is applied upon export. Thus, since our R scripts assumed color compensated data to be exported, no additional compensation was applied. We noted this error during revisions and have updated our R scripts to account for this and process color compensation. We then applied a uniform 2 standard deviation threshold for all of our controls and normalization. Note that the numerical value for some spreading hits changed as a result.

Spreading Analysis.

Nucleated cells were extracted using a “green”-off gate, using median of a “red”-only control plus 2 times the SD. Enrichment of cell populations in particular “orange” fluorescence ranges (Gridn) are calculated as $Grid_n^{mut/par}$: fraction of mutant population is divided by the fraction of parent population in one grid. The intervals of “orange” fluorescence used in grids are determined by: median plus 2SD of “orange”-Off cells (“red”-Only control), median minus 2 SD of “orange”-On cells (Δclr4 control cells with normalized fluorescence above 0.5) and the median of the two. For ECT, instead of using a “red”-Only control strain, we adjusted the fluorescence value of a fluorescence-negative (unstained) strain by the “red” fluorescence from the *Δclr4* control. To evaluate gain of spreading phenotype, enrichment in Grid 1 in WT MAT, MAT ΔREIII and ECT were calculated. To evaluate loss of spreading phenotype, enrichment in Grid 3 and 4 in MAT ΔcenH and WT MAT as well as Grid 4 in MAT ΔREIII and ECT were calculated. The distribution of the $Gri_{dn}^{mut/par}$ were plotted as swarmplots with annotation of 85th percentile and median plus 2SD of parent isolates Gridnmut/par. Gene hit lists comprised mutations above median and 2SD within the 85th percentile. Upset plots were generated using the R package UpSetR (Conway et al. 2017). Beewarm plots were plotted using the R packages ggbeeswarm (Clarke 2017)

GO Complex and Sub-Complex analysis.

<u>generating the heatmap count data</u>
GO Complexes – Based on the GO Complex annotations [link] retrieved from pombase (Lock et al. 2018; Consortium 2019), GO complex membership was determined for genes identified as hits for each strain background and hit category (gain/loss). Briefly, using functions from the R package dplyr (Wickham H., François R., Henry L. and Müller K. (2020). dplyr: A Grammar of Data Manipulation. R package version 0.8.4. https://CRAN.R-project.org/package=dplyr), gene names were converted to systematic ID numbers and these systematic IDs were queried against the GO complex annotation table. The number of times a GO complex appeared per background and hit category was tabulated. Genes can be associated with any number of GO complexes depending on their annotations. However, any particular gene was only counted once per GO complex despite potentially being annotated to that GO complex by more than one evidence code. The unique list of GO complexes for all hits was determined and a matrix was computed representing the number of times each GO complex (row) was identified per strain/hit category (column). This counts matrix was used to generate the GO complex heatmap in Figure 2S1, described below.
Hit tables – Genes annotated to the seven complexes in Figure 2A,B,C were obtained from pombase (Lock et al. 2018). fkh2 was added to the Clr6 I" complex given the protein contacts described previously (Zilio et al. 2014). For the unique set of genes per panel it was determined if each gene was identified as a hit in each strain background/hit category combination. The data was summarized in a counts matrix where rows represent the unique list of genes per panel and columns represent the strain background / hit category. The counts matrix for each set of genes was used to generate the heatmaps in Figure 2A,B, C as described below.

<u>generating the heatmap clustering</u>
Using the R package ComplexHeatmap (Gu et al. 2016), both row and column dendrogram and clustering were generated using hierarchical clustering. Based on an optimal Silhouette score, the strain background / hit category (columns) were clustered into 2 clusters. The dendrogram representing complexes (Figure 2S1) or genes (Figure 2A,B, C) in rows were not separated because validations of the clustering by connectivity, Dunn index or Silhouette score were inconclusive. Clustering validations were conducted using the R package clValid (Brock, G., Pihur, V., Datta, S. and Datta, S. (2008) clValid: An R Package for Cluster Validation Journal of Statistical Software 25(4) URL: http://www.jstatsoft.org/v25/i04).

Validation Strain and Plasmid Construction.

Plasmid constructs for gene knockout validation were generated by in vivo recombination as described (Greenstein et al. 2018; Greenstein et al. 2019). S. pombe transformants were selected as described (Greenstein et al. 2018). For microscopy, hygMX super-folder GFP (SFGFP) constructs for C-terminal tagging we described previously (Al-Sady

2016) were amplified with 175bp ultramer primers with homology to apm3 or apl5 and transformed into a Swi6:E2C kanMX strain. Apm3:SFGFP;Swi6:E2C and Apl5:SFGFP;Swi6:E2C strains were selected on hygromycin B and G418. Integrations and gene knockout were confirmed by PCR.

Flow Cytometry Data Collection and Normalization for Validation.

For validation flow cytometry experiments, cells were grown as described (Greenstein et al. 2018; Greenstein et al. 2019) with the exception that cells were diluted into YES medium and grown 5-8 hours before measurement. Flow cytometry was performed as above. Depending on strain growth and the volume collected per experiment, fluorescence values were measured for ~20,000-100,000 cells per replicate. Fluorescence detection, compensation, and data analysis were as described (Al-Sady et al. 2016; Greenstein et al. 2018; Greenstein et al. 2019) with the exception that the guide-lines for boundary values of "off" and "on" states were determined using median of a Red-Only control plus 3 times the median absolute deviation (MAD) and median of Δ*clr4* minus 2 times the MAD value respectively. Validation flow cytometry plots were generated using the ggplot2 R package (Wickham 2016).

Chromatin Immunoprecipitation and Quantification.

Chromatin Immunoprecipitation (ChIP) was performed essentially as described (Greenstein et al. 2018; Greenstein et al. 2019) Bulk populations of cells for were grown overnight to saturation in YES medium. For anti-H3K9me2 ChIP, the following morning, cultures were diluted to OD 0.1 in 25mL YES and grown for 8h at 32°C and 225rpm. Based on OD measurements, 60x106 cells were fixed and processed for ChIP as previously described (Greenstein et al. 2018) without the addition of W303 carrier. For anti-MYC ChIP, 40mL cultures were grown to OD 0.4-0.7 and then incubated 30min at 18°C. Based on OD measurements, 100x106 cells were crosslinked with 1% formaldehyde at 18°C. Anti-MYC cells were lysed as described (Greenstein, 2018), except that cells were bead mill homogenized for 9 cycles. Cleared chromatin for both anti-H3K9me2 or anti-MYC ChIP samples was incubated with either 1µL of anti-H3K9me2 antibody (Abcam, ab1220) or 2µL anti-MYC antibody (Invitrogen, MA1-980, lot VL317116) overnight after a small fraction was retained as Input/WCE. DNAs were quantified by qPCR. For H3K9me2, percent immunoprecipitation (%IP, ChIP DNA/Input DNA) was calculated as described (Greenstein et al. 2018), except for Figure 2 Supplement 2, where a ratio of %IP queried locus/%IP act1 is plotted. For anti-MYC ChIP, enrichment is presented as the ratio of %IP in PAS867 or 868 (Clr6:13XMYC in PAS 332 WT or □fkh2) over %IP in PAS332 (untagged). Data was plotted in Prism (GraphPad). For comparison of different preparations of ChIP samples, %IP of mutant divided by %IP of wildtype was calculated.

ChIP-Seq Data Collection, library preparation and sequencing.

ChIP was performed essentially as above, with the following exceptions: From 60 mL cultures, 300x106 cells in logarithmic phase were fixed and processed. Sheared chromatin samples were not pre-cleared with Protein A Dynabeads, and the chromatin was directly treated with 2µL of anti-H3K9me2 antibody (Abcam 1220, Lot GR3308902-4). Barcode-indexed sequencing libraries were generated from reverse-crosslinked ChIP-DNA samples using a Kapa Hyper DNA Library Preparation Kit (Kapa Biosystems-Roche, Basel, Switzerland) and NextFlex UDI adapters (PerkinElmer, Waltham, MA). The libraries were amplified with 16 PCR cycles and cleaned with SPRI bead protocol according to the instructions of the manufactures. The fragment lengths of the sequencing libraries were verified via micro-capillary gel electrophoresis on a LabChip GX Touch system (PerkinElmer). The libraries were quantified by fluorometry on a Qubit instrument (LifeTechnologies, Carlsbad, CA), and combined in a pool at equimolar ratios. The library pool was size-selected for library molecules in the lengths of 200 to 450 bp using a Pippin-HT instrument (Sage Science, Beverly, Massachusetts). The success of the size-selection was verified on a Bioanalyzer 2100 instrument (Agilent, Santa Clara, CA). The pool was quantified with a Kapa Library Quant kit (Kapa Biosystems-Roche) on a QuantStudio 5 real-time PCR system (Applied Biosystems, Foster City, CA) and sequenced on a Illumina NextSeq 500 (Illumina, San Diego, CA) run with paired-end 40 bp reads.

ChIP-Seq Data Analysis.

Data processing for ChIP-seq analysis was performed as follows. Trimming of sequencing adaptors and sliding window quality filtering were performed using Trimmomatic v0.39 (Bolger et al. 2014). Filtered and trimmed paired-end (PE) reads were aligned to the S. pombe genome (Wood et al. 2002) with Bowtie2 v2.4.2 (Langmead and Salzberg 2012) using standard end-to-end sensitive alignment. An additional 6bp was trimmed from the 5' end of each read prior to alignment. Sorted, indexed bam files were generated using SAMtools v1.12 (Li et al. 2009). Duplicate reads were marked with Picard tools v2.25.2 "MarkDuplicates" command. Filtered bam files were generated with SAMtools "view" with the following flags [-bh -F 3844 -f 3 -@ 4 I II III mating_type_region] to retain only properly paired reads on the listed

chromosomes/contigs, and remove duplicate reads. The resulting filtered bam files were sorted and indexed with SAMtools and used for downstream genome-wide analysis. Input normalized BigWig files for signal tracks for 25bp bins were generated from the filtered bam files with the bamCompare function from deeptools v3.5.1 (Ramírez et al. 2016) using the following flags [--outFileFormat bigwig --scaleFactorsMethod readCount --operation ratio --pseudocount 1 --extendReads --samFlagInclude 64 --skipZeroOverZero --binSize 25 --numberOfProcessors 4 --effectiveGenomeSize 12591546 –exactScaling]. Fragments were counted once by including only the first mate of each pair and extending to the fragment size. For each genotype, 2 or 3 biological replicates were processed for downstream analysis. Initial whole genome clustering analyses on ChIP and Input samples and inspection for low signal to noise ratio in IGV prompted us to remove two outlier samples, one clr6-1 and wild-type respectively.

BigWig files were imported into R v4.0.3 with rtracklayer v1.50.0 (Lawrence et al. 2009). BigWig files were used to generate signal tracks comprised of the mean and confidence interval for each genotype in custom genome browser plots generated with the DataTrack() command from the Gviz Bioconductor package v1.34.1 (Hahne and Ivanek 2016). As described previously (Greenstein et al. 2019), gene annotations were imported from PomBase (Lock et al. 2018)and converted to genomic coordinates in R v3.5.1 with the make-TxDbFromGFF function from GenomicFeatures v1.32.3 (Lawrence et al. 2013) and saved out to an sqlite file. This sqlite file was imported into R v4.0.3 and used to generate feature annotations for signal tracks in Gviz with the AnnotationTrack() command.

Reads from the filtered bam files for ChIP samples were counted into either 300bp windows or 5kb bins using windowCounts() function from the Bioconductor package csaw v1.24.3 (Lun and Smyth 2016). Regions +/-1.5kb surrounding the following features (*ade6, ura4, fkh2, prw1, mat1-Mc, mat1-Mi*) were blacklisted as they represent experimental artifacts – ade6 and ura4 because their promoter and terminator regions are present in the reporter cassettes, fkh2 and prw1 because these gene's ORFs were entirely removed in certain genetic backgrounds and mat1 genes because these regions are expressed but homologous to those found in the heterochromatic MAT locus. Global background was determined from 5kb bin count matrices and interpreted onto the 300bp windows with the csaw filterWindowsGlobal() function. Only 300bp windows where the abundance exceeded a filtering threshold of 1.7 times the global median were retained resulting in 1500 windows for further analysis.

Differential Enrichment analysis was performed on these 1500 300bp windows using the DESeq2 Bioconductor package v1.30.1 (Love et al. 2014). Size Factors were calculated on the count matrices in the global 5kb bins with the estimateSizeFactors() function and applied on the global enrichment filtered 300bp windows. The model matrix for the experimental design was constructed based on genotype. Normalized counts per bin were obtained with the vst() function from DESeq2 with the parameter blind = FALSE. VST transformed counts were used as an input to principal component analysis via the prcomp() R function on the top 500 most variable bins. PCA plots were generated with ggplot2 v3.3.3 (Wickham 2016). Differential Enrichment analysis, including estimating dispersions and fitting of a negative binomial generalized linear model, was performed with the DESeq() function. Results for pairwise contrasts between genotypes were extracted as GRanges objects with the results() function. Each of the 1500 windows was annotated as belonging to global or heterochromatin location specific nucleation/spreading/euchromatic/other categories. Volcano plots were generated with ggplot2 for each comparison by plotting -log10(padj) against log2FoldChange values. Each dot represents a 300bp region tested for differential enrichment. Dots are colored by their location annotation. Coordinates for nucleator regions are derived from feature coordinates from PomBase adjusted to a multiple of 300 so that a 300bp bin can only be annotated to one category of feature. Coordinates for spreading are defined to be between or outside of nucleator regions. Euchromatic regions are defined as coordinate ranges identified as an "island" (Zofall et al. 2012), "HOOD" (Yamanaka et al. 2013), or "region" (Wang et al. 2015)as delineated in Supplemental Table S6 from (Parsa et al. 2018). A threshold for significance of padj (Benjamini-Hochberg adjusted p-value) < 0.005 and abs(log2FoldChange) > log2(2) was applied on the results of each comparison and these cutoff values are additionally annotated on the volcano plots. For each comparison, the number of significant regions of each category was tabulated. Regions called as significant for the comparison of each mutant to WT are annotated on the custom genome browser plots generated with the Gviz AnnotationTrack() command. A Venn diagram of regions where WT signal significantly exceeds signal from mutants was generated outside of the conda environment in R v4.0.5 with the venn R package v1.10.

An additional custom analysis for the MAT locus was performed starting at the genome alignment stage. A fasta file that includes the inserted "green" and "orange" color cassettes and intact atf1/pcr1 binding sites was used was used to build a genome index for bowtie2. Alignment to this custom reference was performed with bowtie2 as above.

Alignments were filtered with SAMtools to retain only properly paired reads. Multimapping and low-quality alignments were removed with a mapq filter of -q 10. In the context of this custom reference sequence, multimapping reads represent regions that align to ura4p, ade6p, and ura4t which are present at XFP reporter cassettes, IR-R and IR-L repetitive regions, and parts of the mating type cassettes. Duplicate reads were marked and removed with Picard tools. Sorted, and indexed bam files were generated with SAMtools. BigWig files for coverage signal tracks at 10bp resolution were generated from ChIP files using the deeptools bamCoverage function with the following flags [--outFileFormat bigwig --scaleFactor ## --extendReads --samFlagInclude 64 --binSize 10 --numberOfProcessors 4 --blackListFileName cenH_blacklist.bed --effectiveGenomeSize 19996 --exactScaling]. Bam files were scaled by a custom scaling factor (replacing ## above) that adjusts for the read count in the bam file from each sample's the full genome alignment to the read count of the bam file with the smallest number of reads in the full genome alignment. The regions included in the cenH element were blacklisted in this step as they are homologous to many sequences found at the centromeres and telomeres and in this analysis represent aggregate signal from all these regions. The resulting coverage BigWig files were used to generate signal tracks in R/Gviz as described above.

Microscopy.

Swi6:E2C; Apl5:SFGFP and Swi6:E2C; Apm3:SFGFP cells were grown is YES media as described. Slides (ibidi, Cat. No. 80606) were pre-coated with 100 mg/mL lectin (Sigma-Aldrich, Cat. No. L1395) diluted in water by adding lectin solution to slide for 1 min. and removing supernatant. Log-phase growing cells were applied to the slide and excess cells were rinsed off with YES. Cells were immediately imaged with a 60x objective (CFI Plan Apochromat VC 60XC WI) on a Nikon TI-E equipped with a spinning-disk confocal head (CSU10, Yokogawa) and an EM-CCD camera (Hammamatsu). Cells were imaged in brightfield and additionally excited with 488nm (SFGFP) and 561nm (E2C) lasers. Emission was collected using a 510/50 band-pass filter for GFP emission and a 600/50 band-pass filter for E2C emission. For the SFGFP and E2C channels, z-stacks were obtained at 0.3µm/slice for 11 slices total. An overlay of the maximum z-projections for SFGFP and E2C channels are shown separately from the brightfield images. Brightness and contrast were adjusted in ImageJ to clearly show both Swi6 and Apl5/Apm5 signals in the overlay. At least two isolates were imaged to confirm localization patterns.

Reverse transcription qPCR validation of context-specific spreading mutants.

For validation of context-specific spreading hits, saf5, eaf6, pht1, hip1 and gad8 mutants were crossed to PAS217 (WT-MAT), PAS332 (MAT- EIII), PAS482 (MAT- cenH), and PAS231 (ECT), respectively and mating products selected for KAN and HYG (PAS217, PAS332, and PAS482) or KAN, HYG, and NAT resistance (PAS231). For analyzing transcriptional regulation of heterochromatin regulators via Fkh2, PAS332 or PAS798 (fkh2 in PAS332) were grown as above. Two independent isolates of each strain were grown in 200 l YES in 96 well plates to log phase (OD~0.4-0.8), washed with water and flash frozen. Total RNA was extracted from cell pellets as described (Greenstein et al 2018) using the Masterpure yeast RNA extraction kit (Lucigen). cDNA was produced from 2-3 g total RNA as described (Greenstein et al 2018) using a dT primer and Superscript IV (Invitrogen) reverse transcriptase, followed by an RNaseH step to remove RNA:DNA hybrids. qPCR was performed with primers against act1, SF-GFP and mKO2, or amplicons for heterochromatin regulator transcripts indicated in Figure 4 Supplement 2. For act1 qPCR, the cDNA was diluted 1:60. qPCR was performed as described (Greenstein et al 2019).

Sucrose gradient analysis.

Sucrose gradient analysis was performed essentially as in (Nakayama et al. 2003), with several modifications. 50mls of PAS833 (Fkh2:13XMYC), PAS836 (Fkh2:TAP; Clr6:13XMYC), or PAS837 (Fkh2:13XMYC; Sds3:TAP) were grown in YES to OD~ 1, spun and washed with STOP buffer (150mM NaCl, 50mM NaF, 10mM EDTA and 1mM NaN3) and flash frozen. Cells were resuspended in 3ml ice cold HB-300 (50mM MOPS pH7.2, 300mM NaCl, 15mM MgCl2, 15mM EGTA, 60mM glycerophosphate, 0.1mM Na3VO4, 2mM DTT, 1% Triton X-100, 1mM PMSF, 200µM phenantroline, pepstatin A, leupeptin, aprotinin and 1X of EDTA-free protease-inhibitor cocktail (Roche)) and then lysed in the presence of 600µl 0.5mm zirconia beads (RPI) for 6X 1min, with 5 min rest on ice in between cycles, at the maximum setting in a bead mill homogenizer (Beadruptor-12, Omni International). The lysate was clarified by spinning at 18,000 x g for 20min. 500µl clarified lysate was applied to a 4-20% sucrose gradient in gradient buffer (50mM Tris-HCl pH 7.5, 50mM KCl, 1mM EDTA, 1mM DTT, 1mM PMSF, 200µM phenantroline, pepstatin A, leupeptin, aprotinin and 1X of EDTA-free protease-inhibitor cocktail (Roche)) and spung for 20hrs at 151,000 x g (r_{av}) at 4°C in a swinging bucket rotor (Beckman SW-41 Ti). 12 1ml fractions were taken off the gradient and incubated for 10min at RT with 100µl

0.15% deoxycholine. Proteins were then precipitated by addition of 100 l of 50% Trichloroacetic acid and incubation on ice for 30min. Precipitates were collected by centrifugation at 16,000 x g at 4°C for 10min and pellets washed twice in ice cold acetone and then resuspended din 2X SDS-laemmli buffer and proteins separated on 1 10% SDS-PAGE gel.

Co-Immunoprecipitation.

100x106 PAS 835 (Fkh2:13XMYC; Clr6:TAP) or PAS 837 (Fkh2:13XMYC; Sds3:TAP) cells were grown, lysed and the lysate clarified as above (sucrose gradient analysis) but in the following lysis buffer: 20mM HEPES pH7.6, 150mM NaCl, 1mM EDTA, 0.5% IGEPAL NP-40, 10% glycerol, 1mM PMSF, 200µM phenantroline, pepstatin A, leupeptin, aprotinin and 1X of EDTA-free protease-inhibitor cocktail (Roche)). 500µL total protein was incubated with 20µL IgG-Sepharose 6 resin (GE healthcare) for 2 hrs at 4°C with rotation. Beads were washed 4 times with lysis buffer with 350mM NaCl instead of 150mM. Proteins were eluted off washed beads in 20µL 2X SDS-laemmli buffer, separated on SDS-PAGE gels and blotted as below.

Western blot analysis.

Proteins were transferred to low-fluorescence PVDF membranes (Bio-rad) at 90min at 200mA at 4°C. Membranes were blocked in 1:1 mixture of 1XPBS : Intercept PBS blocking buffer (LiCor) and then incubated with anti-PAP (Sigma, P1291, lot 92557) or anti-MYC (Biolegend, 626802 , lot B274036) at 1:1,000 either overnight at 4°C or 90 min at RT. Membranes were washed 4X in the presence of 0.2% Tween-20 and then incubated with fluorescent anti-mouse (800nm, Rockland, 610-145-003, lot 34206) and anti-rabbit (680nm, Cell Signaling, 5366P, lot 9) at 1:5,000 and 1:15,000 respectively for 1hr at RT. Membranes were washed 4X as above, transferred to 1X PBS and imaged on a LiCor Odyssey CLx imager.

Data Availability

Raw and processed ChIP-seq data will be available via GEO upon publication of the manuscript. Code for analysis of ChIP-seq data will be deposited in Zenodo (10.5281/zenodo.5122951). Software version information will be included in conda environment yml files (2021_seqTools.yml for command line data processing and 2021_Renv.yml for analysis via R/Bioconductor).

Acknowledgments

We thank the Michael N Boddy lab for their generous gift of strains expressing tagged Clr6 I" complex subunits. We thank Sy E Redding, Carol A Gross, Douglas Myers-Turnbull and Kamir Hiam for helpful discussions on data acquisition, analysis, and interpretation, Arthur Molines for help with microscopy experiments, and Sandra Catania and Hiten D Madhani for support for chromatin immunoprecipitation experiments. This work was supported by grants from the National Institutes of Health (DP2GM123484), the National Science Foundation (NSF 2113319), and the UCSF Program for Breakthrough Biomedical Research (partially funded by the Sandler Foundation) to BA-S, and the ARCS Foundation Scholarship and Hooper Graduate Fellowship to RAG. HN and CT were supported by National Science Foundation Graduate Research Fellowships (grant number 1650113). This work was supported by grants awarded to SB from the European Union Network of Excellence EpiGeneSys (HEALTH-2010-257082). SB is a Heisenberg Program Fellow (BR 3511/BR 5-1) and Member of the Collaborative Research Center 1064 (Project-ID 213249687) funded by the Deutsche Forschungsgemeinschaft (DFG, German Research Foundation) and acknowledges infrastructural support. Flow cytometry and FACS data were generated in the UCSF Parnassus Flow Cytometry Core which is supported by the Diabetes Research Center (DRC) grants NIH P30 DK063720. The library preparation and sequencing were carried out at the DNA Technologies and Expression Analysis Cores at the UC Davis Genome Center, supported by NIH Shared Instrumentation Grant 1S10OD010786-01.

Competing interests

The authors declare no competing interests.

References

Al-Sady B, Greenstein RA, El-Samad HJ, Braun S, Madhani HD. 2016. Sensitive and Quantitative Three-Color Protein Imaging in Fission Yeast Using Spectrally Diverse, Recoded Fluorescent Proteins with Experimentally-Characterized In Vivo Maturation Kinetics. PloS one 11: e0159292.

Al-Sady B, Madhani HD, Narlikar GJ. 2013. Division of labor between the chromodomains of HP1 and Suv39 methylase enables coordination of heterochromatin spread. Mol Cell 51: 80-91.

Alabert C, Barth TK, Reveron-Gomez N, Sidoli S, Schmidt A, Jensen ON, Imhof A, Groth A. 2015. Two distinct modes for propagation of histone PTMs across the cell cycle. Genes & development 29: 585-590.

Alper BJ, Job G, Yadav RK, Shanker S, Lowe BR, Partridge JF. 2013. Sir2 is required for Clr4 to initiate centromeric heterochromatin assembly in fission yeast. The EMBO journal 32: 2321-2335.

Alves-Rodrigues I, Ferreira PG, Moldón A, Vivancos AP, Hidalgo E, Guigó R, Ayté J. 2016. Spatiotemporal Control of Forkhead Binding to DNA Regulates the Meiotic Gene Expression Program. Cell reports 14: 885-895.

Aygun O, Mehta S, Grewal SI. 2013. HDAC-mediated suppression of histone turnover promotes epigenetic stability of

heterochromatin. Nature structural & molecular biology 20: 547-554.
Bao K, Shan CM, Moresco J, Yates J, 3rd, Jia S. 2019. Anti-silencing factor Epe1 associates with SAGA to regulate transcription within heterochromatin. Genes & development 33: 116-126.
Barrales RR, Forn M, Georgescu PR, Sarkadi Z, Braun S. 2016. Control of heterochromatin localization and silencing by the nuclear membrane protein Lem2. Genes & development 30: 133-148.
Bayne EH, Bijos DA, White SA, de Lima Alves F, Rappsilber J, Allshire RC. 2014. A systematic genetic screen identifies new factors influencing centromeric heterochromatin integrity in fission yeast. Genome biology 15: 481.
Bolger AM, Lohse M, Usadel B. 2014. Trimmomatic: a flexible trimmer for Illumina sequence data. Bioinformatics (Oxford, England) 30: 2114-2120.
Braun S, Garcia JF, Rowley M, Rougemaille M, Shankar S, Madhani HD. 2011. The Cul4-Ddb1(Cdt)(2) ubiquitin ligase inhibits invasion of a boundary-associated antisilencing factor into heterochromatin. Cell 144: 41-54.
Buck V, Ng SS, Ruiz-Garcia AB, Papadopoulou K, Bhatti S, Samuel JM, Anderson M, Millar JB, McInerny CJ. 2004. Fkh2p and Sep1p regulate mitotic gene transcription in fission yeast. J Cell Sci 117: 5623-5632.
Bulmer R, Pic-Taylor A, Whitehall SK, Martin KA, Millar JB, Quinn J, Morgan BA. 2004. The forkhead transcription factor Fkh2 regulates the cell division cycle of Schizosaccharomyces pombe. Eukaryotic cell 3: 944-954.
Canzio D, Chang EY, Shankar S, Kuchenbecker KM, Simon MD, Madhani HD, Narlikar GJ, Al-Sady B. 2011. Chromodomain-mediated oligomerization of HP1 suggests a nucleosome-bridging mechanism for heterochromatin assembly. Mol Cell 41: 67-81.
Canzio D, Liao M, Naber N, Pate E, Larson A, Wu S, Marina DB, Garcia JF, Madhani HD, Cooke R et al. 2013. A conformational switch in HP1 releases auto-inhibition to drive heterochromatin assembly. Nature 496: 377-381.
Clarke ES-M, S. 2017. ggbeeswarm: Categorical Scatter (Violin Point) Plots. R. package version 0.6.0. https://CRAN.R-project.org/package=ggbeeswarm.
Cohen A, Habib A, Laor D, Yadav S, Kupiec M, Weisman R. 2018. TOR complex 2 in fission yeast is required for chromatin-mediated gene silencing and assembly of heterochromatic domains at subtelomeres. The Journal of biological chemistry 293: 8138-8150.
Consortium TGO. 2019. The Gene Ontology Resource: 20 years and still GOing strong. Nucleic acids research 47: D330-d338.
Conway JR, Lex A, Gehlenborg N. 2017. UpSetR: an R package for the visualization of intersecting sets and their properties. Bioinformatics (Oxford, England) 33: 2938-2940.
Eissenberg JC, Morris GD, Reuter G, Hartnett T. 1992. The heterochromatin-associated protein HP-1 is an essential protein in Drosophila with dosage-dependent effects on position-effect variegation. Genetics 131: 345-352.
Fischer T, Cui B, Dhakshnamoorthy J, Zhou M, Rubin C, Zofall M, Veenstra TD, Grewal SIS. 2009. Diverse roles of HP1 proteins in heterochromatin assembly and functions in fission yeast. Proc Natl Acad Sci USA 106: 8998-9003.
Garcia JF, Dumesic PA, Hartley PD, El-Samad H, Madhani HD. 2010. Combinatorial, site-specific requirement for heterochromatic silencing factors in the elimination of nucleosome-free regions. Genes & development 24: 1758-1771.
Greenstein RA, Barrales RR, Sanchez NA, Bisanz JE, Braun S, Al-Sady B. 2019. Set1/COMPASS repels heterochromatin invasion at euchromatic sites by disrupting Suv39/Clr4 activity and nucleosome stability. Genes & development 34: 99-117.
Greenstein RA, Jones SK, Spivey EC, Rybarski JR, Finkelstein IJ, Al-Sady B. 2018. Noncoding RNA-nucleated heterochromatin spreading is intrinsically labile and requires accessory elements for epigenetic stability. eLife 7.
Grewal SI, Klar AJ. 1997. A recombinationally repressed region between mat2 and mat3 loci shares homology to centromeric repeats and regulates directionality of mating-type switching in fission yeast. Genetics 146: 1221-1238.
Grewal SIS, Bonaduce MJ, Klar AJS. 1998. Histone deacetylase homologs regulate epigenetic inheritance of transcriptional silencing and chromosome segregation in fission yeast. Genetics 150: 563-576.
Grewal SIS, Klar AJS. 1996. Chromosomal inheritance of epigenetic states in fission yeast during mitosis and meiosis. Cell 86: 95-101.
Gu Z, Eils R, Schlesner M. 2016. HilbertCurve: an R/Bioconductor package for high-resolution visualization of genomic data. Bioinformatics (Oxford, England) 32: 2372-2374.
Hahne F, Ivanek R. 2016. Visualizing Genomic Data Using Gviz and Bioconductor. Methods in molecular biology (Clifton, NJ) 1418: 335-351.
Hall IM, Shankaranarayana GD, Noma KI, Ayoub N, Cohen A, Grewal SIS. 2002. Establishment and maintenance of a heterochromatin domain. Science 297: 2232-2237.
Holla S, Dhakshnamoorthy J, Folco HD, Balachandran V, Xiao H, Sun LL, Wheeler D, Zofall M, Grewal SIS. 2020. Positioning Heterochromatin at the Nuclear Periphery Suppresses Histone Turnover to Promote Epigenetic Inheritance. Cell 180: 150-164.e115.
Jacobs SA, Taverna SD, Zhang YN, Briggs SD, Li JM, Eissenberg JC, Allis CD, Khorasanizadeh S. 2001. Specificity of the HP1 chromo domain for the methylated N-terminus of histone H3. Embo Journal 20: 5232-5241.
Jia S, Noma K, Grewal SI. 2004. RNAi-independent heterochromatin nucleation by the stress-activated ATF/CREB family proteins. Science 304: 1971-1976.
Jih G, Iglesias N, Currie MA, Bhanu NV, Paulo JA, Gygi SP, Garcia BA, Moazed D. 2017. Unique roles for histone H3K9me states in RNAi and heritable silencing of transcription. Nature.
Kim HS, Choi ES, Shin JA, Jang YK, Park SD. 2004. Regulation of Swi6/HP1-dependent heterochromatin assembly by cooperation of components of the mitogen-activated protein kinase pathway and a histone deacetylase Clr6. The Journal of biological chemistry 279: 42850-42859.
Kim J-H, Saraf A, Florens L, Washburn M, Workman JL. 2010. Gcn5 regulates the dissociation of SWI/SNF from chromatin by acetylation of Swi2/Snf2. Genes & development 24: 2766-2771.
Knott SR, Peace JM, Ostrow AZ, Gan Y, Rex AE, Viggiani CJ, Tavaré S, Aparicio OM. 2012. Forkhead transcription factors establish origin timing and long-range clustering in S. cerevisiae. Cell 148: 99-111.
Krogan NJ, Keogh MC, Datta N, Sawa C, Ryan OW, Ding H, Haw RA, Pootoolal J, Tong A, Canadien V et al. 2003. A Snf2 family ATPase complex required for recruitment of the histone H2A variant Htz1. Mol Cell 12: 1565-1576.
Lachner M, O'Carroll N, Rea S, Mechtler K, Jenuwein T. 2001. Methylation of histone H3 lysine 9 creates a binding site for HP1 proteins. Nature 410: 116-120.
Langmead B, Salzberg SL. 2012. Fast gapped-read alignment with Bowtie 2. Nature methods 9: 357-359.
Lantermann AB, Straub T, Stralfors A, Yuan GC, Ekwall K, Korber P. 2010. Schizosaccharomyces pombe genome-wide nucleosome mapping reveals positioning mechanisms distinct from those of Saccharomyces cerevisiae. Nature structural & molecular biology 17: 251-U215.
Lawrence M, Gentleman R, Carey V. 2009. rtracklayer: an R package for interfacing with genome browsers. Bioinformatics (Oxford, England) 25: 1841-1842.
Lawrence M, Huber W, Pagès H, Aboyoun P, Carlson M, Gentleman R, Morgan MT, Carey VJ. 2013. Software for computing and annotating genomic ranges. PLoS computational biology 9: e1003118.
Li H, Handsaker B, Wysoker A, Fennell T, Ruan J, Homer N, Marth G, Abecasis G, Durbin R. 2009. The Sequence Alignment/Map format and SAMtools. Bioinformatics (Oxford, England) 25: 2078-2079.
Lock A, Rutherford K, Harris MA, Hayles J, Oliver SG, Bähler J, Wood V. 2018. PomBase 2018: user-driven reimplementation of the fission yeast database provides rapid and intuitive access to diverse, interconnected information. Nucleic acids research 47: D821-D827.
Lorch Y, Kornberg RD. 2017. Chromatin-remodeling for transcription. Quarterly reviews of biophysics 50: e5.

Love MI, Huber W, Anders S. 2014. Moderated estimation of fold change and dispersion for RNA-seq data with DESeq2. Genome biology 15: 550.
Lun AT, Smyth GK. 2016. csaw: a Bioconductor package for differential binding analysis of ChIP-seq data using sliding windows. Nucleic acids research 44: e45.
Marina DB, Shankar S, Natarajan P, Finn KJ, Madhani HD. 2013. A conserved ncRNA-binding protein recruits silencing factors to heterochromatin through an RNAi-independent mechanism. Genes & development 27: 1851-1856.
Meneghini MD, Wu M, Madhani HD. 2003. Conserved histone variant H2A.Z protects euchromatin from the ectopic spread of silent heterochromatin. Cell 112: 725-736.
Moazed D. 2009. Small RNAs in transcriptional gene silencing and genome defence. Nature 457: 413-420.
Nakayama J, Klar AJ, Grewal SI. 2000. A chromodomain protein, Swi6, performs imprinting functions in fission yeast during mitosis and meiosis. Cell 101: 307-317.
Nakayama J, Xiao G, Noma K, Malikzay A, Bjerling P, Ekwall K, Kobayashi R, Grewal SI. 2003. Alp13, an MRG family protein, is a component of fission yeast Clr6 histone deacetylase required for genomic integrity. The EMBO journal 22: 2776-2787.
Narlikar GJ, Phelan ML, Kingston RE. 2001. Generation and Interconversion of Multiple Distinct Nucleosomal States as a Mechanism for Catalyzing Chromatin Fluidity. Mol Cell 8: 1219-1230.
Nicetto D, Zaret KS. 2019. Role of H3K9me3 heterochromatin in cell identity establishment and maintenance. Current opinion in genetics & development 55: 1-10.
Nicolas E, Yamada T, Cam HP, FitzGerald PC, Kobayashi R, Grewal SIS. 2007. Distinct roles of HDAC complexes in promoter silencing, antisense suppression and DNA damage protection. Nature structural & molecular biology 14: 372-380.
Noma K, Cam HP, Maraia RJ, Grewal SI. 2006. A role for TFIIIC transcription factor complex in genome organization. Cell 125: 859-872.
Noma K, Sugiyama T, Cam H, Verdel A, Zofall M, Jia S, Moazed D, Grewal SI. 2004. RITS acts in cis to promote RNA interference-mediated transcriptional and post-transcriptional silencing. Nature genetics 36: 1174-1180.
Parsa JY, Boudoukha S, Burke J, Homer C, Madhani HD. 2018. Polymerase pausing induced by sequence-specific RNA-binding protein drives heterochromatin assembly. Genes & development 32: 953-964.
Ragunathan K, Jih G, Moazed D. 2015. Epigenetics. Epigenetic inheritance uncoupled from sequence-specific recruitment. Science 348: 1258699.
Ramírez F, Ryan DP, Grüning B, Bhardwaj V, Kilpert F, Richter AS, Heyne S, Dündar F, Manke T. 2016. deepTools2: a next generation web server for deep-sequencing data analysis. Nucleic acids research 44: W160-165.
Rawal Y, Chereji RV, Qiu H, Ananthakrishnan S, Govind CK, Clark DJ, Hinnebusch AG. 2018. SWI/SNF and RSC cooperate to reposition and evict promoter nucleosomes at highly expressed genes in yeast. Genes & development 32: 695-710.
Reyes-Turcu FE, Zhang K, Zofall M, Chen E, Grewal SI. 2011. Defects in RNA quality control factors reveal RNAi-independent nucleation of heterochromatin. Nature structural & molecular biology 18: 1132-1138.
Rowe CE, Narlikar GJ. 2010. The ATP-dependent remodeler RSC transfers histone dimers and octamers through the rapid formation of an unstable encounter intermediate. Biochemistry 49: 9882-9890.
Sanulli S, G JN. 2020. Liquid-like interactions in heterochromatin: Implications for mechanism and regulation. Current opinion in cell biology 64: 90-96.
Scott KC, Merrett SL, Willard HF. 2006. A heterochromatin barrier partitions the fission yeast centromere into discrete chromatin domains. Current biology : CB 16: 119-129.
Shankaranarayana GD, Motamedi MR, Moazed D, Grewal SIS. 2003. Sir2 regulates histone H3 lysine 9 methylation and heterochromatin assembly in fission yeast. Current Biology 13: 1240-1246.
Shevchenko A, Roguev A, Schaft D, Buchanan L, Habermann B, Sakalar C, Thomas H, Krogan NJ, Shevchenko A, Stewart AF. 2008. Chromatin Central: towards the comparative proteome by accurate mapping of the yeast proteomic environment. Genome biology 9: R167.
Sugiyama T, Cam HP, Sugiyama R, Noma K-i, Zofall M, Kobayashi R, Grewal SIS. 2007. SHREC, an effector complex for heterochromatic transcriptional silencing. Cell 128: 491-504.
Thon G, Bjerling KP, Nielsen IS. 1999. Localization and properties of a silencing element near the mat3-M mating-type cassette of Schizosaccharomyces pombe. Genetics 151: 945-963.
Thon G, Bjerling P, Bunner CM, Verhein-Hansen J. 2002. Expression-state boundaries in the mating-type region of fission yeast. Genetics 161: 611-622.
Thon G, Friis T. 1997. Epigenetic inheritance of transcriptional silencing and switching competence in fission yeast. Genetics 145: 685-696.
Verrier L, Taglini F, Barrales RR, Webb S, Urano T, Braun S, Bayne EH. 2015. Global regulation of heterochromatin spreading by Leo1. Open biology 5.
Volpe TA, Kidner C, Hall IM, Teng G, Grewal SIS, Martienssen RA. 2002. Regulation of heterochromatic silencing and histone H3 lysine-9 methylation by RNAi. Science 297: 1833-1837.
Wang J, Cohen AL, Letian A, Tadeo X, Moresco JJ, Liu J, Yates JR, 3rd, Qiao F, Jia S. 2016. The proper connection between shelterin components is required for telomeric heterochromatin assembly. Genes & development 30: 827-839.
Wang J, Reddy BD, Jia S. 2015. Rapid epigenetic adaptation to uncontrolled heterochromatin spreading. eLife 4.
Wen B, Wu H, Shinkai Y, Irizarry RA, Feinberg AP. 2009. Large histone H3 lysine 9 dimethylated chromatin blocks distinguish differentiated from embryonic stem cells. Nature genetics 41: 246-250.
Wickham H. 2016. ggplot2: Elegant Graphics for Data Analysis. Springer
Wirén M, Silverstein RA, Sinha I, Walfridsson J, Lee H-M, Laurenson P, Pillus L, Robyr D, Grunstein M, Ekwall K. 2005. Genomewide analysis of nucleosome density histone acetylation and HDAC function in fission yeast. The EMBO journal 24: 2906-2918.
Yamanaka S, Mehta S, Reyes-Turcu FE, Zhuang F, Fuchs RT, Rong Y, Robb GB, Grewal SI. 2013. RNAi triggered by specialized machinery silences developmental genes and retrotransposons. Nature 493: 557-560.
Yamane K, Mizuguchi T, Cui B, Zofall M, Noma K, Grewal SI. 2011. Asf1/HIRA facilitate global histone deacetylation and associate with HP1 to promote nucleosome occupancy at heterochromatic loci. Mol Cell 41: 56-66.
Yang XJ, Seto E. 2008. The Rpd3/Hda1 family of lysine deacetylases: from bacteria and yeast to mice and men. Nature reviews Molecular cell biology 9: 206-218.
Yu Y, Zhou H, Deng X, Wang W, Lu H. 2016. Set3 contributes to heterochromatin integrity by promoting transcription of subunits of Clr4-Rik1-Cul4 histone methyltransferase complex in fission yeast. Sci Rep 6: 31752.
Zenk F, Zhan Y, Kos P, Löser E, Atinbayeva N, Schächtle M, Tiana G, Giorgetti L, Iovino N. 2021. HP1 drives de novo 3D genome reorganization in early Drosophila embryos. Nature 593: 289-293.
Zhang K, Mosch K, Fischle W, Grewal SIS. 2008. Roles of the Clr4 methyltransferase complex in nucleation, spreading and maintenance of heterochromatin. Nature structural & molecular biology 15: 381-388.
Zhu J, Adli M, Zou JY, Verstappen G, Coyne M, Zhang X, Durham T, Miri M, Deshpande V, De Jager PL et al. 2013. Genome-wide chromatin state transitions associated with developmental and environmental cues. Cell 152: 642-654.
Zilio N, Codlin S, Vashisht AA, Bitton DA, Head SR, Wohlschlegel JA, Bähler J, Boddy MN. 2014. A novel histone deacetylase complex in the control of transcription and genome stability. Molecular and cellular biology 34: 3500-3514.
Zofall M, Smith DR, Mizuguchi T, Dhakshnamoorthy J, Grewal SIS. 2016. Taz1-Shelterin Promotes Facultative Heterochromatin Assembly at Chromosome-Internal Sites Containing Late Replication Origins. Mol Cell 62: 862-874.
Zofall M, Yamanaka S, Reyes-Turcu FE, Zhang K, Rubin C,

Grewal SI. 2012. RNA elimination machinery targeting meiotic mRNAs promotes facultative heterochromatin formation. Science 335: 96-100.
Zylicz JJ, Borensztein M, Wong FC, Huang Y, Lee C, Dietmann S, Surani MA. 2018. G9a regulates temporal preimplantation developmental program and lineage segregation in blastocyst. eLife 7.
Zylicz JJ, Dietmann S, Gunesdogan U, Hackett JA, Cougot D, Lee C, Surani MA. 2015. Chromatin dynamics and the role of G9a in gene regulation and enhancer silencing during early mouse development. eLife 4.

Figure 1

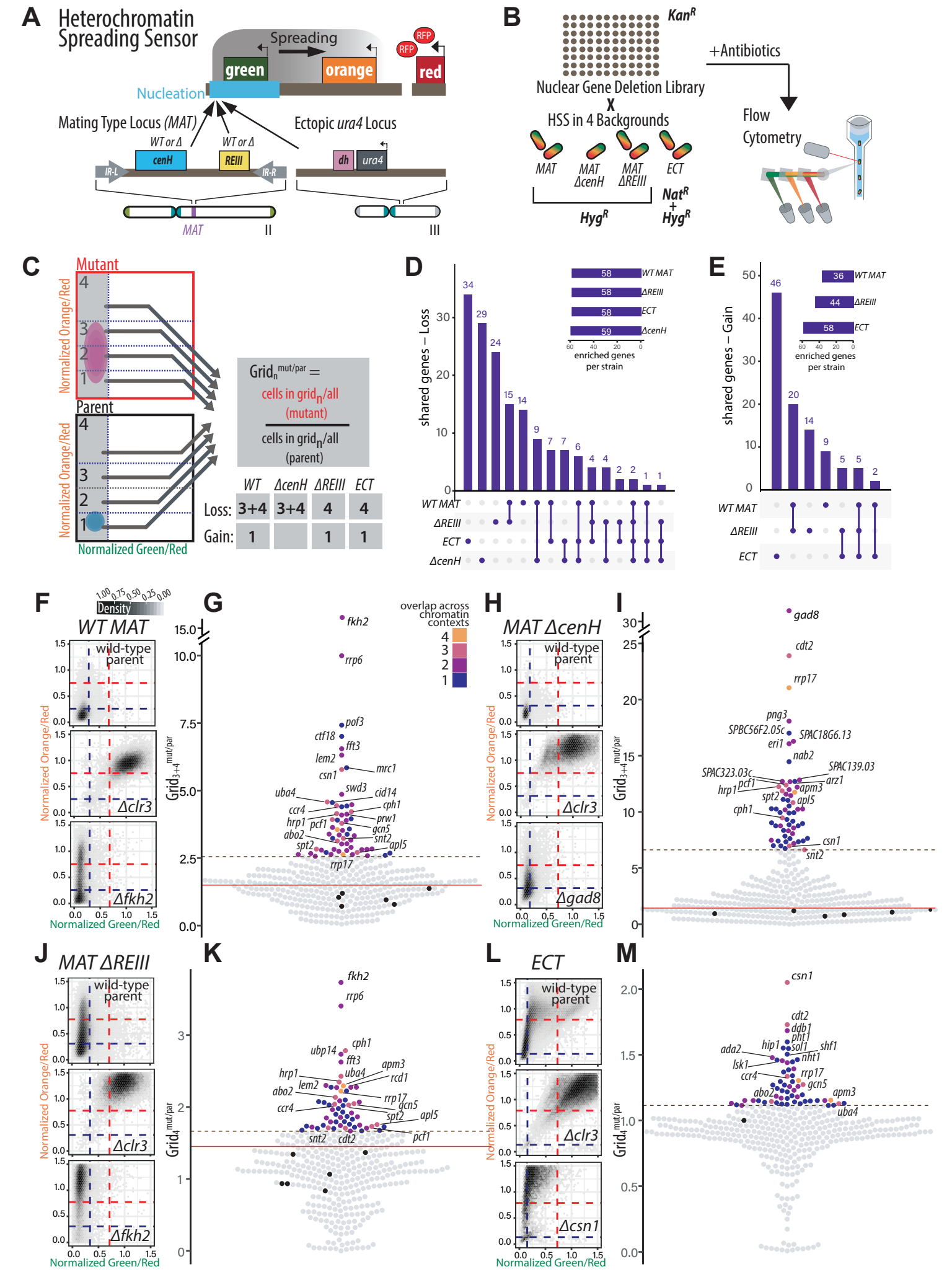
A
Heterochromatin Spreading Sensor
Spreading
green
orange
RFP
RFP
red
Nucleation
Mating Type Locus (MAT)
WT or Δ
WT or Δ
cenH
REIII
IR-L
IR-R
Ectopic ura4 Locus
dh
ura4
MAT
II
III
B
Kan^R
+Antibiotics
Nuclear Gene Deletion Library
X
HSS in 4 Backgrounds
MAT
MAT ΔcenH
MAT ΔREIII
ECT
Hyg^R
Nat^R + Hyg^R
Flow Cytometry
C
Mutant
Parent
Normalized Orange/Red
Normalized Green/Red
Grid_n^mut/par = cells in grid_n/all (mutant) / cells in grid_n/all (parent)
WT ΔcenH ΔREIII ECT
Loss: 3+4 3+4 4 4
Gain: 1 1 1
D
shared genes – Loss
enriched genes per strain
WT MAT
ΔREIII
ECT
ΔcenH
E
shared genes – Gain
F
Density
WT MAT
wild-type parent
Δclr3
Δfkh2
G
overlap across chromatin contexts
fkh2
rrp6
pof3
ctf18
fft3
lem2
mrc1
csn1
swd3
cid14
uba4
cph1
ccr4
prw1
hrp1
pcf1
gcn5
abo2
snt2
spt2
apl5
rrp17
H
MAT ΔcenH
Δgad8
I
gad8
cdt2
rrp17
png3
SPBC56F2.05c
SPAC18G6.13
eri1
nab2
SPAC139.03
SPAC323.03c
arz1
apm3
J
MAT ΔREIII
K
L
ECT
Δcsn1
M
csn1
cdt2
ddb1
pht1
sol1
shf1
ada2
hip1
nht1
lsk1
rrp17
gcn5
apm3
uba4

Figure 1: A genetic screen based on a suite of fluorescent reporters identifies heterochromatin spreading regulators in different chromatin contexts.

A. TOP: Overview of heterochromatin spreading sensor (HSS, Greenstein 2018). Three transcriptionally encoded fluorescent protein genes are integrated in the genome. *SFGFP* ("green") proximal or internal to the nucleation site allows identification of heterochromatin nucleation; *mKO2* ("orange") distal to the nucleation site allows identification of heterochromatin spreading. *3xE2C* ("red") in a euchromatin region normalizes cell-to-cell noise. BOTTOM: The endogenous mating type locus (*MAT*) and ectopically heterochromatic *ura4* locus (Greenstein 2018) were examined with the HSS in the screen. *Bona fide* mutations of the nucleators, *cenH* and *REIII*, in *MAT* were made to limit nucleation to occur from one site. See Figure 1 Supplement 1 for detailed diagrams.

B. Workflow of the screen to identify genes that contribute to heterochromatin spreading. A custom nuclear function deletion library (Table 1) was mated with four different reporter strains (*WT MAT, MAT ΔcenH, MAT ΔREIII and ECT*). The fluorescence of "green", "orange" and "red" for each mutant cell within each background are recorded by flow cytometry.

C. Overview of the spreading-specific analysis with mock distributions of cells and grids indicated. To segregate spreading from nucleation or silencing phenotypes, "green"-off populations (successful nucleation events) are isolated. Within these populations, enrichment of cell populations in particular "orange" fluorescence ranges ($Grid_n$) are calculated as $Grid_n^{mut/par}$. *E.g.* to identify loss of spreading mutants in *WT MAT*, $Grid_{3+4}^{mut/par}$ is calculated as percentage of the mutant population divided by percentage of parent population in $Grid_{3+4}$. The Grids used for analysis of gain and loss of spreading in the four chromatin contexts are indicated.

D.-E. Upset plots indicating the frequency of (**D**) Loss of Spreading, or (**E**) Gain of Spreading gene hits appearing in one or multiple chromatin contexts. For each bar, the chromatin context(s) with shared phenotypes for the underlying gene hits is indicated below the plot. The inset indicates the total number gene hits in each chromatin context of the same phenotype.

F. *WT-MAT* 2D-density hexbin plots of the wild-type parent, a strong heterochromatin loss hit (*Δclr3*), and the top loss of spreading hit of this chromatin context. Dashed blue lines indicate the values for repressed fluorescence state and dashed red lines indicate values for fully expressed fluorescence state.

G. Beeswarm plots of $Grid_{3+4}^{mut/par}$ for *WT MAT* loss of spreading hits. The top 10 hits are all annotated, and below those hits, mutants that show overlap with at least 3 other chromatin contexts are additionally annotated. Red line, 2SD above the $Grid_{3+4}^{mut/par}$ of the wild-type parent isolates (black dots); dashed brown line, the 85th percentile; Dot color, number of chromatin contexts with loss of spreading phenotype over the cutoff.

H.-I. As in F. and G., but for *WT ΔcenH.*

J.-K. As in F. and G., but for $Grid_4^{mut/par}$ of *WT ΔREIII.*

L.-M. As in F. and G., but for $Grid_4^{mut/par}$ of *ECT.*

Figure 2

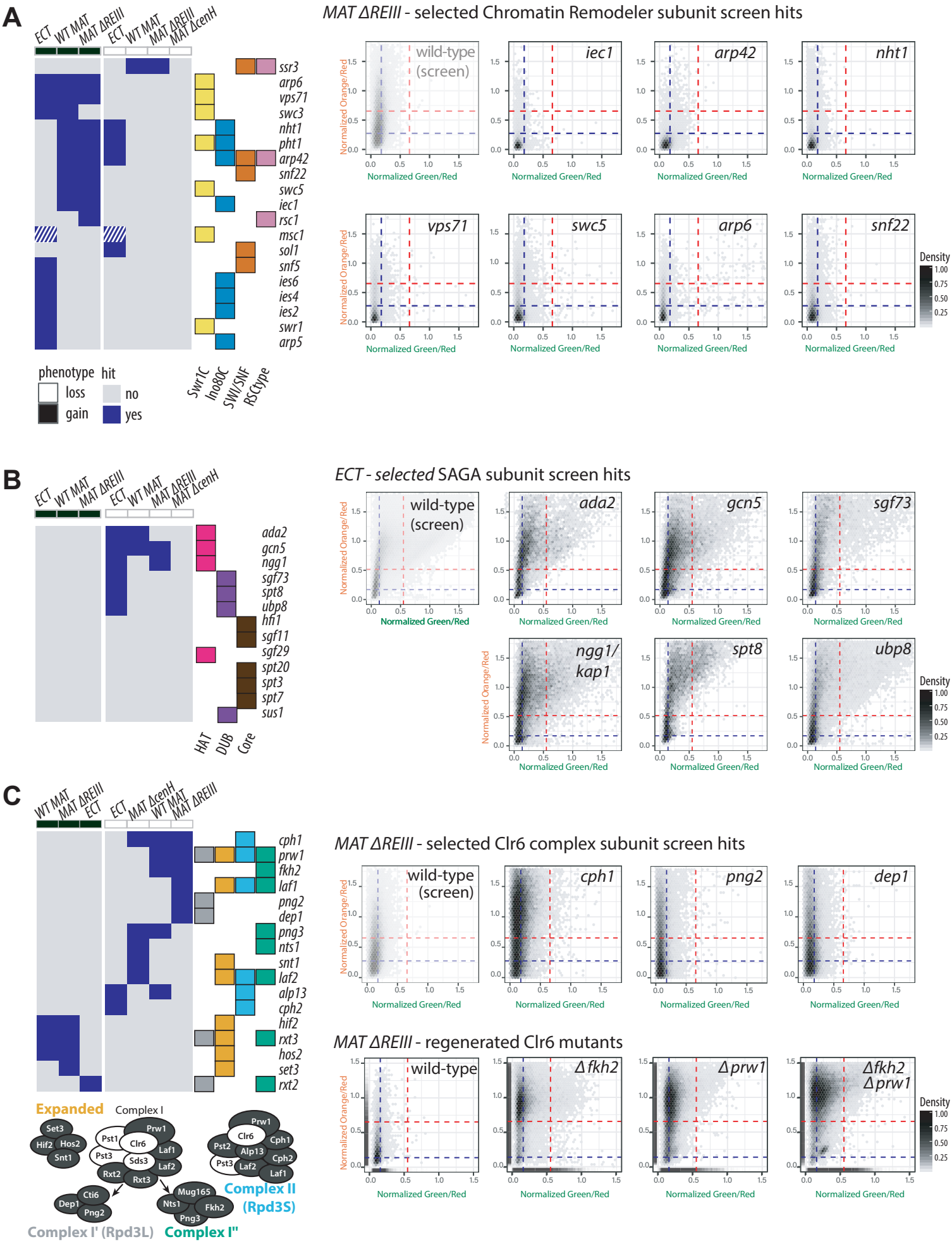
A
ECT
WT MAT
MAT ΔREIII
ECT
WT MAT
MAT ΔREIII
MAT ΔcenH
ssr3
arp6
vps71
swc3
nht1
pht1
arp42
snf22
swc5
iec1
rsc1
msc1
sol1
snf5
ies6
ies4
ies2
swr1
arp5
phenotype
loss
gain
hit
no
yes
Swr1C
Ino80C
SWI/SNF
RSCtype
MAT ΔREIII - selected Chromatin Remodeler subunit screen hits
wild-type (screen)
iec1
arp42
nht1
vps71
swc5
arp6
snf22
Normalized Orange/Red
Normalized Green/Red
Density
B
ECT - selected SAGA subunit screen hits
ada2
gcn5
ngg1
sgf73
spt8
ubp8
hfi1
sgf11
sgf29
spt20
spt3
spt7
sus1
HAT
DUB
Core
ngg1/ kap1
C
MAT ΔREIII - selected Clr6 complex subunit screen hits
cph1
prw1
fkh2
laf1
png2
dep1
png3
nts1
snt1
laf2
alp13
cph2
hif2
rxt3
hos2
set3
rxt2
png2
MAT ΔREIII - regenerated Clr6 mutants
Δfkh2
Δprw1
Δfkh2 Δprw1
Expanded
Complex I
Complex II (Rpd3S)
Complex I' (Rpd3L)
Complex I''

Figure 2: Chromatin remodeler, SAGA and Clr6 complexes regulate heterochromatin spreading.

LEFT: Table of complex members which were hits: **(A)** Swr1C, Ino80, SWI/SNF, and RSC-type chromatin remodeler complexes, **(B)** the SAGA complex, and **(C)** The Clr6 complexes Rpd3L, Rpd3L-Expanded, Rpd3S, and Clr6 I" (Bottom shows schematic of Clr6 complexes, subunits indicated in white are essential). Components identified as a hit in either showing a "gain" or "loss" of spreading phenotype for each background are marked blue, subunits that are a hit for both phenotypes (*msc1*) as white-blue crosshatched. The proteins present in each complex or subcomplex are annotated at the right with the presence of color indicating membership of that protein in the complex. For remodelers and Clr6 complexes, subunits that are not hits in any chromatin context are not included, for SAGA, all subunits except TAF_{II}s are shown. For **(C)**, Clr6 mutants that were not hits are *mug165, pst2* and *cti6*.

RIGHT: 2D density hexbin plots for selected screen hits from different families of complexes in respective background: **(A)** Chromatin remodeler gain of spreading screen hits for *MAT ΔREIII,* (**B**) SAGA loss of spreading screen hits for *ECT*, and **(C)** Clr6 complex subunit loss of spreading screen hits in *MAT ΔREIII, as well as de novo* generated Clr6 complex subunit deletion mutants. *MAT ΔREIII* and *ECT* parents shown in Figure 1 are shown here again (with transparency) for comparison. *Δfkh2, Δprw1 and Δfkh2 Δprw1* mutants were re-created *de novo* in *MAT ΔREIII.* A rug plot is included on the X and Y axes indicating the 1D density for each color. Rug lines are colored with partial transparency to assist with visualization of density changes.

Figure 3

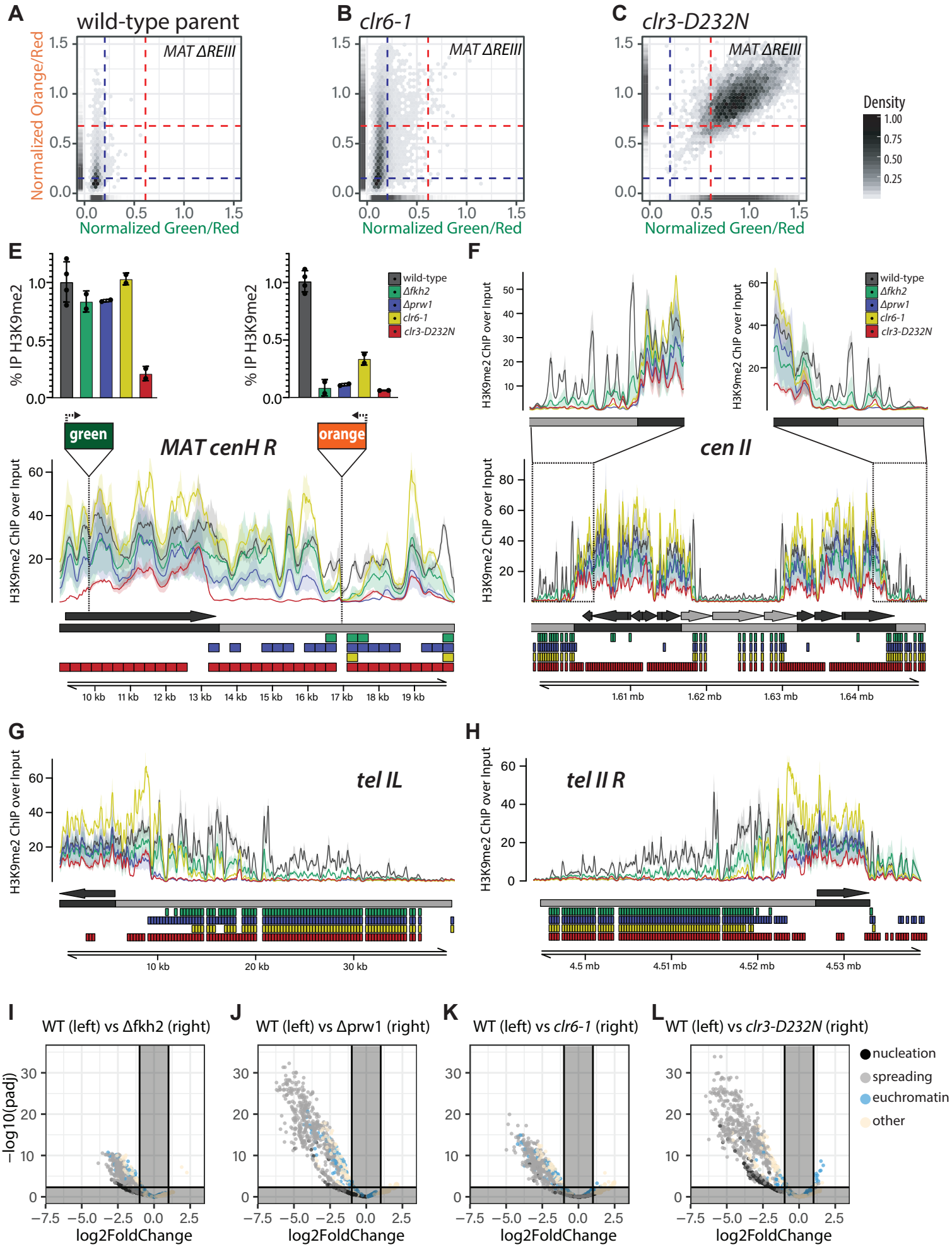
A
wild-type parent
MAT ΔREIII
Normalized Orange/Red
Normalized Green/Red
B
clr6-1
MAT ΔREIII
C
clr3-D232N
MAT ΔREIII
Density
1.00
0.75
0.50
0.25
E
% IP H3K9me2
wild-type
Δfkh2
Δprw1
clr6-1
clr3-D232N
green
orange
MAT cenH R
H3K9me2 ChIP over Input
10 kb
11 kb
12 kb
13 kb
14 kb
15 kb
16 kb
17 kb
18 kb
19 kb
F
cen II
1.61 mb
1.62 mb
1.63 mb
1.64 mb
G
tel IL
10 kb
20 kb
30 kb
H
tel II R
4.5 mb
4.51 mb
4.52 mb
4.53 mb
I
WT (left) vs Δfkh2 (right)
J
WT (left) vs Δprw1 (right)
K
WT (left) vs clr6-1 (right)
L
WT (left) vs clr3-D232N (right)
−log10(padj)
log2FoldChange
nucleation
spreading
euchromatin
other

Figure 3: Fkh2- containing Clr6 Complexes regulate heterochromatin spreading at constitutive and facultative heterochromatin loci.

A.-C. The hypomorphic *clr6-1* allele exhibits a loss of spreading phenotype, while the catalytic dead *clr3-D232N* allele loses all silencing. 2D density hexbin and rug plots in the *MAT⊿REIII* background of the parent strain (**A.**) run together with B. &C.; *clr6-1* (**B.**); and *clr3-D232N* (**C.**).

A rug plot is included on the X and Y axes indicating the 1D density for each color. Rug lines are colored with partial transparency to assist with visualization of density changes. Dashed blue lines indicate the values for repressed fluorescence state and dashed red lines indicate values for fully expressed fluorescence state.

E.-H. Visualization of H3K9me2 ChIP-Seq signals in the *MAT ΔREIII* background at the right side of the MAT locus (E.), centromere II (F.), and telomere and subtelomere IL and IIR (G.&H.). ChIP/Input normalized signal for 25bp intervals is plotted as mean (line) and 95% confidence interval (shade) for each genotype (see legend). Below the signal tracks the following annotations are present in order from top to bottom: (1) features of interest (i.e. nucleators, dark grey; non-nucleator, light grey) based on coordinates and strand derived from Pombase. (2) Nucleation and spreading annotation zones (based on (1)) are represented by dark grey and light grey boxes respectively. Spreading zones are defined to be between or outside of nucleation zones. (3-6) 300bp regions determined to be significantly differentially enriched for the comparisons between *⊿fkh2* and wild-type (green), *⊿prw1* and wild-type (blue), *clr6-1* and wild-type (yellow), *clr3-D232N* and wild-type (red) are annotated as colored boxes respectively. In E., bars above signal tracks indicate wild-type normalized H3K9me2 ChIP-RTqPCR signals for indicated genotypes conducted independently of the ChIP-Seq experiment at “green” and “orange” reporters. Error bars represent 1SD.

I.-L. Volcano plots representing -log10(adjusted p-value) vs log2FoldChange values for mutants (I., *⊿fkh2;* J., *⊿prw1;* K, *clr6-1;* L., *clr3-D232N*) over WT. P-values were corrected for multiple testing with the Benjamini-Hochberg procedure. Cutoff values for adjusted p-value < 0.005 and absolute value Log2FoldChange > 1 are annotated on the plot. Dots represent individual 300bp windows tested for differential enrichment. Dots are colored by their annotation to nucleation or spreading zones, presence within a previously identified euchromatin embedded H3K9me2 heterochromatin region (“island”, “HOOD”, or “region”), or regions outside these categories (other).

Figure 4

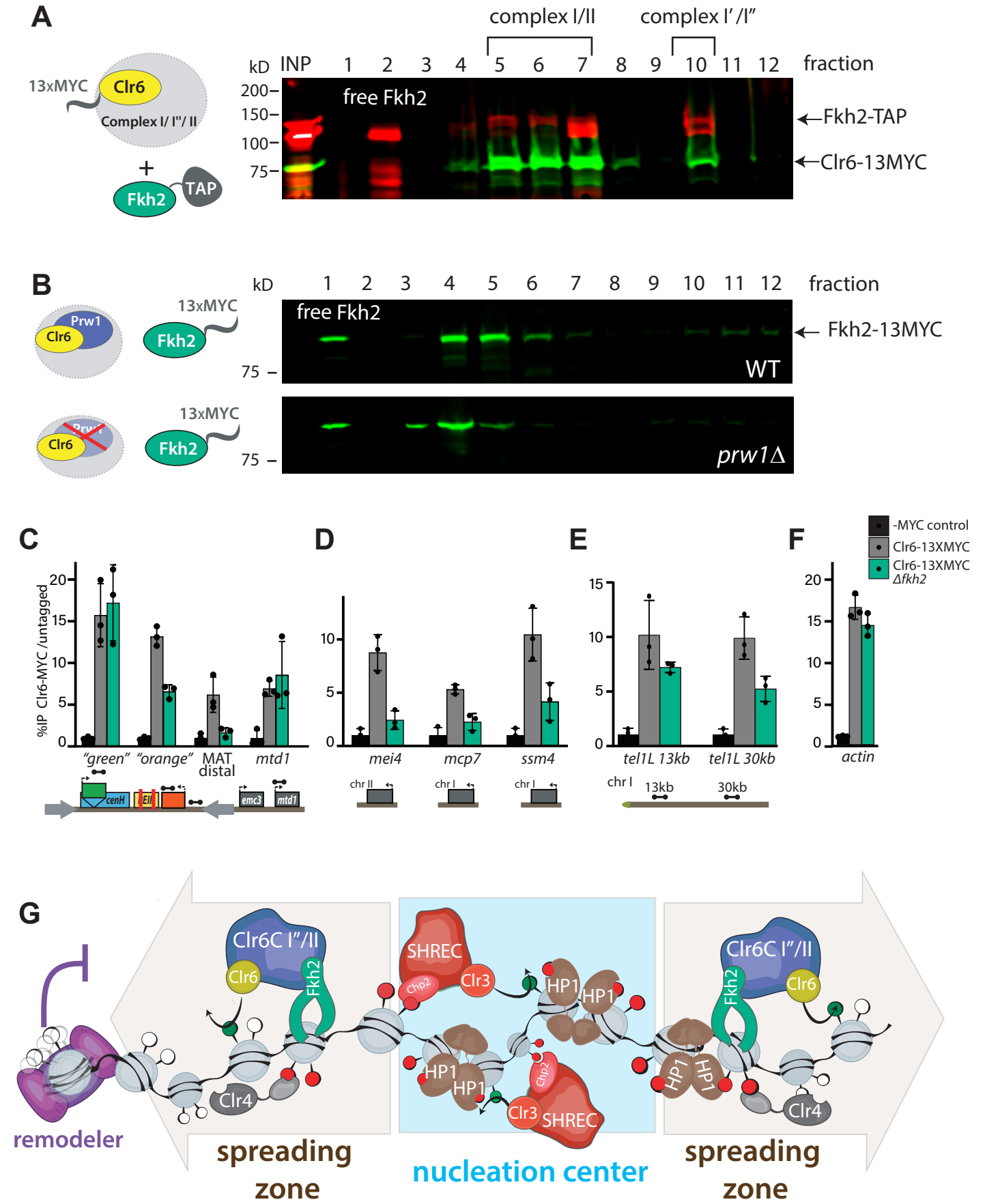
A
13xMYC
Clr6
Complex I/ I"/ II
+
Fkh2
TAP
kD
INP
1 2 3 4 5 6 7 8 9 10 11 12
fraction
complex I/II
complex I' /I"
free Fkh2
200–
150–
100–
75–
Fkh2-TAP
Clr6-13MYC
B
Prw1
Clr6
13xMYC
Fkh2
kD
1 2 3 4 5 6 7 8 9 10 11 12
fraction
free Fkh2
Fkh2-13MYC
75 –
WT
prw1Δ
C
D
E
F
-MYC control
Clr6-13XMYC
Clr6-13XMYC Δfkh2
%IP Clr6-MYC /untagged
"green"
"orange"
MAT distal
mtd1
cenH
Ell
emc3
mei4
mcp7
ssm4
chr II
chr I
tel1L 13kb
tel1L 30kb
13kb
30kb
actin
G
Clr6C I"/II
Clr6
Fkh2
Clr4
remodeler
SHREC
Chp2
Clr3
HP1
spreading zone
nucleation center
spreading zone

Figure 4: Fkh2 is a constituent member of multiple Clr6 complexes and directs Clr6 to nucleation-distal heterochromatin regions.

A. Fkh2 co-migrates with medium sized and large Clr6 complexes. Western blot against TAP (red) and MYC (green) on fractions of a sucrose density gradient of whole cells extract containing Fkh2-TAP and Clr6-MYC. Fkh2 migrates as a free protein on top of the gradient and in both major peaks of Clr6. Complex annotation based on Nicolas et el., 2007.

B. Fkh2 migration in sucrose gradients depends on Prw1. Western blot against MYC (green) on fractions of a sucrose density gradient of wild-type (WT) or *Δprw1* whole cell extract containing Fkh2:MYC. While the free Fkh2 fraction is not affected by the absence of Prw1, the medium and large peak fractions shift towards the top of the gradient.

C.-F. Clr6 chromatin localization in heterochromatin spreading areas and heterochromatin islands depends partially on Fkh2. Clr6:MYC ChIP qPCR in wild-type (Clr6-13XMYC) or *Δfkh2* (Clr6-13XMYC *Δfkh2*) background relative to an untagged (-MYC) control, in *MATΔREIIII* at the HSS reporter and downstream (C.), heterochromatin islands (D.), tel1L (E.), and *act1* (F).

G. Model for control of heterochromatin spreading by Clr3, Clr6 and chromatin remodeler complexes. The Clr3- containing SHREC complex is essential for heterochromatin assembly at noncoding RNA-driven nucleation centers, such as *cenH, dg/dh* repeats or *tlh1/2.* There, SHREC activity enables normal HP1 and Clr4 H3K9 methylase activity and is upstream to the spreading process. In the spreading zone specifically, Fkh2-containing Clr6 complexes (complex I" or complex II) are required to propagate H3K9 methylation and gene silencing. Fkh2 recruits Clr6 to nucleation center-distal chromatin. Chromatin remodelers repel spreading via nucleosome destabilization, thus hinder the “guided-state” nucleosome-to-nucleosome spreading mechanism of Clr4.

Figure 1 - Supplement 1

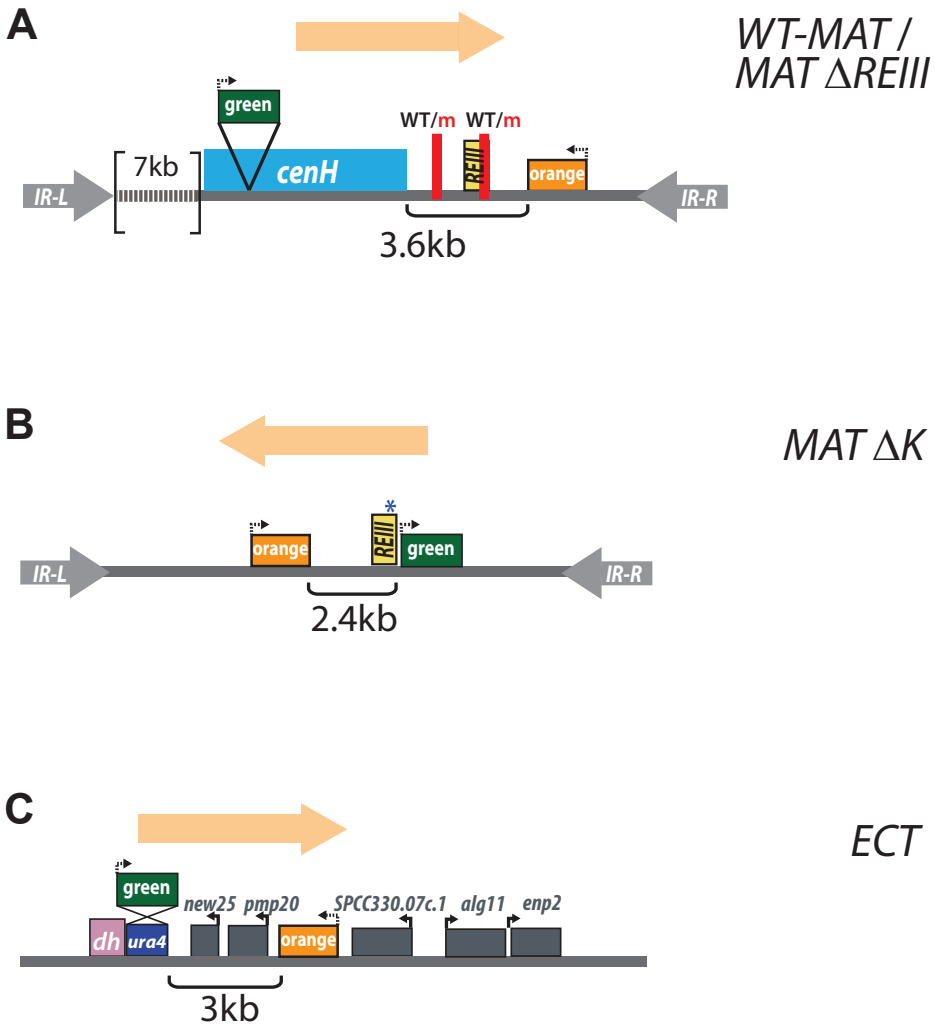

Figure 1 Supplement 1: Screen chromatin contexts with "green" and "orange" reporters.

To-scale diagrams of the heterochromatin spreading sensors (without the euchromatically placed "red" reporter) in the 4 chromatin contexts used for the spreading screen (as in Greenstein et al 2018). The direction in which spreading is analyzed ("green" to "orange") is indicated per chromatin context.

A. *WT MAT* and *MAT ΔREIII.* These two contexts are similar, except that *MAT ΔREIII* contains two short 7bp deletions of the two Atf1/Pcr1 DNA binding sites near *REIII*, inactivating it. The first binding site is not included in *REIII*, per the definitions of (Thon et al. 1999) and (Jia et al. 2004).

B. *MAT ΔcenH.*

C. *ECT.*

In Greenstein et al 2018, the distance between "green" and "orange" was varied for B. and C. contexts, without changes to the qualitative behavior of spreading.

Figure 1 Supplement 2

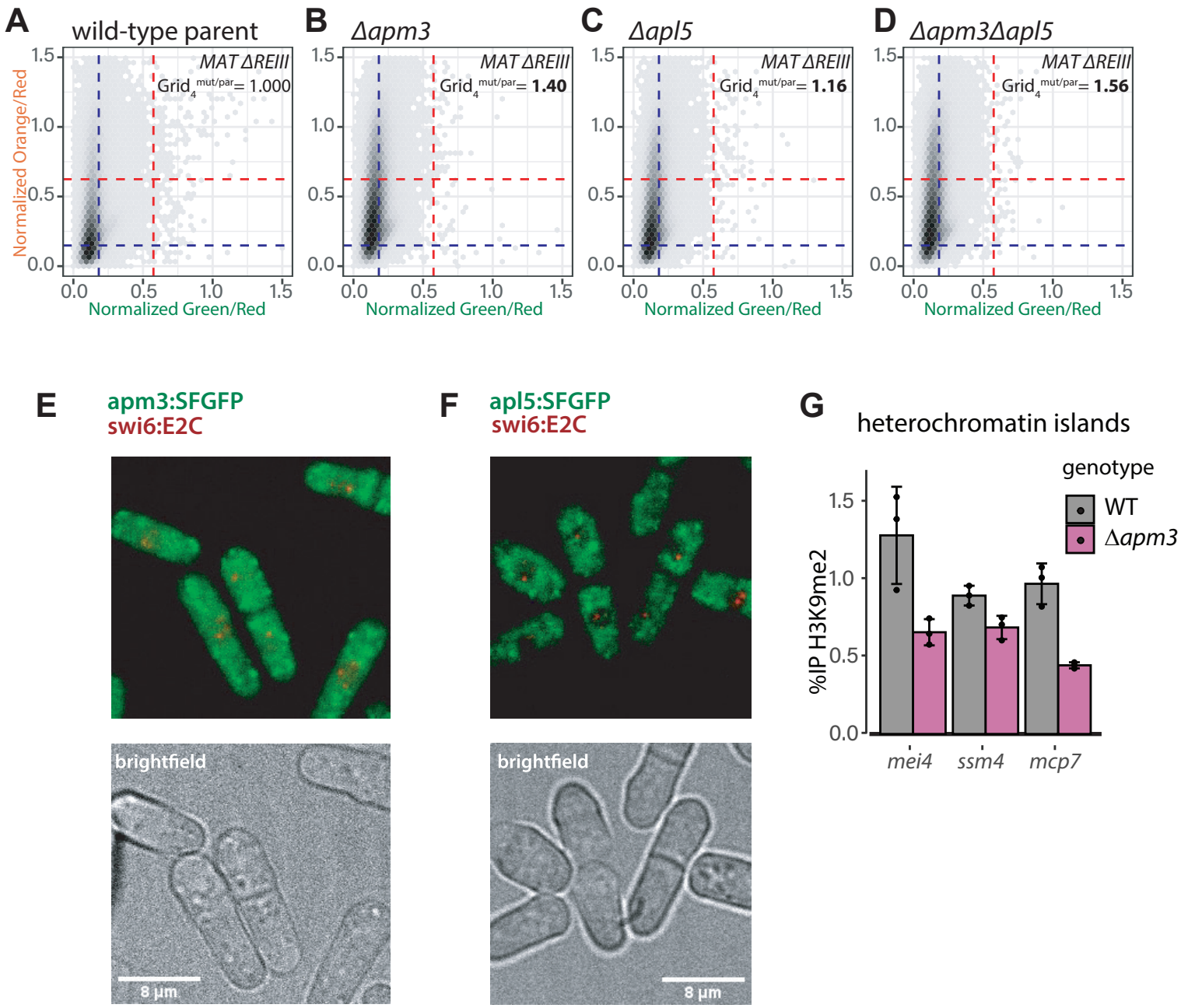

Figure 1 Supplement 2: *apm3* and *apl5*, coding for nuclear-cytosolic and cytosolic proteins, respectively, act together in modulation of heterochromatin spreading.

A.-D. 2D density hexbin plots of *de novo* generated *Δapm3* (B.), *Δapl5* (C.), and *Δapm3Δapl5* double mutant (D.) compared to the wild-type *MAT ΔREIII* parent (A.). The Fold change of $Grid_4^{mut/par}$ is indicated in the plot. At least 3 independent isolates of each genotype are combined in each plot.
E. Apm3:SFGFP is distributed in the cytosol and nucleus. Apm3:SFGFP was expressed from its native locus and co-expressed with Swi6:E2C. Swi6:E2C labels nuclear heterochromatin. Z-projection overlays of the Apm3:SFGFP and Swi6:E2C on top, and a brightfield image on the bottom.

F. Apl5:SFGFP is largely nuclear excluded. Apl5:SFGFP was expressed from its native locus and co-expressed with Swi6:E2C. Swi6:E2C labels nuclear heterochromatin. Z-projection overlays of the Apl5:SFGFP and Swi6:E2C on top, and a brightfield image on the bottom.

G. *Δapm3* exhibits a mild defect in H3K9me2 accumulation at heterochromatin islands. H3K9me2 ChIP-qPCR in wild-type parent *MAT ΔREIII* or *Δapm3* mutant.

Figure 1- Supplement 3

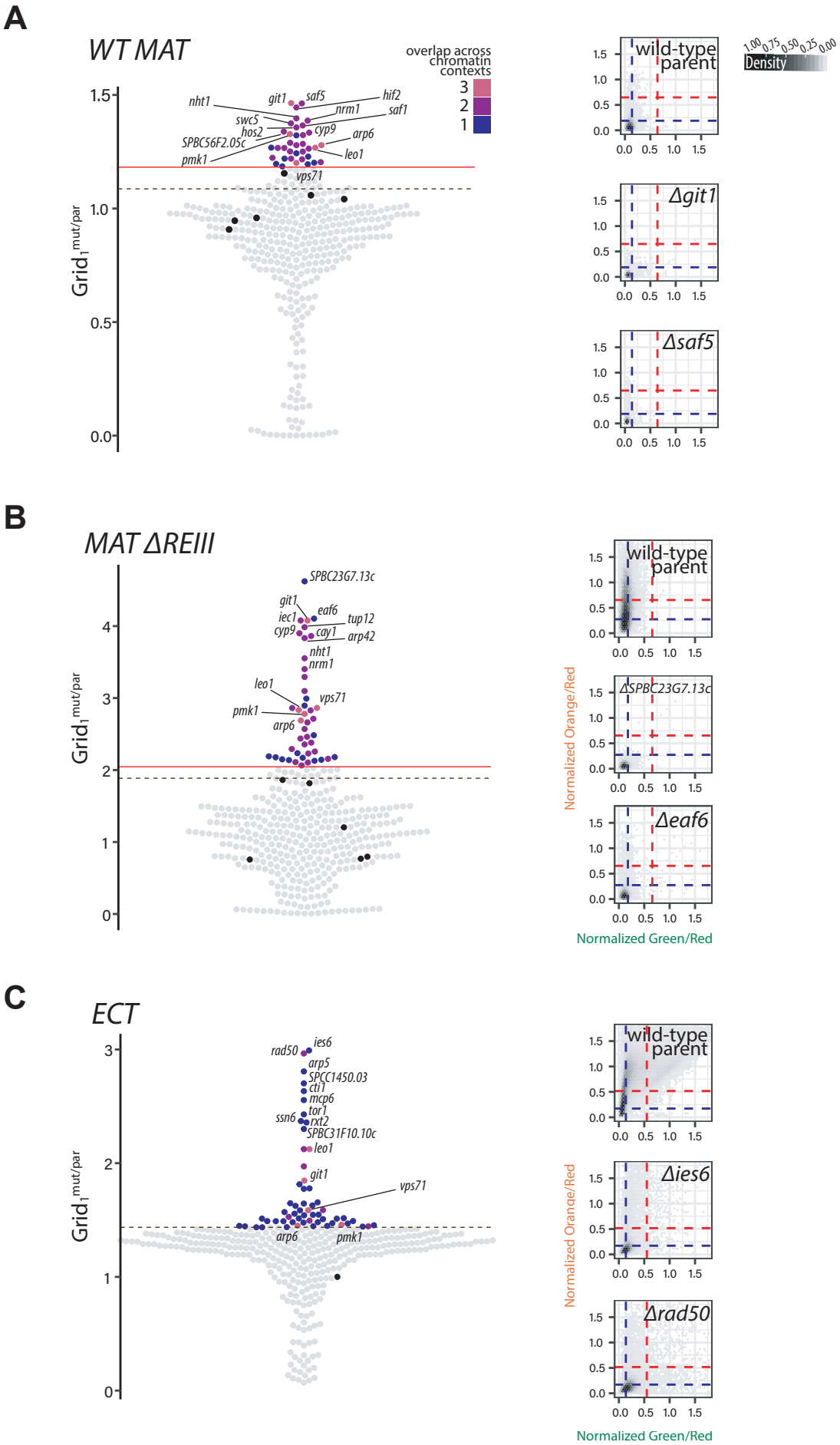

Figure 1 Supplement 3: Swarm- and 2D density hexbin plots for gain of spreading.

A. LEFT: Beeswarm plots of $Grid_1^{mut/par}$ for *WT MAT* gain of spreading hits. The top 10 hits are all annotated, and below those hits, mutants that show overlap with 2 other chromatin contexts are additionally annotated. Red line, 2SD above the $Grid_1^{mut/par}$ of wild-type parent isolates(black dots); dashed brown line, the 85th percentile; Dot color, number of chromatin contexts with loss of spreading phenotype over the cutoff. RIGHT: *WT-MAT* 2D-density hexbin plots of the wild-type parent, and the two top gain of spreading hit of this chromatin context. Dashed blue lines indicate the values for repressed fluorescence state and dashed red lines indicate values for fully expressed fluorescence state.
B. As in A. but for *MAT ΔREIII.*

C. As in A. but for *ECT.*

Figure 1 Supplement 4

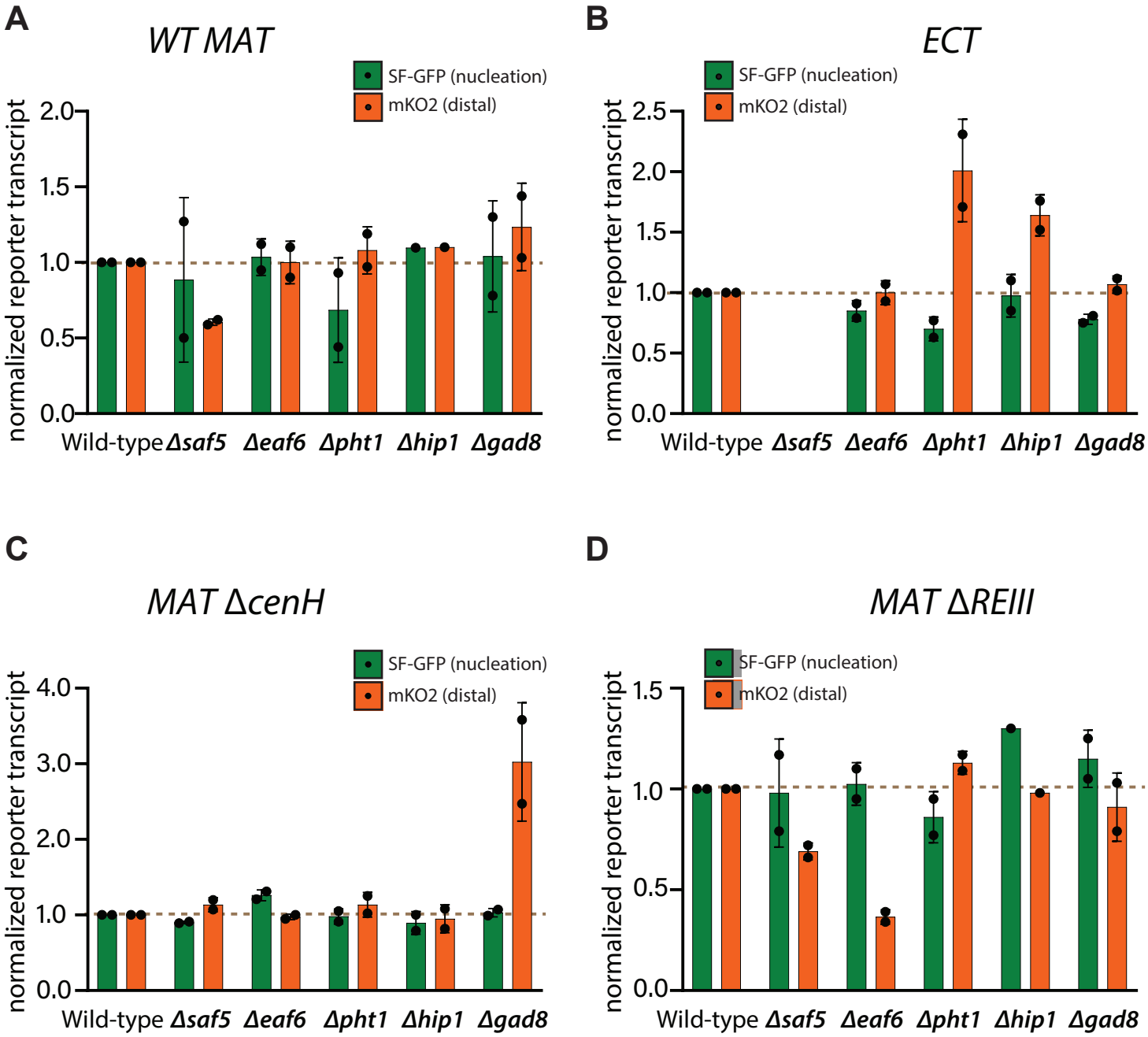

Figure 1 Supplement 4: RT-qPCR validations of selected chromatin-context unique loss and gain of spreading hits.
5 moderate- to strong hits in the loss and gain of spreading category that are partially or fully chromatin context-specific were selected for validations: *saf5* (gain of spreading in *WT MAT*, and moderately in *MAT ΔREIII*), *eaf6* (gain of spreading only in *MAT ΔREIII*), *pht1* and *hip1* (loss of spreading only in *ECT*), and *gad8* (strong loss of spreading in *MAT ΔcenH* and mildly in *ECT*). RT-qPCRs for SF-GFP ("*green*"-nucleation) and mKO2 (*"orange",* spreading) transcripts normalized to the *act1* transcript are shown for **A.** *WT-MAT,* **B.** *ECT,* **C.** *MAT ΔcenH,* and **D.** *MAT ΔREIII.* Error bars indicate 1SD of 2 biological replicates generated independently from the screen. Note we could not recover *Δsaf5* mutants in *ECT.*

Figure 1 Supplement 5

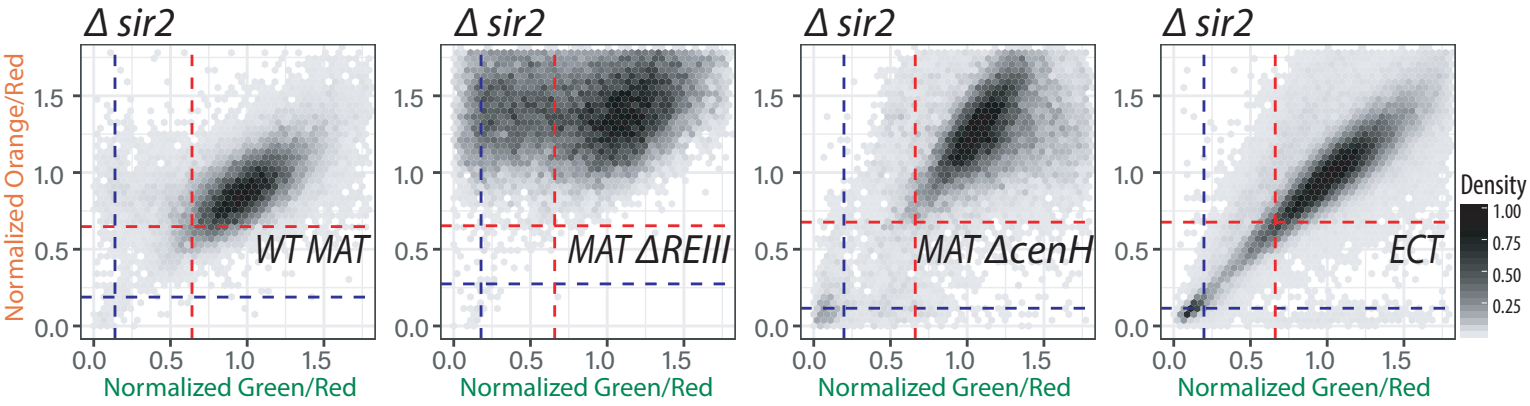

Figure 1 Supplement 5: Class III HDAC family Sir2 is required for heterochromatin silencing.

2D density hexbin plots of *Δsir2* mutants in each chromatin context from the screen. Mutation in *sir2* causes a loss of silencing phenotype in all examined chromatin context.

Figure 2 Supplement 1

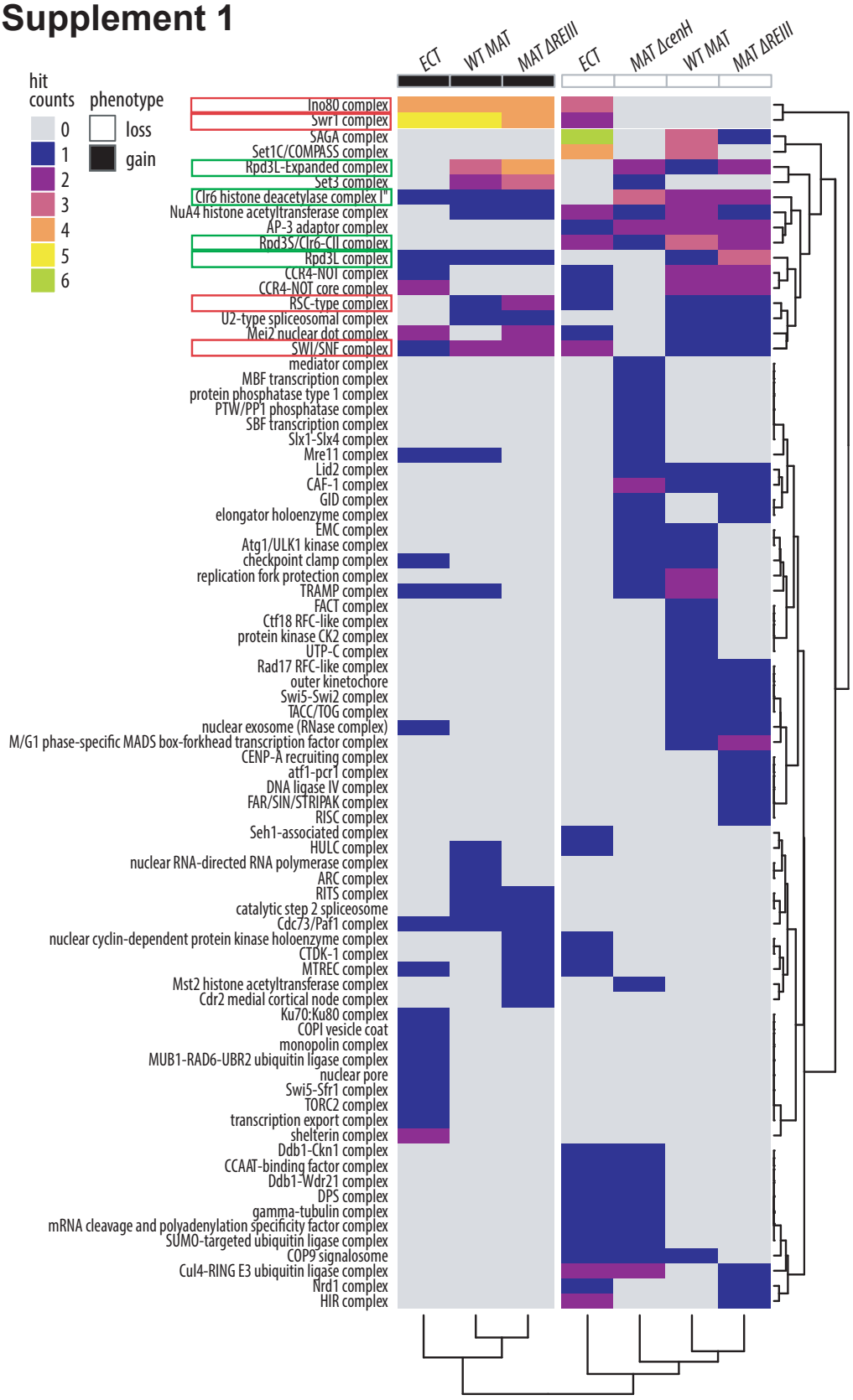

Figure 2 Supplement 1: Heterochromatin spreading is regulated by sets of unique and common protein complexes across different chromatin contexts.

Heatmap of GO complex annotations for hits in each category and strain. Rows, representing GO complexes annotated to genes within the screen that were identified as hits, are arranged via hierarchical clustering. Columns are defined by the hit phenotype (loss of spreading – white; gain of spreading – black), and each screen chromatin context is indicated at the top. The columns were clustered by hierarchical clustering and the dendrogram was cut to define 2 branches. Red boxes, chromatin remodeling complexes; Green boxes, Clr6 complexes (Note that Rpd3L Expanded includes Set3C).

Figure 2 Supplement 2

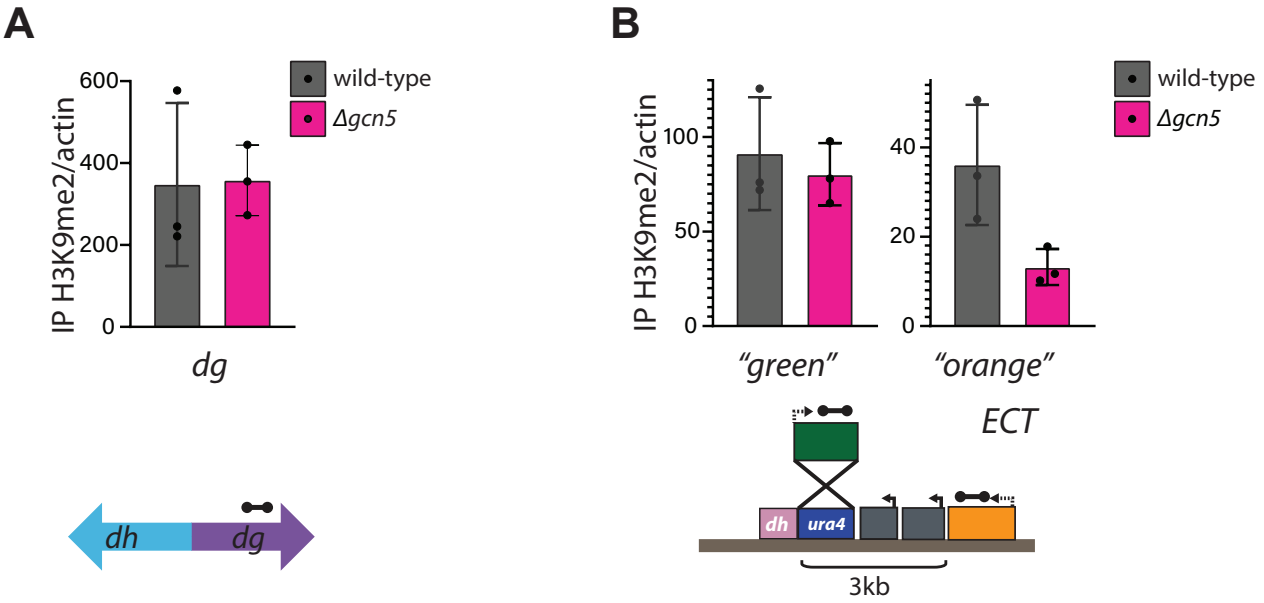

Figure 2 Supplement 2: *gcn5* is specifically required for H3K9me2 spreading at the *ECT* heterochromatin spreading sensor, but not pericentromeric heterochromatin.

act1-normalized ChIP-qPCR for H3K9me2 in *ECT* wild-type parent or the *de novo* generated *Δgcn5* mutant at **A.** the pericentomeric *dg* element, and **B.** the heterochromatin spreading sensor at the *ura4* locus in *ECT.* Dumbbells indicate qPCR amplicons. Error bars indicate 1SD of 3 biological replicates.

Figure 2 Supplement 3

MAT ΔREIII - Clr6 Subcomplex Components

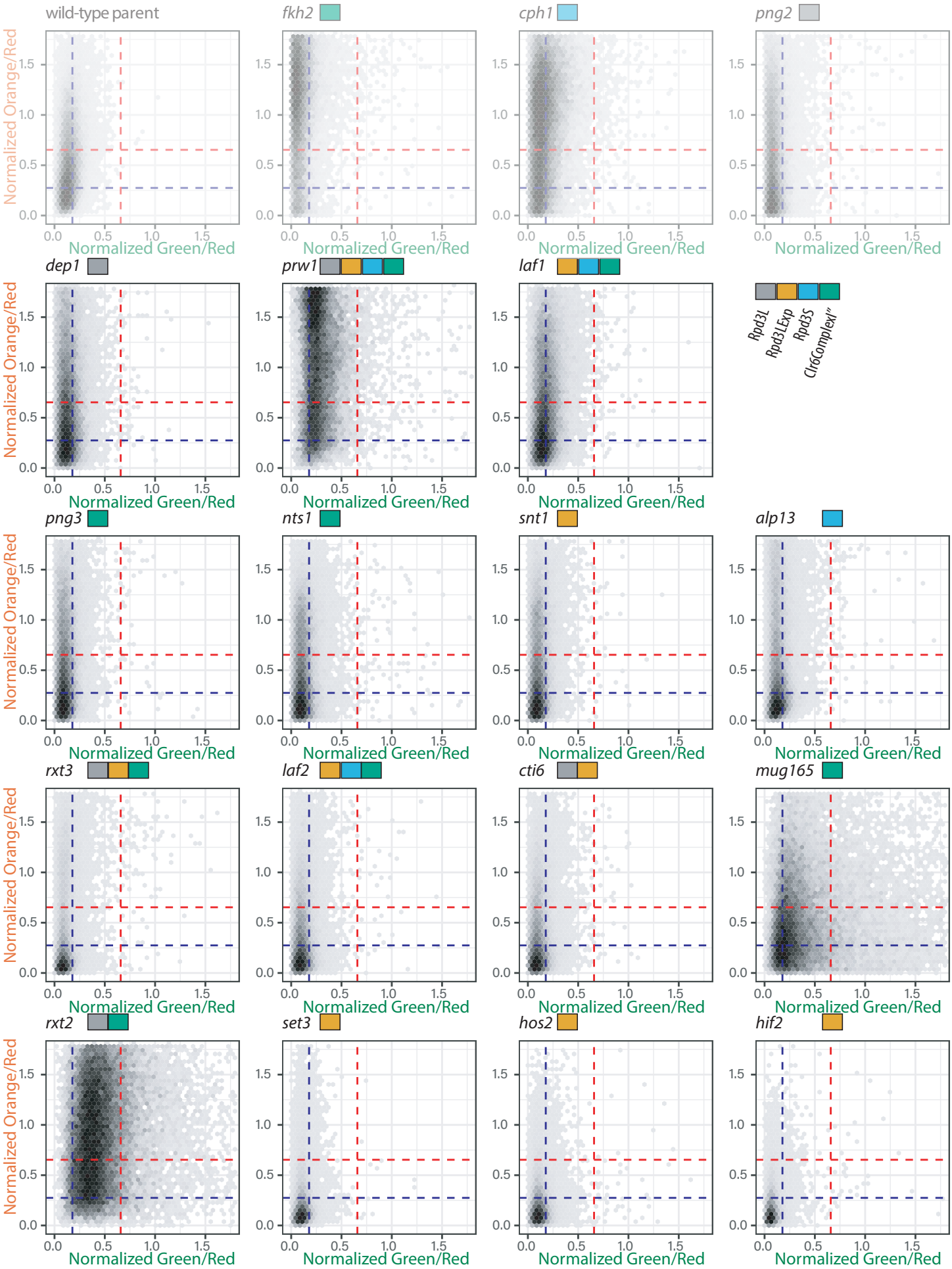

Figure 2 Supplement 3: 2D density hexbin plots for all Clr6 complex subunit screen mutants in *MAT ΔREIII.*

2D density hexbin plots of all Clr6 complexes gene mutants from the screen, corresponding to Figure 2C in *MAT ΔREIII* context. The mutants are arranged in descending order of $Grid_{3+4}^{mut/par}$; in *MAT ΔREIII* only *Δfkh2, Δcph1, Δpng2, Δdep1, Δprw1* and *Δlaf1* were identified as loss of spreading phenotype. Original *MAT ΔREIII* wild type parent and mutants shown in Figure 2 are shown here again (with transparency) for comparison. GO complex annotations are indicated next to each mutant by colored boxes.

Figure 3 - Supplement 1

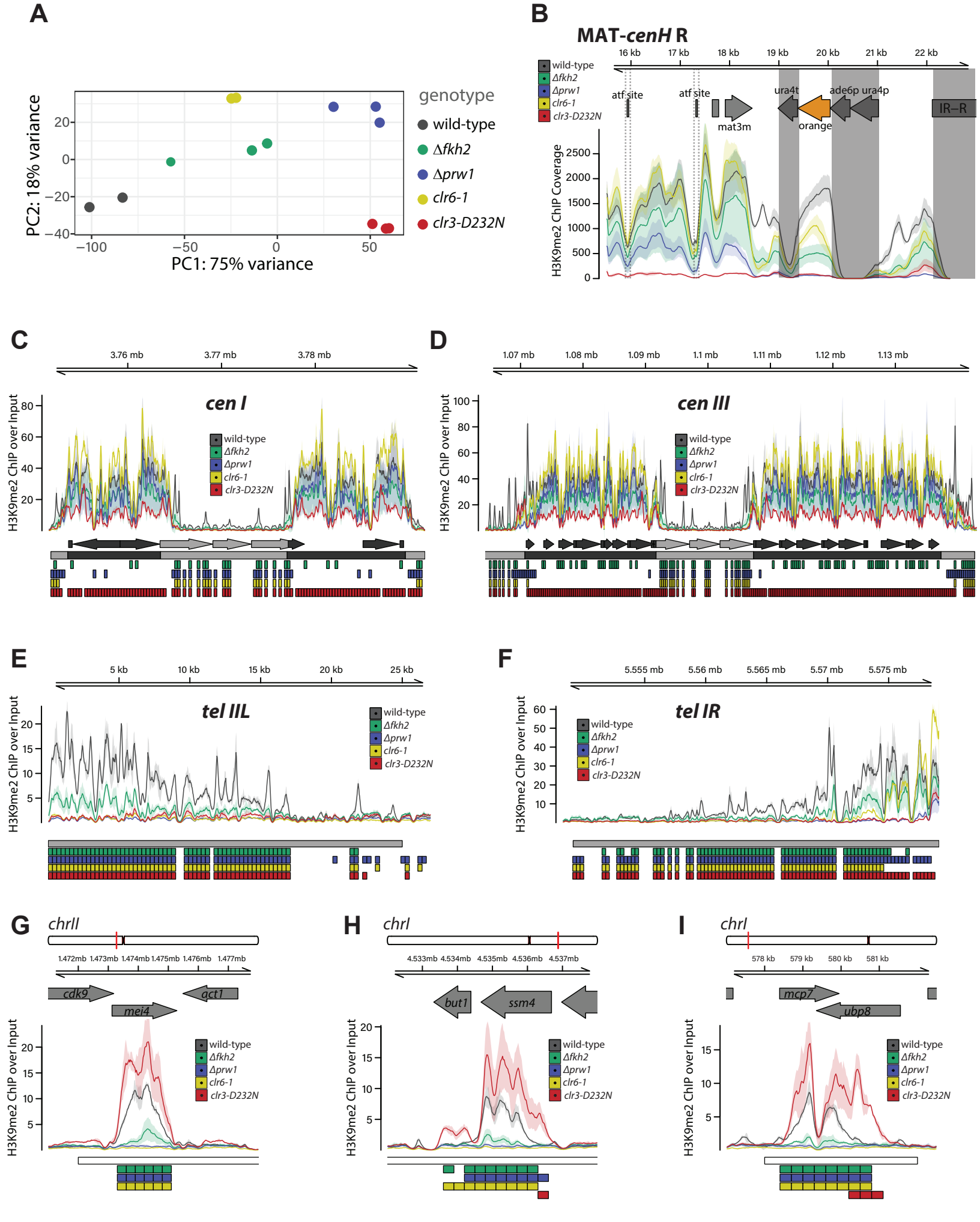

Figure 3 Supplement 1: Fkh2- containing Clr6 complexes direct H3K9me2 spreading at multiple genomic regions.

A. Principal Component Analysis was performed on the normalized counts in the top 500 most variable bins passing a threshold for global enrichment of H3K9me2 signal (see methods). The first two principal component values are plotted for each sample with genotypes as defined in the legend.

B. Alignment was performed to a custom mating type region contig in *MAT ΔREIII* with green and orange color cassettes. ChIP signal for 10bp intervals is plotted as mean (line) and 95% confidence interval (shade) for each genotype (see legend). ChIP signal represents the coverage of each interval adjusted for the sequencing depth of the full genome bam file relative to that of the full genome bam file with the lowest depth. Features of interest are annotated above the signal tracks. During data processing for alignment to this custom contig, reads mapping to multiple locations within the reference sequence were removed. For this reason, there is little to no signal over regions that are homologous within this reference including *ura4p*/*ade6p* at the color cassette promoters, *ura4t* at the color cassette terminators, and *IR-L* and *IR-R* elements (these regions are shaded). Signals at feature "atf site" (indicated by dashed box) are reduced as both 7bp sites in *MAT ΔREIII* are deleted.

C.-F. Signal tracks plots for indicated centromeres and telomeres as in the main text. No nucleator sequences are present on subtelomeres I right and II left so the first annotation row below the signal tracks is empty.

G.-I. Signal tracks for *mcp7, mei4, ssm4* islands are plotted as in the main text. Genes are annotated above the signal tracks. Below the signal tracks the following annotations are present in order from top to bottom: (1) previously identified euchromatin embedded H3K9me2 heterochromatin region ("island", "HOOD", or "region") annotated as a white box. (2-5) 300bp regions determined to be significantly differentially enriched for the comparisons between *Δfkh2* and wild-type [green], *Δprw1* and wild-type [blue], *clr6-1* and wild-type [yellow], *clr3-D232N* and wild-type [red] respectively annotated as colored boxes.

Figure 3 - Supplement 2

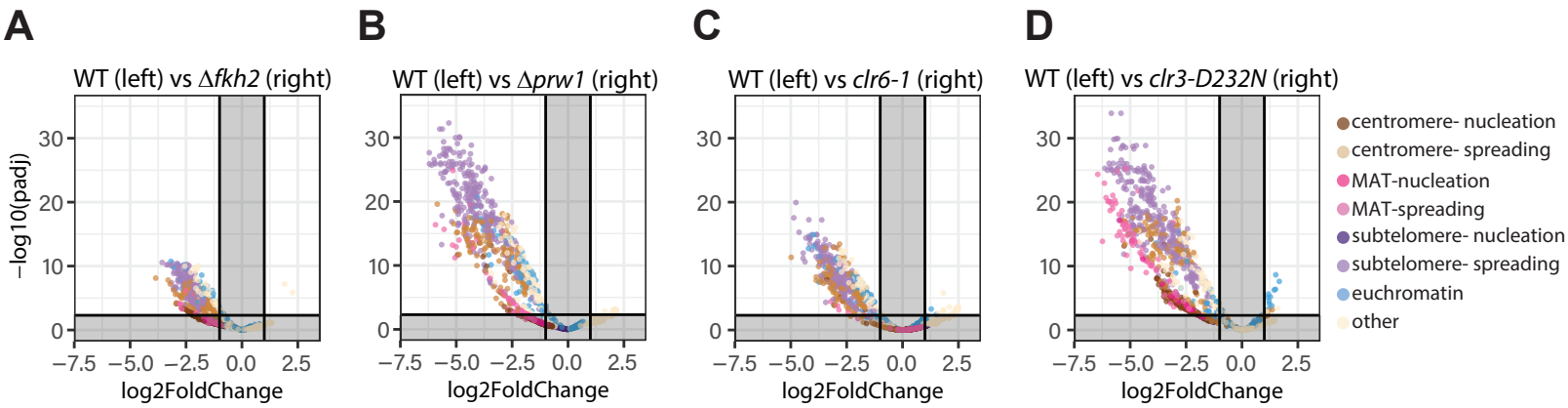

E

comparison	nucleator	spreading	other	euchromatin
Δfkh2 v. WT Δfkh2↑	0	0	2	0
Δfkh2 v. WT WT↑	73	383	67	77
Δprw1 v. WT Δprw1↑	0	0	12	0
Δprw1 v. WT WT↑	22	490	122	92
clr6-1 v. WT clr6-1↑	2	0	15	0
clr6-1 v. WT WT↑	6	383	91	88
clr3-D-N v. WT clr3-D-N↑	0	3	2	12
clr3-D-N v. WT WT↑	345	524	92	31

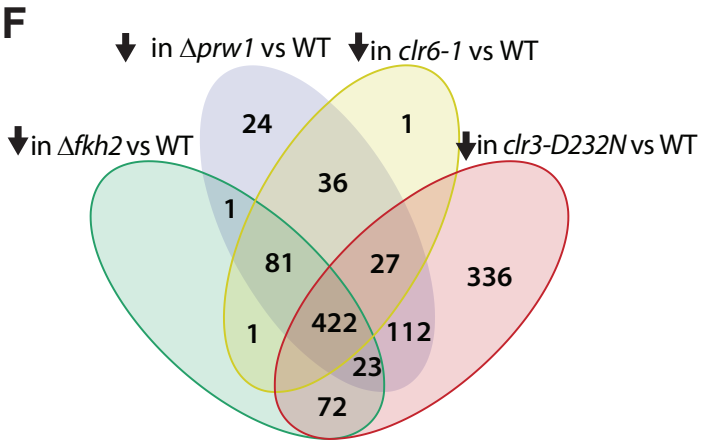

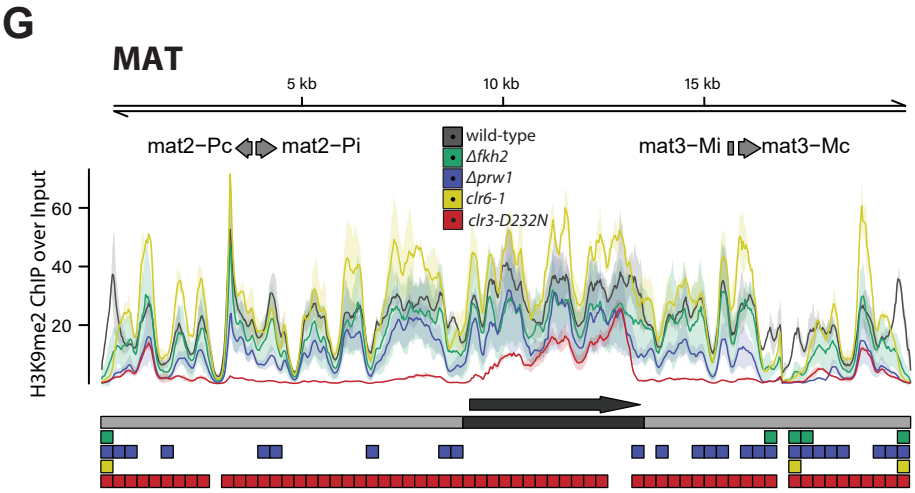

Figure 3 Supplement 2: Fkh2- containing Clr6 complexes contribute primarily to H3K9me2 spreading, while Clr3 is required for H3K9me2 accumulation at all heterochromatin regions except islands.

A.-D. Volcano plots were generated as in Figure 3. Dots are colored by their annotation to nucleation or spreading zones broken down by heterochromatin location (pericentromere, subtelomere, MAT) or presence within a previously identified euchromatin embedded H3K9me2 heterochromatin region.

E. The number of regions called as significant in each direction for each of the pairwise comparisons is tabulated per each category of genomic feature.

F. The overlap of regions identified as significantly reduced in H3K9me2 signal in each mutant vs WT is compared in a Venn Diagram.

G. Signal tracks for H3K9me2 ChIP-Seq in *MAT ⊿REIII* at the full mating_type_region contig from the Pombase reference genome, as in Figure 3E. Gene annotations for the mating type cassette genes are additionally included above the signal tracks. Note that most Clr6 subunits only show defects in spreading to the right of *cenH,* indicated with a dark grey arrow.

Figure 3 Supplement 3

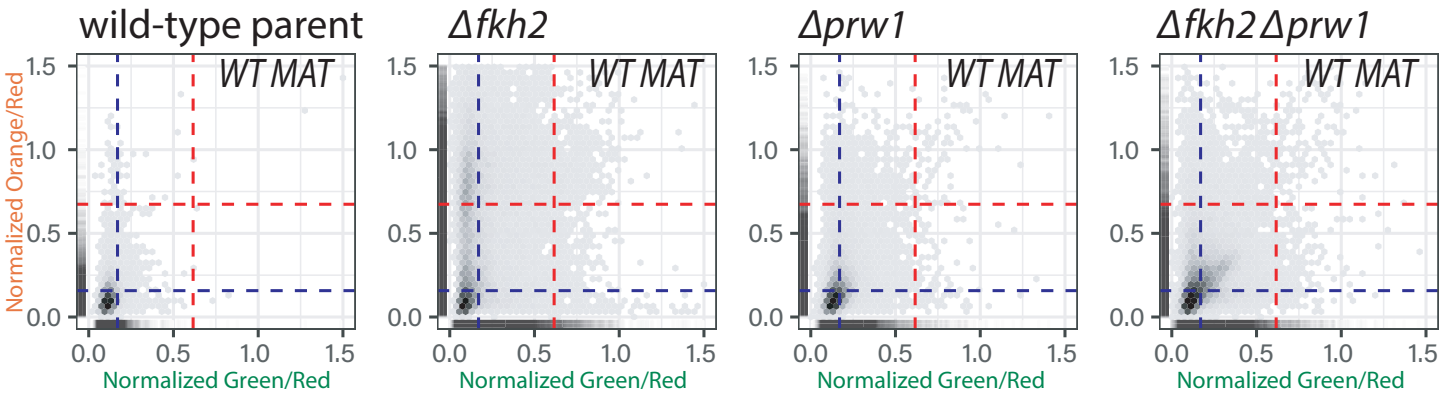

Figure 3 Supplement 3: Validation of *Δfkh2, Δprw1 and Δfkh2 Δprw1* double mutant spreading defects in *WT MAT.*

Δfkh2, Δprw1 and Δfkh2 Δprw1 mutants were re-created *de novo* in *WT MAT.* 2D density hexbin and rug plots of indicated backgrounds are shown.

Figure 3 Supplement 4

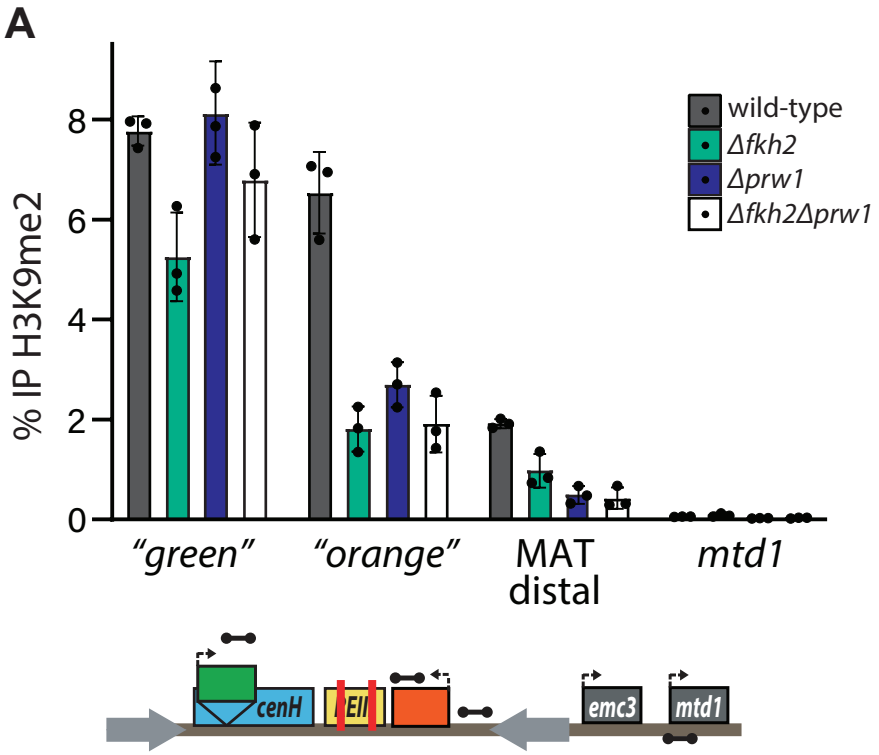

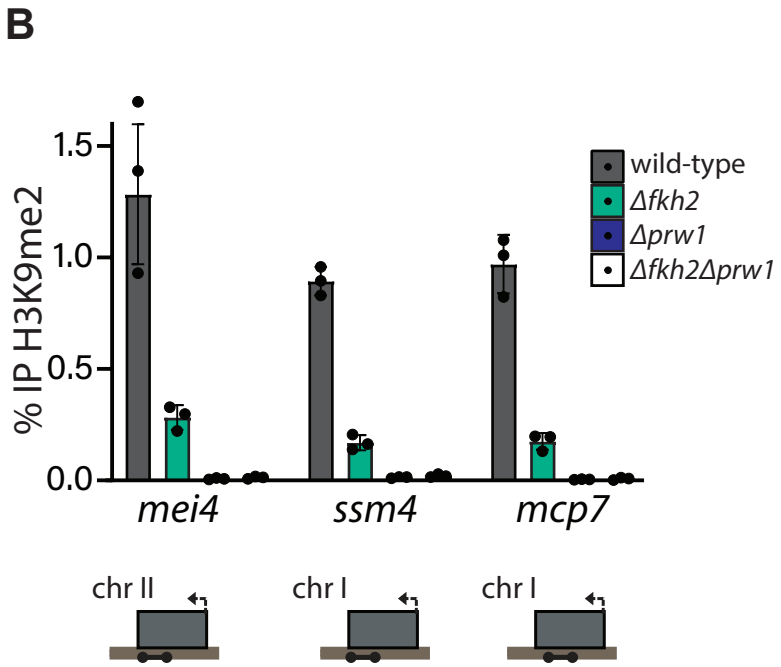

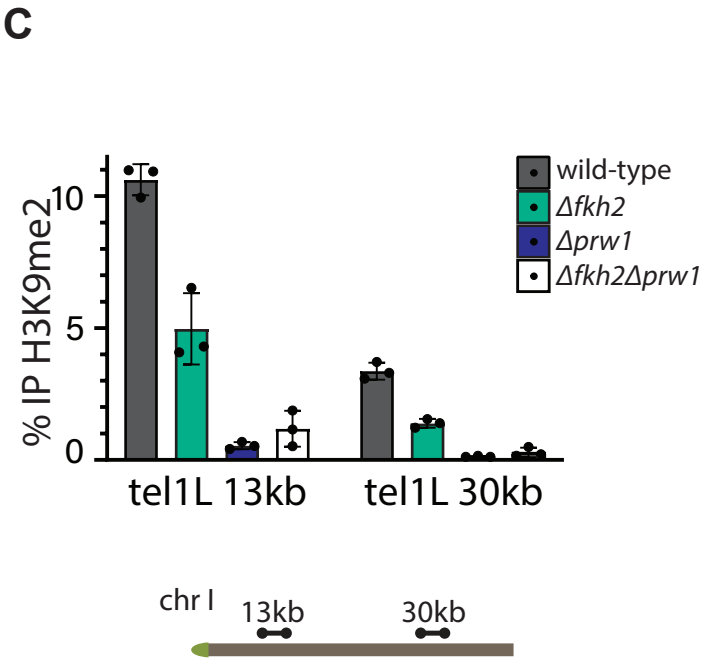

Figure 3 Supplement 4: Fkh2 and Prw1 act together in spreading H3K9me2.

A. H3K9me2 ChIP -qPCR at the MAT locus in wild-type *MAT ΔREIII, Δfkh2, Δprw1,* and the *Δfkh2Δprw1* double mutant.

B. As in A., at indicated heterochromatin islands.

C. As in A., at *tel IL.*

Error bars represent 1SD of 3 biological replicates.

Figure 4 Supplement 1

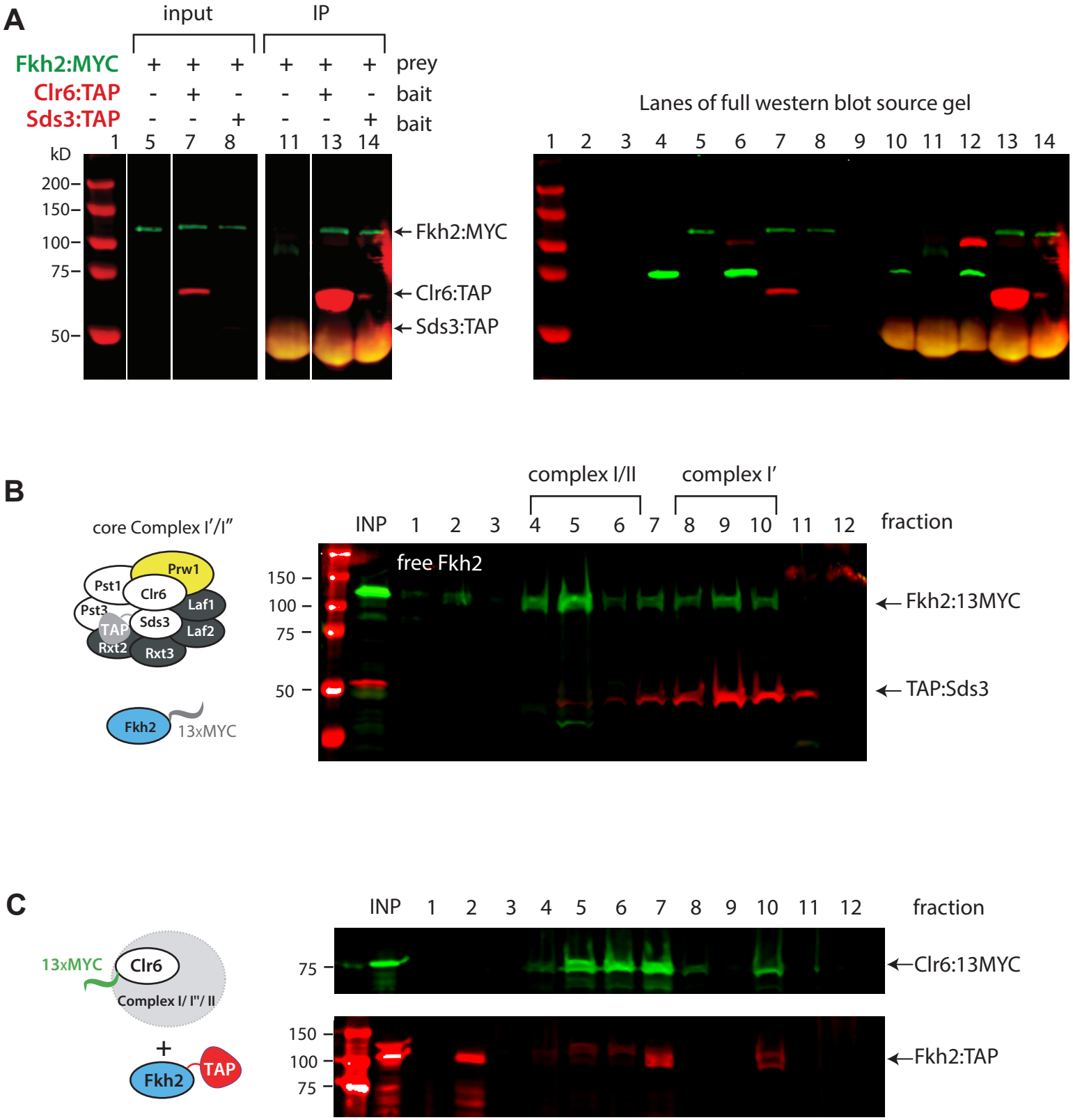

Figure 4 Supplement 1: Fkh2 is a constituent member of Clr6 complexes.

A. Co-Immunoprecipitation experiment with baits Clr6-TAP or Sds3-TAP and prey Fkh2-MYC. LEFT: Western blot against indicated proteins for the Co-IP experiment. RIGHT shows the entire western blot, including lanes unrelated to the co-IP experiment (2-4,5,10,12).

B. Sucrose density gradient for whole cell extracts of cells containing Sds3-TAP, a signature of complex I/I", and Fkh2:MYC. Gradient and Western as in Figure 4.

C. Single channel Western blots of Figure 4 A.

Figure 4 Supplement 2

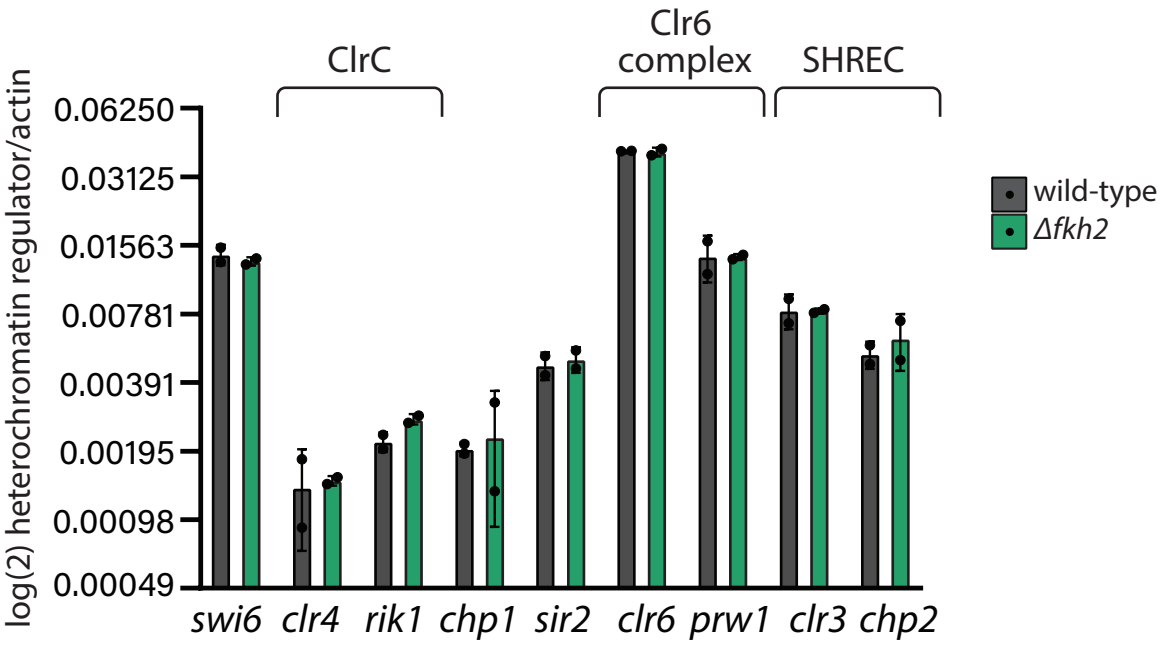

Figure 4 Supplement 2: Fkh2 does not affect transcription of core heterochromatin regulators.

RT-qPCR of indicated core heterochromatin regulators, including representatives of ClrC, Clr6, and SHREC in *MAT ΔREIII* wild-type or *Δfkh2* cells. Heterochromatin regulator transcripts are normalized to the *act1* transcript and shown on a log2 scale, given the wide distribution of transcript abundance between indicated regulators. Error bars indicate 1SD of 2 biological replicates.

Table 1: Nuclear function gene deletion library

	Systematic ID	Symbol	Description
1	SPAC1002.05c	jmj2	histone demethylase Jmj2
2	SPAC1006.03c	red1	RNA elimination defective protein Red1
3	SPAC1039.05c	klf1	transcription factor, zf-fungal binuclear cluster type Klf1
4	SPAC1071.02	mms19	CIA machinery protein Mms19
5	SPAC1071.06	arp9	SWI/SNF and RSC complex subunit Arp9
6	SPAC10F6.08c	nht1	Ino80 complex HMG box subunit Nht1
7	SPAC10F6.11c	atg17	autophagy associated protein kinase activator Atg17
8	SPAC1142.03c	swi2	Swi5 complex subunit Swi2
9	SPAC1142.08	fhl1	forkhead transcription factor Fhl1
10	SPAC11D3.07c	toe4	transcription factor, zf-fungal binuclear cluster type(predicted)
11	SPAC11D3.16c		Schizosaccharomyces specific protein
12	SPAC11E3.01c	swr1	SNF2 family ATP-dependent DNA helicase Swr1
13	SPAC11H11.01	sst6	ESCRT I complex subunit Vps23
14	SPAC11H11.05c	fta6	Mis6-Sim4 complex Fta6
15	SPAC12B10.10	nod1	medial cortical node Gef2-related protein protein Nod1
16	SPAC12G12.13c	cid14	TRAMP complex poly(A) polymerase subunit Cid14
17	SPAC139.03	toe2	transcription factor, zf-fungal binuclear cluster type (predicted)
18	SPAC139.06	hat1	histone acetyltransferase Hat1
19	SPAC1399.05c	toe1	transcription factor, zf-fungal binuclear cluster type
20	SPAC13A11.04c	ubp8	SAGA complex ubiquitin C-terminal hydrolase Ubp8
21	SPAC13D6.02c	byr3	translational activator, zf-CCHC type zinc finger protein (predicted)
22	SPAC13G6.01c	rad8	ubiquitin-protein ligase E3/ ATP-dependent DNA helicase Rad8
23	SPAC144.02	iec1	Ino80 complex subunit Iec1
24	SPAC144.05		DNA-dependent ATPase/ ubiquitin-protein ligase E3 (predicted)
25	SPAC144.06	apl5	AP-3 adaptor complex subunit Apl5 (predicted)
26	SPAC144.14	klp8	kinesin-like protein Klp8
27	SPAC14C4.06c	nab2	poly(A) binding protein Nab2 (predicted)
28	SPAC14C4.12c	laf1	Clr6 L associated factor 1 Laf1
29	SPAC14C4.13	rad17	RFC related checkpoint protein Rad17
30	SPAC1556.01c	rad50	DNA repair protein Rad50
31	SPAC15A10.11	ubr11	UBR ubiquitin-protein ligase E3 Ubr11
32	SPAC15A10.15	sgo2	inner centromere protein, shugoshin Sgo2
33	SPAC1610.01	saf5	splicing factor Saf5
34	SPAC1610.02c	mrpl1	mitochondrial ribosomal protein subunit L1 (predicted)
35	SPAC1687.05	pli1	SUMO E3 ligase Pli1
36	SPAC1687.09	irs4	autophagy/CVT pathway ENTH/VHS domain protein Irs4 (predicted)
37	SPAC16A10.03c		ubiquitin-protein ligase E3 involved in vesicle docking Pep5/Vps11-like (predicted)
38	SPAC16A10.07c	taz1	shelterin complex subunit Taz1
39	SPAC16C9.04c	mot2	CCR4-Not complex ubiquitin-protein ligase E3 subunit Mot2
40	SPAC16C9.05	cph1	Clr6 histone deacetylase associated PHD protein-1 Cph1
41	SPAC16E8.12c	png3	ING family homolog Png3 (predicted)
42	SPAC1751.01c	gti1	gluconate transmembrane transporter inducer Gti1
43	SPAC1782.05	ypa2	protein phosphatase type 2A regulator, PTPA family Ypa2
44	SPAC1782.08c	rex3	exonuclease Rex3 (predicted)
45	SPAC1782.09c	clp1	Cdc14-related protein phosphatase Clp1/Flp1
46	SPAC1783.05	hrp1	ATP-dependent DNA helicase Hrp1
47	SPAC17A2.12	rrp1	ATP-dependent DNA helicase/ ubiquitin-protein ligase E3 (predicted)
48	SPAC17G8.05	med20	mediator complex subunit Med20
49	SPAC17G8.07	yaf9	YEATS family histone acetyltransferase subunit Yaf9
50	SPAC17G8.09	shg1	Set1C complex subunit Shg1
51	SPAC17G8.10c	dma1	mitotic spindle checkpoint ubiquitin ligase Dma1
52	SPAC17G8.13c	mst2	histone acetyltransferase Mst2
53	SPAC17H9.10c	ddb1	Cul4-RING E3 adaptor Ddb1
54	SPAC17H9.19c	cdt2	WD repeat protein Cdt2
55	SPAC1805.14		Schizosaccharomyces specific protein
56	SPAC1805.15c	pub2	HECT-type ubiquitin-protein ligase E3 Pub2
57	SPAC1851.03	ckb1	CK2 family regulatory subunit Ckb1
58	SPAC18G6.02c	chp1	heterochromatin (HP1) family chromodomain protein Chp1
59	SPAC18G6.10	lem2	LEM domain nuclear inner membrane protein Heh1/Lem2
60	SPAC18G6.13		Schizosaccharomyces specific protein
61	SPAC1952.05	gcn5	SAGA complex histone acetyltransferase catalytic subunit Gcn5
62	SPAC19A8.10	rfp1	SUMO-targeted ubiquitin-protein ligase subunit Rfp1
63	SPAC19D5.06c	din1	RNA pyrophosphohydrolase Din1
64	SPAC19D5.11c	ctf8	Ctf18 RFC-like complex subunit Ctf8
65	SPAC19E9.02	fin1	serine/threonine protein kinase, NIMA related Fin1
66	SPAC19G12.13c	poz1	shelterin complex subunit Poz1
67	SPAC19G12.17	erh1	enhancer of rudimentary homolog Erh1
68	SPAC1B3.17	clr2	chromatin silencing protein Clr2
69	SPAC1D4.09c	rtf2	replication termination factor Rtf2
70	SPAC1D4.11c	lkh1	dual specificity protein kinase Lkh1
71	SPAC1F3.01	rrp6	exosome 3'-5' exoribonuclease subunit Rrp6
72	SPAC1F3.06c	spo15	mitotic and mieotic spindle pole body protein Spo15

73	SPAC1F7.01c	spt6	nucleosome remodeling protein Spt6
74	SPAC20G4.04c	hus1	checkpoint clamp complex protein Hus1
75	SPAC20G8.08c	fft1	SMARCAD1 family ATP-dependent DNA helicase Fft1 (predicted)
76	SPAC20H4.03c	tfs1	general transcription elongation factor TFIIS
77	SPAC20H4.10	ufd2	ubiquitin-protein ligase E4 Ufd2 (predicted)
78	SPAC21E11.03c	pcr1	transcription factor Pcr1
79	SPAC21E11.05c	cyp8	cyclophilin family peptidyl-prolyl cis-trans isomerase Cyp8
80	SPAC222.04c	ies6	Ino80 complex subunit Ies6
81	SPAC222.15	meu13	Tat binding protein 1(TBP-1)-interacting protein (TBPIP) homolog (predicted)
82	SPAC22A12.01c	pso2	DNA 5' exonuclease (predicted)
83	SPAC22E12.11c	set3	histone lysine methyltransferase Set3
84	SPAC22E12.19	snt1	Set3 complex subunit Snt1
85	SPAC22F3.02	atf31	transcription factor Atf31
86	SPAC22F3.09c	res2	MBF transcription factor complex subunit Res2
87	SPAC22F8.12c	shf1	small histone ubiquitination factor Shf1
88	SPAC22H12.02	tfg3	TFIID, TFIIF, Ino80, SWI/SNF, and NuA3 complex subunit Tfg3
89	SPAC23A1.07		ubiquitin-protein ligase E3 (predicted)
90	SPAC23C11.08	php3	CCAAT-binding factor complex subunit Php3
91	SPAC23C11.15	pst2	Clr6 histone deacetylase complex subunit Pst2
92	SPAC23C4.03	hrk1	haspin related kinase Hrk1
93	SPAC23D3.01	pdp3	PWWP domain protein, involved in chromatin remodeling (predicted)
94	SPAC23D3.09	arp42	SWI/SNF and RSC complex subunit Arp42
95	SPAC23E2.01	fep1	iron-sensing transcription factor Fep1
96	SPAC23E2.03c	ste7	arrestin family meiotic suppressor protein Ste7
97	SPAC23G3.04	ies4	Ino80 complex subunit Ies4
98	SPAC23G3.07c	snf30	SWI/SNF complex subunit Snf30
99	SPAC23G3.08c	ubp7	ubiquitin C-terminal hydrolase Ubp7
100	SPAC23G3.10c	ssr3	SWI/SNF and RSC complex subunit Ssr3
101	SPAC23H3.05c	swd1	Set1C complex subunit Swd1
102	SPAC23H4.12	alp13	MRG family Clr6 histone deacetylase complex subunit Alp13
103	SPAC24B11.10c	cfh1	SEL1/TPR repeat protein Cfh1 (predicted)
104	SPAC25A8.01c	fft3	SMARCAD1 family ATP-dependent DNA helicase Fft3
105	SPAC25H1.02	jmj1	histone demethylase Jmj1 (predicted)
106	SPAC26H5.03	pcf2	CAF assembly factor (CAF-1) complex subunit B, Pcf2
107	SPAC29A4.09		rRNA exonuclease Rrp17 (predicted)
108	SPAC29A4.18	prw1	Clr6 histone deacetylase complex subunit Prw1
109	SPAC29B12.02c	set2	histone lysine H3-K36 methyltransferase Set2
110	SPAC29B12.03	spd1	ribonucleotide reductase (RNR) inhibitor
111	SPAC29B12.06c	rcd1	CCR4-Not complex RNA-binding protein subunit Rcd1
112	SPAC29B12.08	clr5	Clr5 protein
113	SPAC2C4.07c	dis32	3'-5'-exoribonuclease activity Dis3L2
114	SPAC2F3.15	lsk1	P-TEFb-associated cyclin-dependent protein kinase Lsk1
115	SPAC2F3.16		ubiquitin-protein ligase E3, implicated in DNA repair (predicted)
116	SPAC2F7.07c	cph2	Clr6 histone deacetylase associated PHD protein Cph2
117	SPAC2F7.08c	snf5	SWI/SNF complex subunit Snf5
118	SPAC2G11.05c	rim20	BRO1 domain protein Rim20
119	SPAC2G11.10c	uba42	thiosulfate sulfurtransferase, URM1 activating enzyme E1-type Uba42 (predicted)
120	SPAC30D11.07	nth1	DNA endonuclease III
121	SPAC31A2.09c	apm4	AP-2 adaptor complex mu subunit Apm4 (predicted)
122	SPAC31A2.16	gef2	RhoGEF Gef2
123	SPAC31G5.09c	spk1	MAP kinase Spk1
124	SPAC31G5.19	abo1	ATPase with bromodomain protein
125	SPAC323.03c		Schizosaccharomyces specific protein
126	SPAC328.05	hrb1	RNA-binding protein involved in export of mRNAs Hrb1 (predicted)
127	SPAC32A11.03c	phx1	stationary phase-specific homeobox transcription factor Phx1
128	SPAC343.04c	gid7	GID complex subunit Gid7 (predicted)
129	SPAC343.11c	msc1	Swr1 complex subunit Msc1
130	SPAC343.18	rfp2	SUMO-targeted ubiquitin-protein ligase subunit Rfp2
131	SPAC3A11.05c	kms1	meiotic spindle pole body KASH domain protein Kms1
132	SPAC3C7.08c	elf1	AAA family ATPase Elf1
133	SPAC3F10.10c	map3	pheromone M-factor receptor Map3
134	SPAC3F10.12c		transcription factor (predicted)
135	SPAC3G6.01	hrp3	ATP-dependent DNA helicase Hrp3
136	SPAC3G6.06c	rad2	FEN-1 endonuclease Rad2
137	SPAC3G6.11	chl1	ATP-dependent DNA helicase Chl1 (predicted)
138	SPAC3G9.07c	hos2	histone deacetylase (class I) Hos2
139	SPAC3H1.11	hsr1	transcription factor Hsr1
140	SPAC3H1.12c	snt2	Lid2 complex PHD finger subunit Snt2
141	SPAC3H8.08c		transcription factor (predicted)
142	SPAC4A8.09c	cwf21	complexed with Cdc5 protein Cwf21
143	SPAC4F8.11	sea2	SEA complex WD repeat subunit Sea2 (predicted)
144	SPAC4G9.06c	chz1	histone H2A-H2B dimer chaperone Chz1 (predicted)
145	SPAC4H3.02c	swc3	Swr1 complex subunit Swc3
146	SPAC4H3.05	srs2	ATP-dependent DNA helicase, UvrD subfamily

147	SPAC56F8.16	esc1	transcription factor Esc1 (predicted)
148	SPAC57A10.09c	nhp6	High-mobility group non-histone chromatin protein (predicted)
149	SPAC5D6.02c	mug165	Clr6 histone deacetylase complex subunit Mug165
150	SPAC5D6.08c	mes1	meiotic APC inhibitor Mes1
151	SPAC630.14c	tup12	transcriptional corepressor Tup12
152	SPAC631.02	bdf2	BET family double bromodomain protein Bdf2
153	SPAC637.09	rex1	3'-5'- exoribonuclease Rex1 (predicted)
154	SPAC644.14c	rad51	RecA family recombinase Rad51/Rhp51
155	SPAC664.01c	swi6	heterochromatin (HP1) family chromodomain protein Swi6
156	SPAC664.02c	arp8	Ino80 complex actin-like protein Arp8
157	SPAC664.07c	rad9	checkpoint clamp complex protein Rad9
158	SPAC664.15	caf4	CCR4-Not complex subunit Caf4/Mdv1 (predicted)
159	SPAC688.06c	slx4	structure-specific endonuclease subunit Slx4
160	SPAC694.06c	mrc1	claspin, Mrc1
161	SPAC6B12.05c	ies2	Ino80 complex subunit Ies2
162	SPAC6B12.07c		ubiquitin-protein ligase E3 with SPX domain, human LORNRF1 ortholog (predicted)
163	SPAC6B12.14c		conserved fungal protein
164	SPAC6B12.16	meu26	DUF4451 family conserved fungal protein
165	SPAC6F12.09	rdp1	RNA-directed RNA polymerase Rdp1
166	SPAC6F6.09	eaf6	Mst2/NuA4 histone acetyltransferase complex subunit Eaf6
167	SPAC6G9.03c	mug183	histone H3.3 H4 heterotetramer chaperone Rtt106-like (predicted)
168	SPAC6G9.10c	sen1	ATP-dependent 5' to 3' DNA/RNA helicase Sen1
169	SPAC6G9.16c	xrc4	XRCC4 nonhomologous end joining factor Xrc4
170	SPAC7D4.04	atg11	autophagy associated protein Atg11
171	SPAC7D4.14c	iss10	NURS complex subunit Iss10
172	SPAC821.07c	moc3	transcription factor Moc3
173	SPAC823.03	ppk15	serine/threonine protein kinase Ppk15 (predicted)
174	SPAC824.04	swd22	mRNA cleavage and polyadenylation specificity factor complex, WD repeat protein Swd22
175	SPAC890.07c	rmt1	type I protein arginine N-methyltransferase Rmt1
176	SPAC8C9.14	prr1	transcription factor Prr1
177	SPAC8C9.17c	spc34	DASH complex subunit Spc34
178	SPAC8F11.03	msh3	MutS protein homolog 3
179	SPAC9E9.08	rad26	ATRIP, ATR checkpoint kinase regulatory subunit Rad26
180	SPAC9E9.10c	cbh1	CENP-B homolog Cbh1
181	SPAP14E8.02	tos4	chromatin binding FHA domain protein Tos4 (predicted)
182	SPAP27G11.15	slx1	structure-specific endonuclease catalytic subunit Slx1
183	SPAP32A8.03c	bop1	ubiquitin-protein ligase E3, human RNF126 ortholog (predicted)
184	SPAP8A3.02c	ofd2	histone H2A dioxygenase Ofd2
185	SPAPB1E7.02c	mcl1	DNA polymerase alpha accessory factor Mcl1
186	SPAPB24D3.01	toe3	transcription factor (predicted)
187	SPAPB2B4.03	cig2	G1/S-specific B-type cyclin Cig2
188	SPBC1105.04c	cbp1	CENP-B homolog
189	SPBC119.08	pmk1	MAP kinase Pmk1
190	SPBC119.14	rti1	Rad22 homolog Rti1
191	SPBC1198.11c	reb1	RNA polymerase I transcription termination factor/ RNA polymerase II transcription factor Reb1
192	SPBC11B10.05c	rsp1	random septum position protein, DNAJ domain protein Rsp1
193	SPBC11B10.08		WW domain containing conserved fungal protein
194	SPBC11B10.10c	pht1	histone H2A variant H2A.Z, Pht1
195	SPBC1347.07	rex2	RNA exonuclease (predicted)
196	SPBC13E7.08c	leo1	RNA polymerase II associated Paf1 complex subunit Leo1
197	SPBC13G1.08c	ash2	Ash2-trithorax family protein
198	SPBC146.06c	fan1	DNA repair protein Fan1
199	SPBC14C8.17c	spt8	SAGA complex subunit Spt8
200	SPBC14F5.07	doa10	ER ubiquitin-protein ligase E3 Doa10 (predicted)
201	SPBC15C4.01c	oca3	TPR repeat protein Oca3/ ER membrane protein complex Ecm2 (predicted)
202	SPBC15C4.06c		ubiquitin-protein ligase E3 Meu34, human RNF13 family homolog, unknown biological role (predicted)
203	SPBC15D4.03	slm9	histone H3.3 H4 chaperone, hira family Slm9
204	SPBC1604.09c	rex4	exoribonuclease Rex4 (predicted)
205	SPBC1604.16c		RNA-binding protein, G-patch type, human GPANK1 ortholog
206	SPBC1685.08	cti6	histone deacetylase complex ubiquitin-like protein ligase subunit Cti6
207	SPBC16A3.07c	nrm1	MBF complex corepressor Nrm1
208	SPBC16A3.19	eaf7	histone acetyltransferase complex subunit Eaf7
209	SPBC16D10.07c	sir2	Sirtuin family histone deacetylase Sir2
210	SPBC16E9.11c	pub3	HECT-type ubiquitin-protein ligase E3 Pub3 (predicted)
211	SPBC16E9.12c	pab2	poly(A) binding protein Pab2
212	SPBC16G5.03	mrz1	ubiquitin-protein ligase E3/SUMO transferase, Topors, possibly associated with DNA damage (predicted)
213	SPBC16G5.15c	fkh2	forkhead transcription factor Fkh2
214	SPBC16G5.17		transcription factor, zf-fungal binuclear cluster type (predicted)
215	SPBC1703.04	mlh1	MutL family protein Mlh1 (predicted)
216	SPBC1703.14c	top1	DNA topoisomerase I
217	SPBC1709.11c	png2	ING family histone acetyltransferase complex PHD-type zinc finger subunit Png2
218	SPBC1711.14	rec15	meiotic recombination protein Rec15
219	SPBC1718.02	hop1	linear element associated protein Hop1
220	SPBC1734.06	rhp18	Rad18 homolog ubiquitin protein ligase E3, Rhp18

221	SPBC1734.15	rsc4	RSC complex subunit Rsc4
222	SPBC1773.16c		transcription factor, zf-fungal binuclear cluster type(predicted)
223	SPBC1778.10c	ppk21	serine/threonine protein kinase Ppk21 (predicted)
224	SPBC17D11.04c	nto1	histone acetyltransferase complex PHD finger subunit Nto1 (predicted)
225	SPBC17G9.05	rct1	cyclophilin family peptidyl-prolyl cis-trans isomerase, RRM-containing Rct1
226	SPBC18H10.06c	swd2	Set1C complex subunit Swd2.1
227	SPBC18H10.15	cdk11	serine/threonine protein kinase Cdk11
228	SPBC19C7.02	ubr1	N-end-recognizing protein, UBR ubiquitin-protein ligase E3 Ubr1
229	SPBC1A4.03c	top2	DNA topoisomerase II
230	SPBC1D7.03	clg1	cyclin-like protein involved in autophagy Clg1 (predicted)
231	SPBC1D7.04	mlo3	RNA binding protein Mlo3
232	SPBC20F10.05	nrl1	RNAi-mediated silencing protein, human NRDE2 ortholog Nrl1
233	SPBC20F10.10	psl1	cyclin pho85 family Psl1 (predicted)
234	SPBC215.03c	csn1	COP9/signalosome complex subunit Csn1
235	SPBC215.06c		nucleolar RNA-binding protein, human LYAR homolog, implicated in transcriptional regulation
236	SPBC215.07c	pdp2	PWWP domain protein Pdp2 (predicted)
237	SPBC216.05	rad3	ATR checkpoint kinase Rad3
238	SPBC216.06c	swi1	replication fork protection complex subunit Swi1
239	SPBC21B10.13c	yox1	MBF complex corepressor Yox1
240	SPBC21C3.02c	dep1	Sds3-like family protein Dep1
241	SPBC21C3.20c	git1	C2 domain protein Git1
242	SPBC21D10.09c	rkr1	RQC complex ubiquitin-protein ligase E3 Rkr1 (predicted)
243	SPBC21D10.10	bdc1	bromodomain protein Bdc1
244	SPBC23E6.02	rrp2	ATP-dependent DNA helicase/ ubiquitin-protein ligase E3 (predicted)
245	SPBC23E6.09	ssn6	transcriptional corepressor Ssn6
246	SPBC23G7.13c		plasma membrane urea transmembrane transporter (predicted)
247	SPBC24C6.05	sec28	coatomer epsilon subunit (predicted)
248	SPBC25B2.08		Schizosaccharomyces pombe specific protein
249	SPBC26H8.09c	snf59	SWI/SNF complex subunit Snf59
250	SPBC28E12.02		RNA-binding protein
251	SPBC28F2.07	sfr1	Swi five-dependent recombination mediator Sfr1
252	SPBC28F2.10c	ngg1	SAGA complex subunit Ngg1/Ada3
253	SPBC29A10.03c	pcf1	CAF assembly factor (CAF-1) complex large subunit Pcf1
254	SPBC29A10.05	exo1	exonuclease I Exo1
255	SPBC29A10.14	rec8	meiotic cohesin complex subunit Rec8
256	SPBC29A3.03c	gid2	GID complex ubiquitin-protein ligase E3 subunit Gid2/Rmd5 (predicted)
257	SPBC29A3.05	vps71	Swr1 complex subunit Vps71
258	SPBC29A3.13	pdp1	PWWP domain protein Pdp1
259	SPBC29B5.01	atf1	transcription factor, Atf-CREB family Atf1
260	SPBC2A9.04c	san1	sir antagonist, ubiquitin-protein ligase E3
261	SPBC2D10.11c	nap2	histone H2A-H2B chaperone Nap2
262	SPBC2D10.17	clr1	SHREC complex intermodule linker subunit Clr1
263	SPBC2F12.09c	atf21	transcription factor, Atf-CREB family Atf21
264	SPBC2F12.12c	cay1	cactin, spliceosome complex subunit
265	SPBC2G2.06c	apl1	AP-2 adaptor complex beta subunit Apl1 (predicted)
266	SPBC2G2.14	csi1	mitotic centromere-SPB clustering protein Csi1
267	SPBC2G5.02c	ckb2	CK2 family regulatory subunit Ckb2 (predicted)
268	SPBC30B4.04c	sol1	SWI/SNF complex subunit Sol1
269	SPBC30D10.10c	tor1	serine/threonine protein kinase Tor1
270	SPBC31F10.07	lsb5	actin cortical patch component Lsb5 (predicted)
271	SPBC31F10.10c	mub1	Armadillo-type fold protein, zf-MYND type zinc finger protein, Mub1-Rad6-Ubr2 ubiquitin ligase complex Mub1 (predicted)
272	SPBC31F10.13c	hip1	histone H3.3 H4 chaperone, hira family Hip1
273	SPBC31F10.14c	hip3	HIRA interacting protein Hip3
274	SPBC32F12.07c		membrane associated ubiquitin-protein ligase E3, MARCH family (predicted)
275	SPBC32H8.06	mug93	TPR repeat protein, meiotically spliced
276	SPBC337.03	rhn1	RNA polymerase II transcription termination factor homolog
277	SPBC342.05	crb2	DNA repair protein Rad9 homolog Crb2
278	SPBC342.06c	rtt109	RTT109 family histone lysine acetyltransferase
279	SPBC354.03	swd3	WD repeat protein Swd3
280	SPBC354.05c	sre2	membrane-tethered transcription factor Sre2
281	SPBC365.10	arp5	Ino80 complex actin-like protein Arp5
282	SPBC36B7.05c	pib1	endosomal and vacuolar ubiquitin-protein ligase E3/phosphatidylinositol(3)-phosphate binding protein Pib1
283	SPBC36B7.08c	ccp1	histone chaperone, CENP-A nucleosome disassembly Ccp1
284	SPBC3B8.02	php5	CCAAT-binding factor complex subunit Php5
285	SPBC3D6.04c	mad1	mitotic spindle checkpoint protein Mad1
286	SPBC3D6.09	dpb4	DNA polymerase epsilon subunit Dpb4
287	SPBC3H7.13	far10	SIP/FAR complex FHA domain subunit Far10/Csc1
288	SPBC4.05	mlo2	ubiquitin protein ligase E3 component human N-recognin 7 homolog Mlo2
289	SPBC428.06c	rxt2	histone deacetylase complex subunit Rxt2
290	SPBC428.08c	clr4	histone lysine H3 methyltransferase Clr4
291	SPBC4B4.03	rsc1	RSC complex subunit Rsc1
292	SPBC4C3.12	1-Sep	forkhead transcription factor Sep1
293	SPBC530.08		membrane-tethered transcription factor (predicted)
294	SPBC530.14c	dsk1	SR protein-specific kinase Dsk1

295	SPBC543.07	pek1	MAP kinase kinase Pek1
296	SPBC56F2.03	arp10	dynactin complex actin-like protein Arp10 (predicted)
297	SPBC56F2.05c		transcription factor (predicted)
298	SPBC582.04c	dsh1	RNAi protein, Dsh1
299	SPBC582.06c	mcp6	horsetail movement protein Hrs1/Mcp6
300	SPBC609.05	pob3	histone H2A-H2B chaperone, FACT complex subunit Pob3
301	SPBC651.11c	apm3	AP-3 adaptor complex subunit Apm3 (predicted)
302	SPBC660.06		WW domain containing conserved fungal protein
303	SPBC660.14	mik1	mitotic inhibitor kinase Mik1
304	SPBC6B1.04	mde4	microtubule-site clamp monopolin complex subunit Mde4
305	SPBC6B1.06c	ubp14	Lys48-specific deubiquitinase Ubp14
306	SPBC725.02	mpr1	histidine-containing response regulator phosphotransferase Mpr1
307	SPBC725.11c	php2	CCAAT-binding factor complex subunit Php2
308	SPBC776.02c	dis2	serine/threonine protein phosphatase PP1, Dis2
309	SPBC776.16	mis20	centromere protein Mis20/Eic2
310	SPBC800.03	clr3	histone deacetylase (class II) Clr3
311	SPBC83.03c	tas3	RITS complex subunit 3
312	SPBC902.02c	ctf18	Ctf18 RFC-like complex subunit Ctf18
313	SPBC902.04	rmn1	RNA-binding protein
314	SPBC902.06	mto2	gamma tubulin complex linker Mto2
315	SPBP16F5.03c	tra1	SAGA complex phosphatidylinositol pseudokinase Tra1
316	SPBP22H7.05c	abo2	ATPase with bromodomain protein (predicted)
317	SPBP23A10.05	ssr4	SWI/SNF and RSC complex subunit Ssr4
318	SPBP35G2.08c	air1	TRAMP complex zinc knuckle subunit Air1
319	SPBP35G2.10	mit1	SHREC complex ATP-dependent DNA helicase subunit Mit1
320	SPBP35G2.13c	swc2	Swr1 complex subunit Swc2
321	SPBP8B7.07c	set6	histone lysine methyltransferase Set6 (predicted)
322	SPBP8B7.23	rnf10	ubiquitin-protein ligase E3 (predicted)
323	SPBP8B7.28c	stc1	CLRC ubiquitin ligase complex linker protein, LIM-like Stc1
324	SPCC1020.12c	xap5	xap-5-like protein
325	SPCC11E10.08	rik1	CLRC ubiquitin ligase complex WD repeat protein Rik1
326	SPCC1223.13	cbf12	CBF1/Su(H)/LAG-1 family transcription factor Cbf12
327	SPCC1235.05c	fft2	SMARCAD1 family ATP-dependent DNA helicase Fft2 (predicted)
328	SPCC1235.09	hif2	Set3 complex subunit Hif2
329	SPCC1235.12c	mug146	Schizosaccharomyces specific protein Mug46
330	SPCC1259.04	iec3	Ino80 complex subunit Iec3
331	SPCC1259.07	rxt3	transcriptional regulatory protein Rxt3
332	SPCC126.02c	pku70	Ku domain protein Pku70
333	SPCC126.04c	sgf73	SAGA complex deubiquitinating submodule subunit Sgf73
334	SPCC126.07c	asr1	ubiquitin-protein ligase E3 Asr1 (predicted)
335	SPCC126.11c		RNA-binding protein, rrm type
336	SPCC126.13c	sap18	splicing factor Sap18 (predicted)
337	SPCC132.02	hst2	Sirtuin family histone deacetylase Hst2
338	SPCC1393.02c	spt2	non-specific DNA binding protein Spt2 (predicted)
339	SPCC1393.05	ers1	RNA-silencing factor Ers1
340	SPCC1442.13c	sqs2	R3H and G-patch domain protein Sqs2
341	SPCC1450.02	bdf1	Swr1 complex bromodomain subunit Bdf1
342	SPCC1450.03	utp502	ribonucleoprotein (RNP) complex Utp502 (predicted)
343	SPCC1494.03	arz1	human RAP1 GTPase-GDP dissociation stimulator ortholog, Zfs1 target number 1
344	SPCC162.11c	urk1	uridine kinase/uracil phosphoribosyltransferase (predicted)
345	SPCC1620.14c	snf22	ATP-dependent DNA helicase Snf22
346	SPCC1682.13	laf2	Clr6 associated factor 2, Laf2
347	SPCC16C4.11	pef1	Pho85/PhoA-like cyclin-dependent kinase Pef1
348	SPCC1739.03	hrr1	Helicase Required for RNAi-mediated heterochromatin assembly Hrr1
349	SPCC1739.05	set5	histone lysine methyltransferase Set5 (predicted)
350	SPCC1739.07	cti1	exosome C1D family subunit Cti1
351	SPCC1739.12	ppe1	serine/threonine protein phosphatase Ppe1
352	SPCC1753.03c	rec7	meiotic recombination protein Rec7
353	SPCC1840.04	pca1	metacaspase Pca1
354	SPCC188.07	ccq1	shelterin complex HEAT repeat subunit Ccq1
355	SPCC188.13c	dcr1	dicer
356	SPCC18B5.03	wee1	M phase inhibitor protein kinase Wee1
357	SPCC18B5.07c	nup61	nucleoporin Nup61
358	SPCC24B10.07	gad8	AGC family protein kinase Gad8
359	SPCC24B10.08c	ada2	SAGA complex subunit Ada2
360	SPCC24B10.14c	xlf1	XRCC4-like nonhomologous end joining factor, Cernunnon Xlf1/Nej1
361	SPCC24B10.19c	nts1	Clr6 histone deacetylase complex subunit Nts1
362	SPCC297.03	ssp1	Ca2+/calmodulin-dependent (CaMMK)-like protein kinase Ssp1
363	SPCC297.04c	set7	histone lysine H3-K37 methyltransferase Set7
364	SPCC2H8.05c	dbl1	double strand break localizing Dbl1
365	SPCC306.04c	set1	histone lysine H3-K4 methyltransferase Set1
366	SPCC31H12.08c	ccr4	CCR4-Not complex 3'-5'-exoribonuclease subunit Ccr4
367	SPCC330.01c	rhp16	Rad16 homolog ATP-dependent DNA helicase/ ubiquitin protein ligase E3 Rhp16
368	SPCC330.02	rhp7	Rad7 homolog Rhp7

369	SPCC338.16	pof3	F-box protein Pof3
370	SPCC364.02c	bis1	splicing factor Bis1
371	SPCC364.06	nap1	histone H2A-H2B chaperone Nap1
372	SPCC417.07c	mto1	gamma tubulin complex linker Mto1
373	SPCC417.09c		transcription factor (predicted)
374	SPCC4B3.12	set9	histone lysine H4-K20 methyltransferase Set9
375	SPCC4G3.15c	not2	CCR4-Not complex NOT box subunit Not2
376	SPCC4G3.19	alp16	gamma tubulin complex subunit Alp16
377	SPCC548.05c	dbl5	ubiquitin-protein ligase E3 Dbl5
378	SPCC550.12	arp6	actin-like protein Arp6
379	SPCC550.15c	rei1	ribosome biogenesis protein Rei1 (predicted)
380	SPCC553.04	cyp9	WD repeat containing cyclophilin family peptidyl-prolyl cis-trans isomerase Cyp9 (predicted)
381	SPCC576.13	swc5	Swr1 complex subunit Swc5
382	SPCC594.05c	spf1	Set1C ubiquitin-protein ligase E3 subunit Spf1
383	SPCC61.02	spt3	SAGA complex subunit Spt3
384	SPCC613.12c	raf1	CLRC ubiquitin ligase complex WD repeat subunit Raf1/Dos1
385	SPCC622.15c		Schizosaccharomyces specific protein
386	SPCC622.16c	epe1	Jmjc domain chromatin associated protein Epe1
387	SPCC622.19	jmj4	peptidyl-lysine 3-dioxygenase activity jmj4 (predicted)
388	SPCC645.13	bye1	transcription elongation regulator Bye1 (predicted)
389	SPCC663.11	saf1	splicing associated factor Saf1
390	SPCC663.12	cid12	poly(A) polymerase Cid12
391	SPCC736.08	cbf11	CBF1/Su(H)/LAG-1 family transcription factor Cbf11
392	SPCC736.11	ago1	argonaute
393	SPCC757.09c	rnc1	KH domain RNA-binding protein Rnc1
394	SPCC895.06	elp2	elongator complex WD repeat protein Elp2 (predicted)
395	SPCC895.07	alp14	TOG/XMAP215 microtubule plus end tracking polymerase Alp14
396	SPCC970.07c	raf2	CLRC ubiquitin ligase complex subunit Raf2

Table 2: Strain table

Strain	Genotype
PAS075	Locus2*::ade6p::3xE2C:hygMX* at Locus2 (between SPBC1711.11 and SPBC1711.12)
PM003	Wild-type strain: h(+); ura4-D18; leu1-32; ade6-M216; his7-366
PM006	972 h- wild-type
PAS193	Δ*K*::*ade6p:*mKO2; *ade6p:*SF-GFP between *REIII* and mat3M; *ade6p*:3xE2C*: hygMX* at Locus2; *clr4::kanMX,* h(-)
PAS216	*cenH*::*ade6p:*SF-GFP(Kint2); *mat3m(Eco*RV):: *ade6p:*mKO2; *ade6p:*3xE2C: *hygMX* at Locus2; *clr4::kanMX,* h90
PAS217	*cenH*: *ade6p:*SF-GFP (Kint2); *mat3m(Eco*RV):: *ade6p:*mKO2; *ade6p:*3xE2C: *hygMX* at Locus2, h90
PAS231	*ura4::natMX:dh:ade6p:*SF-GFP, *ade6p:*mKO2 3 kb, *leu1*::*ade6p:*3xE2C: *hygMX*
PAS331	*cenH*:: *ade6p:*SF-GFP (Kint2); *mat3m(Eco*RV):: *ade6p:*mKO2; *ade6p:*3xE2C:*hygMX* at Locus2; Δ*REIII*::REIII(Δs1, Δs2) in *clr4::kanMX,* h90
PAS332	*cenH*:: *ade6p:*SF-GFP (Kint2); *mat3m(Eco*RV):: *ade6p:*mKO2; *ade6p:*3xE2C:*hygMX* at Locus2; Δ*REIII*::REIII(Δs1, Δs2), h90
PAS353	*ura4::natMX:dh:ade6p:*SF-GFP, *ade6p:*mKO2 3 kb, *leu1*::*ade6p:*3xE2C: *hygMX; gcn5::kanMX*
PAS482	Δ*K*::*ade6p:*mKO2; *ade6p:* SF-GFP between *REIII* and mat3M; *ade6p:*3xE2C*: hygMX* at Locus2, h(-); 'OFF' allele
PAS795	*cenH*: *ade6p:*SF-GFP (Kint2); *mat3m(Eco*RV):: *ade6p:*mKO2; *ade6p:*3xE2C: *hygMX* at Locus2; *fkh2::natMX*
PAS796	*cenH*: *ade6p:*SF-GFP (Kint2); *mat3m(Eco*RV):: *ade6p:*mKO2; *ade6p:*3xE2C: *hygMX* at Locus2; *prw1::kanMX*
PAS797	*cenH*: *ade6p:*SF-GFP (Kint2); *mat3m(Eco*RV):: *ade6p:*mKO2; *ade6p:*3xE2C: *hygMX* at Locus2; *png3::kanMX*
PAS798	*cenH*:: *ade6p:*SF-GFP (Kint2); *mat3m(Eco*RV):: *ade6p:*mKO2; *ade6p:*3xE2C:*hygMX* at Locus2; Δ*REIII*::REIII(Δs1, Δs2); *fkh2::natMX*
PAS799	*cenH*:: *ade6p:*SF-GFP (Kint2); *mat3m(Eco*RV):: *ade6p:*mKO2; *ade6p:*3xE2C:*hygMX* at Locus2; Δ*REIII*::REIII(Δs1, Δs2); *prw1::kanMX*
PAS800	*cenH*:: *ade6p:*SF-GFP (Kint2); *mat3m(Eco*RV):: *ade6p:*mKO2; *ade6p:*3xE2C:*hygMX* at Locus2; Δ*REIII*::REIII(Δs1, Δs2); *png3::kanMX*
PAS803	Δ*K*::*ade6p:*mKO2; *ade6p:* SF-GFP between *REIII* and mat3M; *ade6p:*3xE2C*: hygMX* at Locus2; 'OFF' allele; *fkh2::natMX*
PAS808	*cenH*: *ade6p:*SF-GFP (Kint2); *mat3m(Eco*RV):: *ade6p:*mKO2; *ade6p:*3xE2C: *hygMX* at Locus2; *fkh2::natMX; prw1::kanMX* by cross
PAS809	*cenH*: *ade6p:*SF-GFP (Kint2); *mat3m(Eco*RV):: *ade6p:*mKO2; *ade6p:*3xE2C: *hygMX* at Locus2; *fkh2::natMX; prw1::kanMX* by sequential knockout
PAS810	*cenH*:: *ade6p:*SF-GFP (Kint2); *mat3m(Eco*RV):: *ade6p:*mKO2; *ade6p:*3xE2C:*hygMX* at Locus2; Δ*REIII*::REIII(Δs1, Δs2); *fkh2::natMX; prw1::kanMX* by cross
PAS811	*cenH*:: *ade6p:*SF-GFP (Kint2); *mat3m(Eco*RV):: *ade6p:*mKO2; *ade6p:*3xE2C:*hygMX* at Locus2; Δ*REIII*::REIII(Δs1, Δs2); *fkh2::natMX; prw1::kanMX* by sequential knockout
PAS813	*cenH*:: *ade6p:*SF-GFP (Kint2); *mat3m(Eco*RV):: *ade6p:*mKO2; *ade6p:*3xE2C:*hygMX* at Locus2; Δ*REIII*::REIII(Δs1, Δs2); *apm3::natMX*
PAS816	apl5:SF-GFP:*hygMX*; Swi6:E2C:*kanMX*
PAS817	apm3:SF-GFP:*hygMX;* Swi6:E2C:*kanMX*
PAS833	fkh2::Fkh2:13XMYC Zilio et al.
PAS836	clr6::Clr6:13XMYC:*hygMX;* fkh2::Fkh2:TAP:*kanMX* Zilio et al.

PAS838	fkh2::Fkh2:13XMYC:*hygMX;* sds3::Sds3:TAP:*kanMX* Zilio et al.
PAS839	*cenH*:: *ade6p:*SF-GFP (Kint2); *mat3m(Eco*RV):: *ade6p:*mKO2; *ade6p:*3xE2C:*hygMX* at Locus2; Δ*REIII*::REIII(Δs1, Δs2); *clr6-1,* h90
PAS841	*cenH*:: *ade6p:*SF-GFP (Kint2); *mat3m(Eco*RV):: *ade6p:*mKO2; *ade6p:*3xE2C:*hygMX* at Locus2; Δ*REIII*::REIII(Δs1, Δs2), fkh2::Fkh2:13XMYC:*hygMX*, h90
PAS842	*cenH*:: *ade6p:*SF-GFP (Kint2); *mat3m(Eco*RV):: *ade6p:*mKO2; *ade6p:*3xE2C:*hygMX* at Locus2; Δ*REIII*::REIII(Δs1, Δs2); *clr3-D232N:natMX,* h90
PAS850	*cenH*:: *ade6p:*SF-GFP (Kint2); *mat3m(Eco*RV):: *ade6p:*mKO2; *ade6p:*3xE2C:*hygMX* at Locus2; Δ*REIII*::REIII(Δs1, Δs2), fkh2::Fkh2:13XMYC:*hygMX*; *prw1::kanMX,* h90
PAS867	*cenH*:: *ade6p:*SF-GFP (Kint2); *mat3m(Eco*RV):: *ade6p:*mKO2; *ade6p:*3xE2C:*kanMX* at Locus2; Δ*REIII*::REIII(Δs1, Δs2), clr6::Clr6:13XMYC:*hygMX,* h90
PAS868	*cenH*:: *ade6p:*SF-GFP (Kint2); *mat3m(Eco*RV):: *ade6p:*mKO2; *ade6p:*3xE2C:*kanMX* at Locus2; Δ*REIII*::REIII(Δs1, Δs2), clr6::Clr6:13XMYC:*hygMX; fkh2::natMX,* h90
PAS869	*cenH*:: *ade6p:*SF-GFP (Kint2); *mat3m(Eco*RV):: *ade6p:*mKO2; *ade6p:*3xE2C:*kanMX* at Locus2; Δ*REIII*::REIII(Δs1, Δs2), *apl5::kanMX; apm3::natMX,* h90
PAS870	*cenH*:: *ade6p:*SF-GFP (Kint2); *mat3m(Eco*RV):: *ade6p:*mKO2; *ade6p:*3xE2C:*kanMX* at Locus2; Δ*REIII*::REIII(Δs1, Δs2), *apl5::kanMX,* h90
PAS889	*cenH*:: *ade6p:*SF-GFP (Kint2); *mat3m(Eco*RV):: *ade6p:*mKO2; *ade6p:*3xE2C:*kanMX* at Locus2; *saf5::kanMX,* h90
PAS890	*cenH*:: *ade6p:*SF-GFP (Kint2); *mat3m(Eco*RV):: *ade6p:*mKO2; *ade6p:*3xE2C:*kanMX* at Locus2; *eaf6::kanMX,* h90
PAS891	*cenH*:: *ade6p:*SF-GFP (Kint2); *mat3m(Eco*RV):: *ade6p:*mKO2; *ade6p:*3xE2C:*kanMX* at Locus2; *pht1::kanMX,* h90
PAS892	*cenH*:: *ade6p:*SF-GFP (Kint2); *mat3m(Eco*RV):: *ade6p:*mKO2; *ade6p:*3xE2C:*kanMX* at Locus2; *hip1::kanMX,* h90
PAS893	*cenH*:: *ade6p:*SF-GFP (Kint2); *mat3m(Eco*RV):: *ade6p:*mKO2; *ade6p:*3xE2C:*kanMX* at Locus2; *gad8::kanMX,* h90
PAS894	Δ*K*::*ade6p:*mKO2; *ade6p:* SF-GFP between *REIII* and mat3M; *ade6p:*3xE2C*: hygMX* at Locus2, h(-); *pht1::kanMX,* h90
PAS895	Δ*K*::*ade6p:*mKO2; *ade6p:* SF-GFP between *REIII* and mat3M; *ade6p:*3xE2C*: hygMX* at Locus2, h(-); *hip1::kanMX,* h90
PAS896	Δ*K*::*ade6p:*mKO2; *ade6p:* SF-GFP between *REIII* and mat3M; *ade6p:*3xE2C*: hygMX* at Locus2, h(-); *gad8::kanMX,* h90
PAS897	Δ*K*::*ade6p:*mKO2; *ade6p:* SF-GFP between *REIII* and mat3M; *ade6p:*3xE2C*: hygMX* at Locus2, h(-); *hip1::kanMX,* h90
PAS898	Δ*K*::*ade6p:*mKO2; *ade6p:* SF-GFP between *REIII* and mat3M; *ade6p:*3xE2C*: hygMX* at Locus2, h(-); *gad8::kanMX,* h90
PAS899	*ura4::natMX:dh:ade6p:*SF-GFP, *ade6p:*mKO2 3 kb, *leu1*::*ade6p:*3xE2C: *hygMX; saf5::kanMX*
PAS900	*ura4::natMX:dh:ade6p:*SF-GFP, *ade6p:*mKO2 3 kb, *leu1*::*ade6p:*3xE2C: *hygMX; eaf6::kanMX*
PAS901	*ura4::natMX:dh:ade6p:*SF-GFP, *ade6p:*mKO2 3 kb, *leu1*::*ade6p:*3xE2C: *hygMX; pht1::kanMX*
PAS902	*ura4::natMX:dh:ade6p:*SF-GFP, *ade6p:*mKO2 3 kb, *leu1*::*ade6p:*3xE2C: *hygMX; hip1::kanMX*
PAS903	*ura4::natMX:dh:ade6p:*SF-GFP, *ade6p:*mKO2 3 kb, *leu1*::*ade6p:*3xE2C: *hygMX; gad8::kanMX*
PAS904	*cenH*:: *ade6p:*SF-GFP (Kint2); *mat3m(Eco*RV):: *ade6p:*mKO2; *ade6p:*3xE2C:*kanMX* at Locus2; Δ*REIII*::REIII(Δs1, Δs2); *saf5::kanMX,* h90

PAS905	*cenH*:: *ade6p:*SF-GFP (Kint2); *mat3m(Eco*RV):: *ade6p:*mKO2; *ade6p:*3xE2C:*kanMX* at Locus2; Δ*REIII*::REIII(Δs1, Δs2); *eaf6::kanMX,* h90
PAS906	*cenH*:: *ade6p:*SF-GFP (Kint2); *mat3m(Eco*RV):: *ade6p:*mKO2; *ade6p:*3xE2C:*kanMX* at Locus2; Δ*REIII*::REIII(Δs1, Δs2); *pht1::kanMX,* h90
PAS907	*cenH*:: *ade6p:*SF-GFP (Kint2); *mat3m(Eco*RV):: *ade6p:*mKO2; *ade6p:*3xE2C:*kanMX* at Locus2; Δ*REIII*::REIII(Δs1, Δs2); *hip1::kanMX,* h90
PAS908	*cenH*:: *ade6p:*SF-GFP (Kint2); *mat3m(Eco*RV):: *ade6p:*mKO2; *ade6p:*3xE2C:*kanMX* at Locus2; Δ*REIII*::REIII(Δs1, Δs2); *gad8::kanMX,* h90

Table 3: Primers used for ChIP qPCR and RT qPCR

oligo	target	sequence
OAS 0367	orange F	AATTTTCCTGCTGATGGTCCT
OAS 0368	orange R	TGATCACCAGGCATTTCAAG
OAS 0846	green F	CTGCTGATAAGCAAAAGAACG
OAS 0847	green R	CCATATGATCACGCTTTTCG
OAS 1044	dg F	CCATCACCACTTTCATCTCC
OAS 1045	df R	CAGGATACCTAGACGCACAA
OAS 1362	dh F	TTTAAAGCTTCACTACCATCGAAA
OAS 1363	dh R	TGCCAACAGTTTTTCCAACTT
OAS 1569	MAT distal F	TTTGTTTGGCCGATAGTCTG
OAS 1570	MAT distal R	GTTATGTTGGCAAAACGATTGCT
OAS 1601	mtd1 F	CCTGCCAGCAAGGAGAGGTT
OAS 1602	mtd1 R	TGGTACTTACTGCAGCTATGGTTAGG
OAS 1822	mei4 F	CCCCCTCTTCCCCCTTCTAA
OAS 1823	mei4 R	AAAGGCTAGACTCATGGGCATC
OAS 2087	mcp7 F	GGAAGCTGCCAATTTGTGGA
OAS 2088	mcp7 R	TTGCAGATCGTCCAAATCCTC
OAS 2091	ssm4 F	CAATTCCAAGCCCATTGACC
OAS 2092	ssm4 R	TGAAAACTGGGTCGCTCGAT
OAS 2097	SB_TEL1L_3 F	TAATGAGTTGCCCCGGGTAT
OAS 2098	SB_TEL1L_3 R	CCGAATGGCAAGATGGTAAT
OAS 2099	SB_TEL1L_7 F	CACAGACGTCTCCTGGTGTC
OAS 2100	SB_TEL1L_7 R	TGCAGAGTTTGCGGTACTTG
	swi6	GGTCGTCGGACAATGAAGTT
	swi6	TCCACCTTTTCTCGCCATAC
	clr4	TTCAAAGAAGCTGGGGAAGA
	clr4	CGTTACTTCGGGTCCTTCAA
	rik1	CGGTAGACACAGCGACTTCA
	rik1	TAATCCTGGAGGGCGATATG
	clr6	ATTTCTGCTGGCGGTTCAAT
	clr6	TCTACACCGTCTCCGTGGTG
	prw1	AGTGCGAAGCTTATGCCACA
	prw1	TAGCGTCTTGCGATCCAGAA
	clr3	AGACGCGTCCTTCGTGTTTT
	clr3	CGAGCACAAAACGCACTTTC
	chp2	AAGAAGATTGTGCGGGCTGT
	chp2	GCTGCATTCCTGCTTCTCCT
	sir2	GGGGCAGGCATAAGTACAAG
	sir2	ATTCGTCTCCGGCAAAAGAT
	chp1	AAATGGGCTGGCTATGATTG
	chp1	TTGCGCTTTTGTCTTTGTTG